

## **Supplementary Material**

# **A Benchmark Dataset and Evaluation for Non-Lambertian and Uncalibrated Photometric Stereo**

Boxin Shi   Zhipeng Mo   Zhe Wu   Dinglong Duan   Sai-Kit Yeung   Ping Tan

### **Contents**

Part I – Additional figures to the main paper .....	pages 2 – 8
Part II – Complete results for normal estimation .....	pages 9 – 28
Part III – Complete results for regional error analysis .....	pages 29 – 46

## Part I Footnote 1: Coordinate system and notations in Section 2.1

---

We use a camera centered coordinate system with viewing direction  $\mathbf{v} = [0,0,1]^T$ .

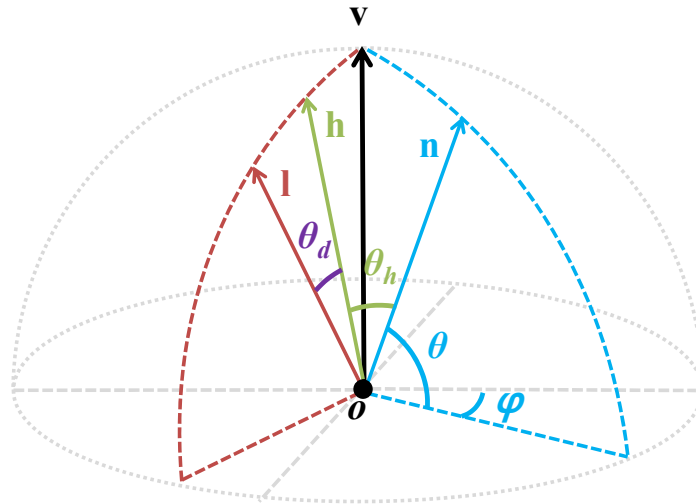
$\mathbf{n}$ : surface normal

$\mathbf{l}$ : lighting direction

$\mathbf{h}$ : half vector (the bisector of  $\mathbf{l}$  and  $\mathbf{v}$ )

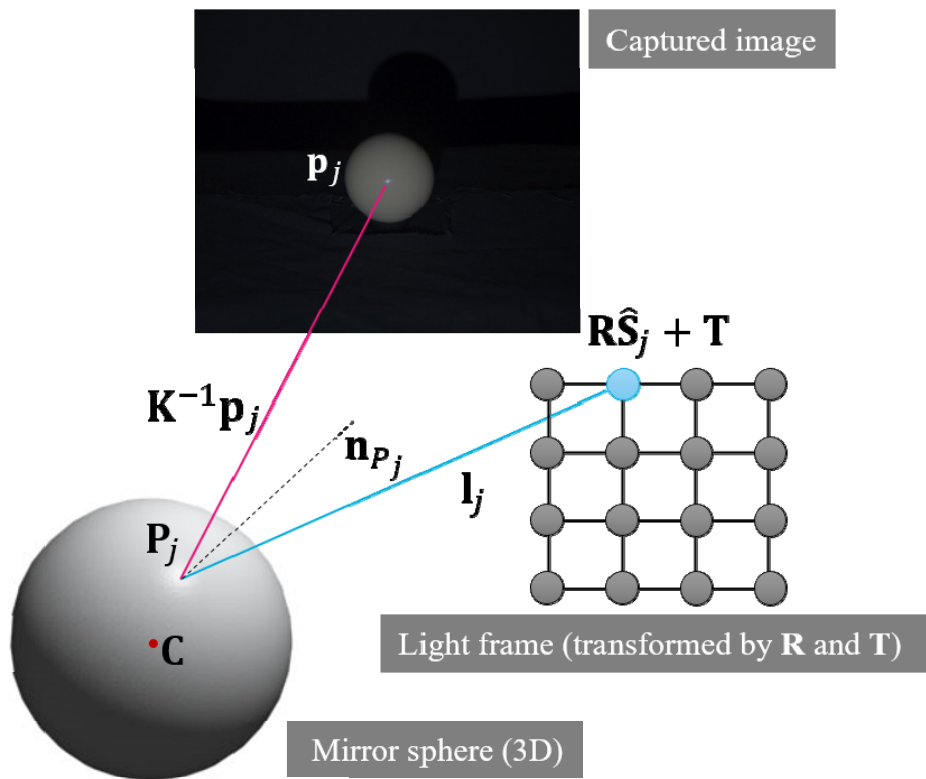
$\theta_h$ : the angle between  $\mathbf{n}$  and  $\mathbf{h}$

$\theta_d$ : the angle between  $\mathbf{h}$  and  $\mathbf{l}$  (or  $\mathbf{v}$ )



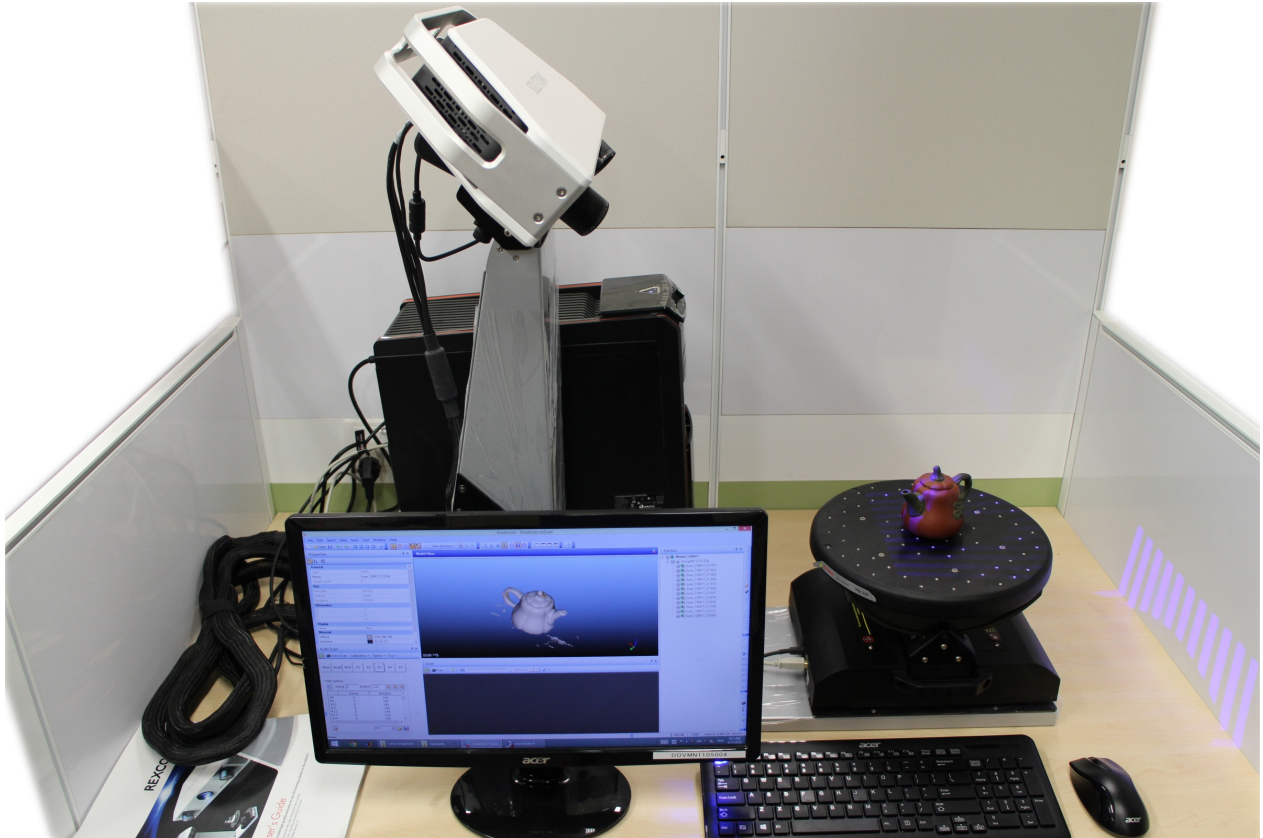
## Part I Footnote 7: Coordinate system and notations in Section 3.2

Our light frame contains 96 LED bulbs on a rectangular grid (here for simplicity, we only draw a  $4 \times 4$  grid). We use the algorithm introduced in Section 3.2 to simultaneously calibrate the 3D positions of all LEDs.

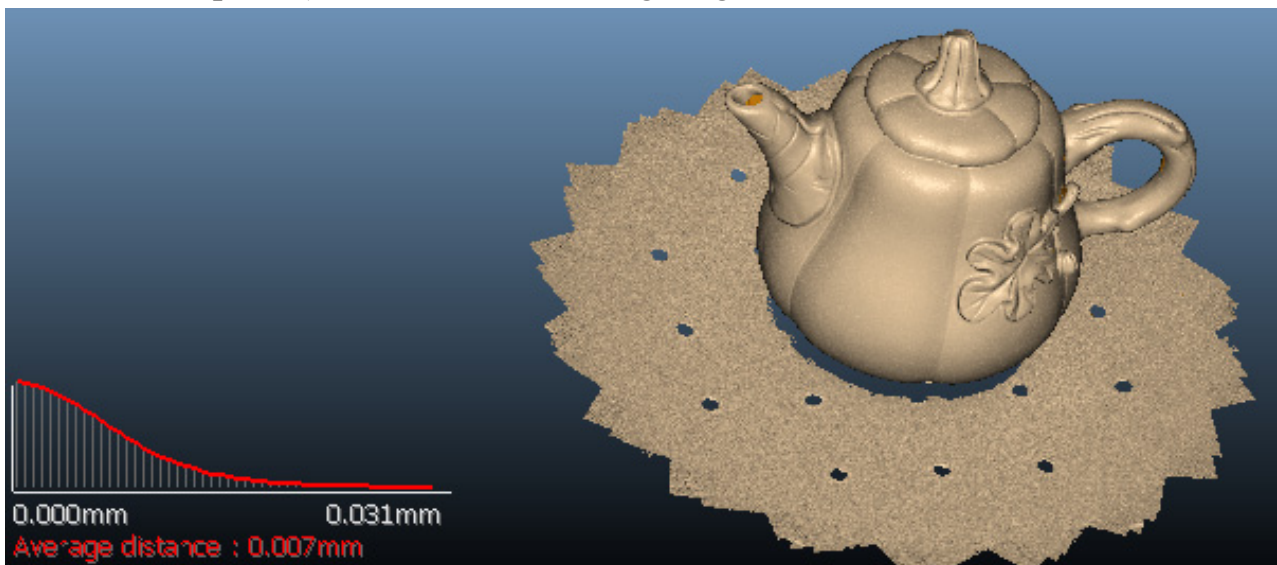


## Part I Footnote 8: Scanning setup in Section 3.3

We use the Rexcan CS scanner synchronized with the TA-300 turn table (such a combination is denoted as Rexcan CS+) to scan our objects.

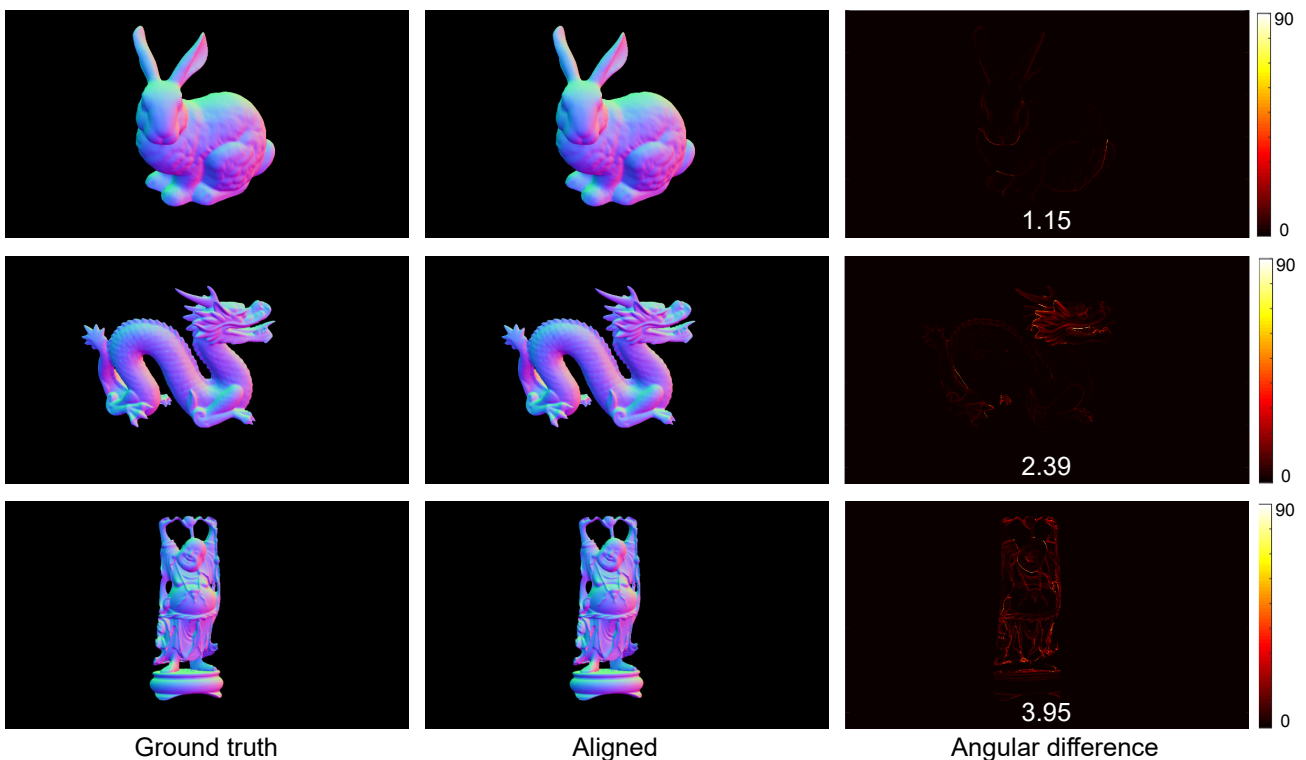


An example output from the scanner (after automatically merging all scans from different viewpoints) shows a small average registration error.



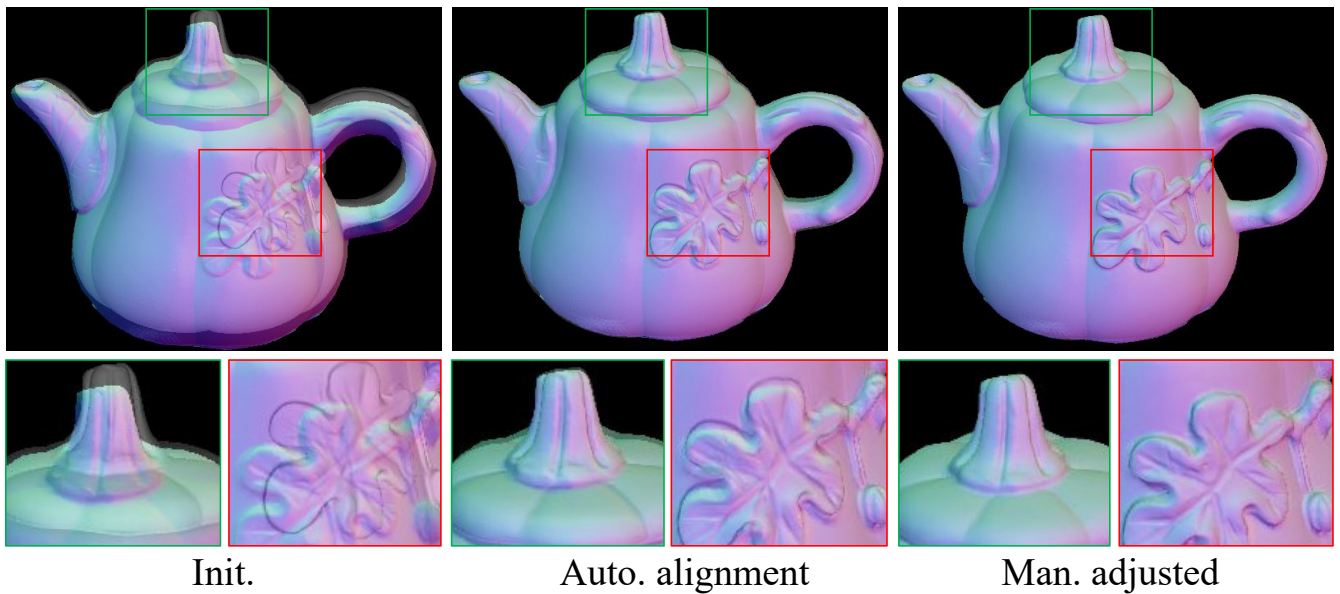
## Part I Footnote 10: Synthetic evaluation in Section 3.4

We use three 3D models, in particular the well-known BUNNY, DRAGON, and HAPPY BUDDHA from the Stanford 3D Scanning Repository, to perform synthetic experiments that quantitatively analyze the shape-to-image registration error introduced in Section 3.4. We first scale, translate, and rotate these 3D shapes to different poses and render their normal maps with three different intrinsic camera settings as ground truth. We then perform the shape-to-image alignment using the proposed procedure (a toolbox with step-by-step instruction is provided on our website). Finally, we calculate the per-pixel angular difference of the true and aligned normal maps. The results are summarized in the figure below. The error distribution (with mean values indicated using white fonts on the different maps) tells that 1) the registration error depends on the geometric complexity of the surface, for smooth surface like the BUNNY, we can obtain an average accuracy of  $1.15^\circ$ , but for highly complicated surface like the HAPPY BUDDHA the accuracy drops to  $3.95^\circ$  and 2) the high registration errors are mainly concentrated along the edges. The ‘DiLiGenT’ dataset includes both smooth and complicated shapes, so ideally the registration errors should be similar to the cases evaluated here. However, the real data contain much noise from the camera (calibration error, lens distortion, *etc.*) which is not included in the rendering pipeline, so the registration error here can only be seen as a lower bound reference.

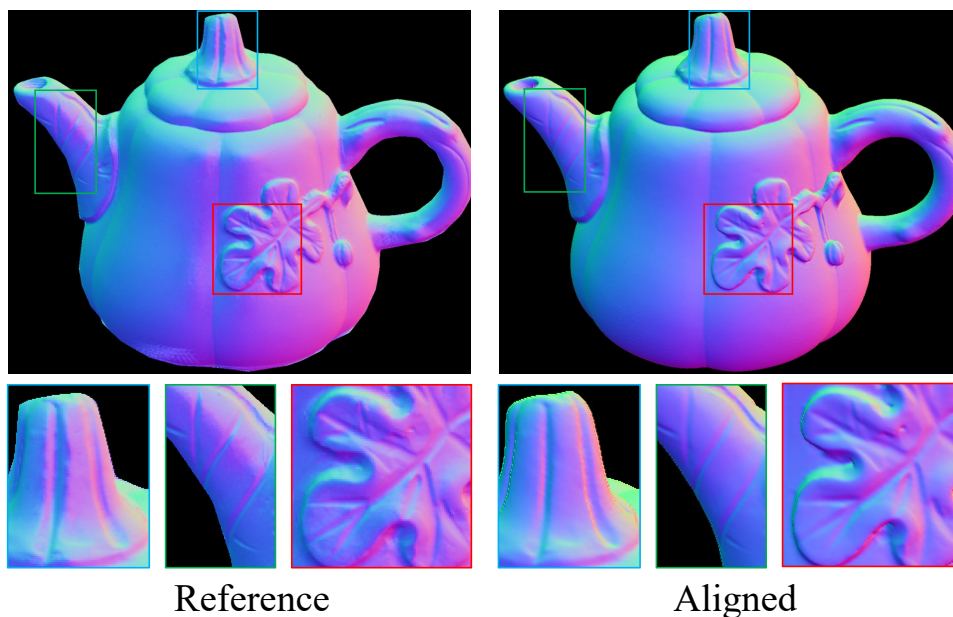


## Part I Footnote 11: Manual alignment result in Section 3.4

Real data contains noise from camera calibration, lens distortion, and other unexpected sources, we find for objects with large depth variation (in particular POT1, POT2, and BUDDHA), the automatic alignment results are obviously sub-optimal (middle figure below) even if we tried our best to provide good initialization. Therefore, we have to manually adjust the 3D shape by carefully rotating and translating it in minimum steps allowed by Meshlab based on the automatic alignment result. Upon finishing a single step of manual operation, we compare the normal map rendered from the aligned shape and the reference normal map by closely checking every small feature on both normal maps, until all parts are aligned with subpixel precision (right figure below).



A close-up check of the reference (from photometric stereo) and aligned (from the scanned shape) normal maps shows the high consistency between the two.



## Part I Footnote 12: Results using main and test datasets in Section 4

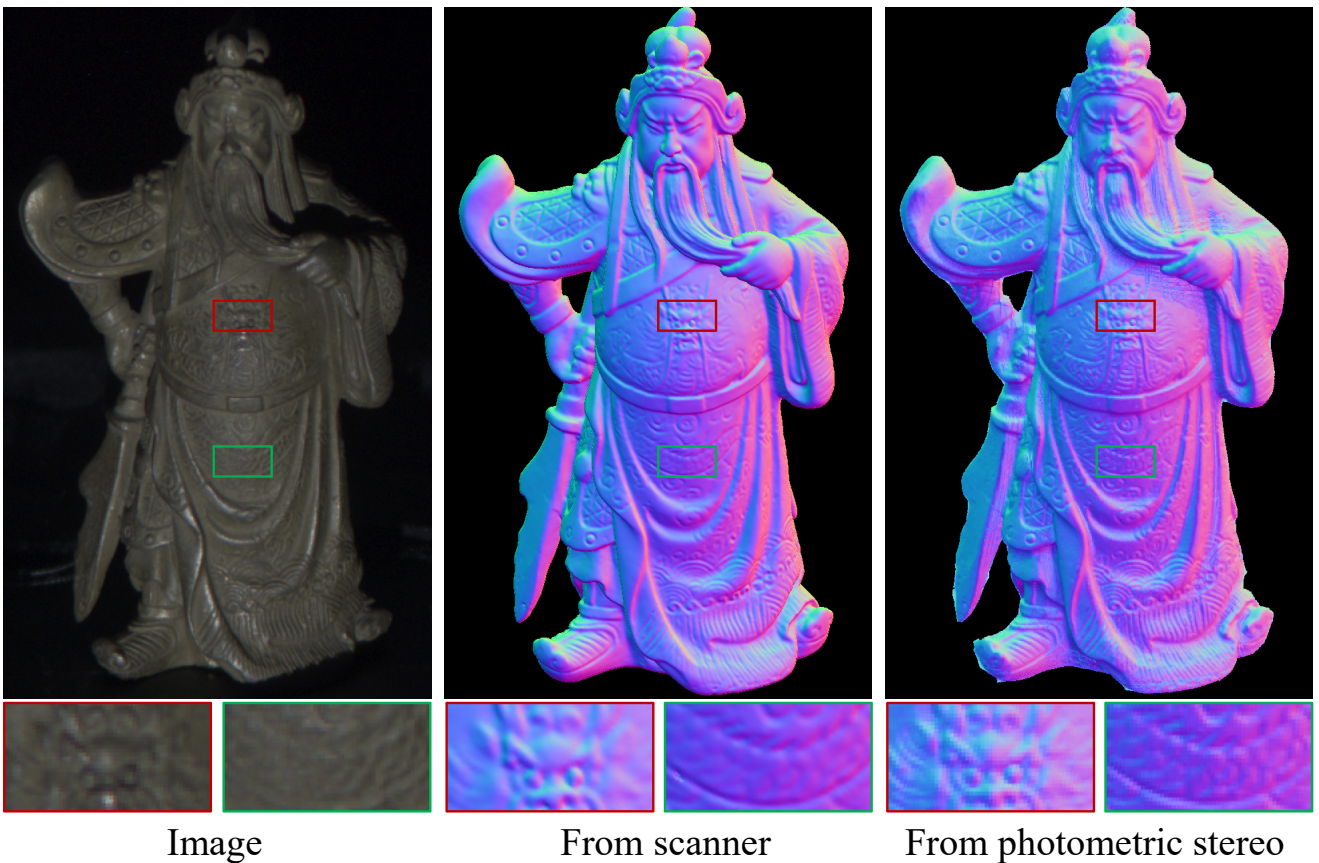
We show the summary of evaluation results using the main and test datasets in the table below. The numbers are mean angular errors (degree) for all pixels.

		BALL	CAT	POT1	BEAR	POT2	BUDDHA	GOBLET	READING	COW	HARVEST	
Main dataset	Non-Lambertian	BASELINE	4.10	8.41	8.89	8.39	14.65	14.92	18.50	19.80	25.60	30.62
		WG10	2.06	6.73	7.18	6.50	13.12	10.91	15.70	15.39	25.89	30.01
		IW14	2.54	7.21	7.74	7.32	14.09	11.11	16.25	16.17	25.70	29.26
		GC10	3.21	8.22	8.53	6.62	7.90	14.85	14.22	19.07	9.55	27.84
		AZ08	2.71	6.53	7.23	5.96	11.03	12.54	13.93	14.17	21.48	30.50
		HM10	3.55	8.40	10.85	11.48	16.37	13.05	14.89	16.82	14.95	21.79
		ST12	13.58	12.34	10.37	19.44	9.84	18.37	17.80	17.17	7.62	19.30
		ST14	1.74	6.12	6.51	6.12	8.78	10.60	10.09	13.63	13.93	25.44
		IA14	3.34	6.74	6.64	7.11	8.77	10.47	9.71	14.19	13.05	25.95
	Uncalibrated	AM07	7.27	31.45	18.37	16.81	49.16	32.81	46.54	53.65	54.72	61.70
		SM10	8.90	19.84	16.68	11.98	50.68	15.54	48.79	26.93	22.73	73.86
		PF14	4.77	9.54	9.51	9.07	15.90	14.92	29.93	24.18	19.53	29.21
		WT13	4.39	36.55	9.39	6.42	14.52	13.19	20.57	58.96	19.75	55.51
		Opt. A	3.37	7.50	8.06	8.13	12.80	13.64	15.12	18.94	16.72	27.14
		Opt. G	4.72	8.27	8.49	8.32	14.24	14.29	17.30	20.36	17.98	28.05
		LM13	22.43	25.01	32.82	15.44	20.57	25.76	29.16	48.16	22.53	34.45
Test dataset	Non-Lambertian	BASELINE	N.A.	8.43	10.44	9.36	17.06	15.15	15.86	21.41	21.97	27.62
		WG10	N.A.	7.15	6.77	6.26	14.14	11.36	12.81	15.96	20.64	26.27
		IW14	N.A.	7.54	7.44	6.81	14.95	11.77	13.44	18.05	22.17	26.46
		GC10	N.A.	7.12	10.50	8.60	9.53	16.28	24.13	19.99	10.97	30.32
		AZ08	N.A.	6.13	8.60	6.60	12.85	13.01	14.78	14.57	19.27	26.72
		HM10	N.A.	7.36	11.23	8.43	16.27	13.03	14.71	16.36	15.70	22.11
		ST12	N.A.	11.43	11.84	14.81	10.32	18.65	20.21	18.35	8.07	26.46
		ST14	N.A.	5.61	6.33	5.12	8.83	11.00	10.54	13.27	11.18	24.82
		IA14	N.A.	6.43	6.64	6.09	8.94	10.92	10.33	14.16	10.82	25.43
	Uncalibrated	AM07	N.A.	30.95	21.86	17.09	50.48	45.17	46.30	55.29	49.18	59.26
		SM10	N.A.	12.65	20.18	12.87	25.84	28.54	59.04	22.81	23.41	83.42
		PF14	N.A.	8.78	10.45	10.65	17.35	15.55	31.27	28.61	19.59	35.44
		WT13	N.A.	35.72	11.89	7.99	13.11	12.70	30.12	99.82	23.27	34.61
		Opt. A	N.A.	6.72	9.51	8.96	14.16	13.65	14.84	20.66	16.33	25.09
		Opt. G	N.A.	7.43	9.85	9.40	15.62	14.13	17.92	22.04	19.17	29.32
		LM13	N.A.	15.34	26.27	20.26	24.02	26.19	26.70	49.89	22.96	45.84

The evaluation results generally show similar trends in both the main and test datasets, *e.g.*, the best-performing method for each object is mostly the same on both datasets. However, distinctive features can also be observed, *e.g.*, for BEAR the top method becomes ST14 in the test dataset instead of AZ08 in the main dataset. The diversity becomes more obvious for objects with more complex non-Lambertian reflectance, since their irradiance values change more drastically when captured from another viewpoint albeit the same lighting condition, *e.g.*, for CAT most methods show difference smaller than one degree between the two datasets while for HARVEST the largest difference is  $7.16^\circ$  (ST12). Such distinctiveness plus the hidden ‘ground truth’ make the test dataset suitable for the purpose of evaluating newly propose method.

## Part I Footnote 19: Limitation of current dataset in Section 5

We have tried to include surfaces with more delicate structures, but the scanned geometry looks more blurred than photometric stereo results as shown in the figure below. Such a scanned shape cannot be used to evaluate photometric stereo. We believe for tiny objects or highly detailed geometry photometric cues have to be integrated with scanned shapes to obtain the more accurate 3D shapes. Though we have tried our best in achieving shape-to-image alignment, our ‘ground truth’ normal is still not the real ground truth of surface normal measurements.



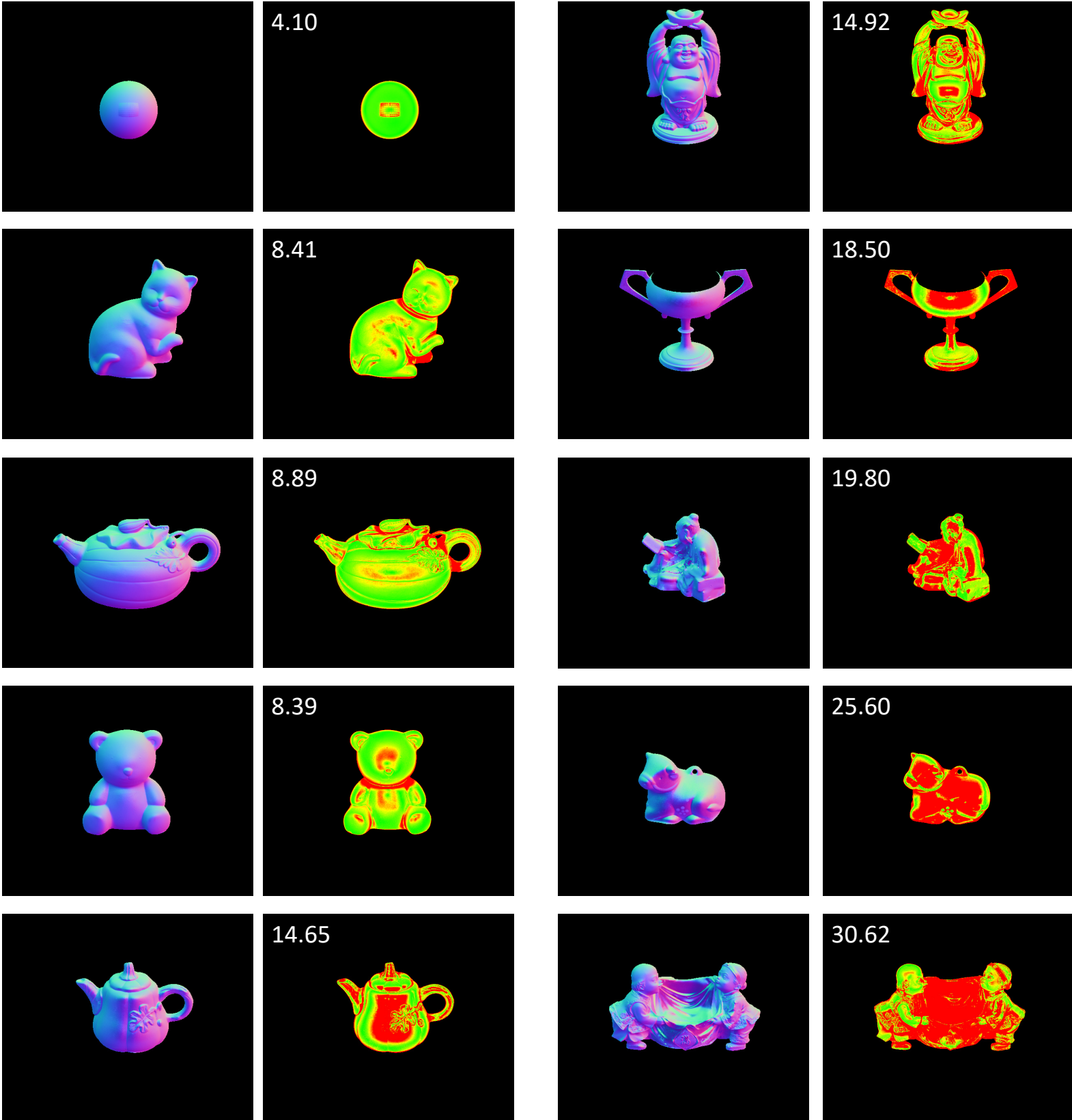
# Part II Footnote 13: Results for all objects and methods in Figure 2

R. J. Woodham. Photometric method for determining surface orientation from multiple images. Optical Engineering 19(1):139-144, 1980

## BASELINE

0

20



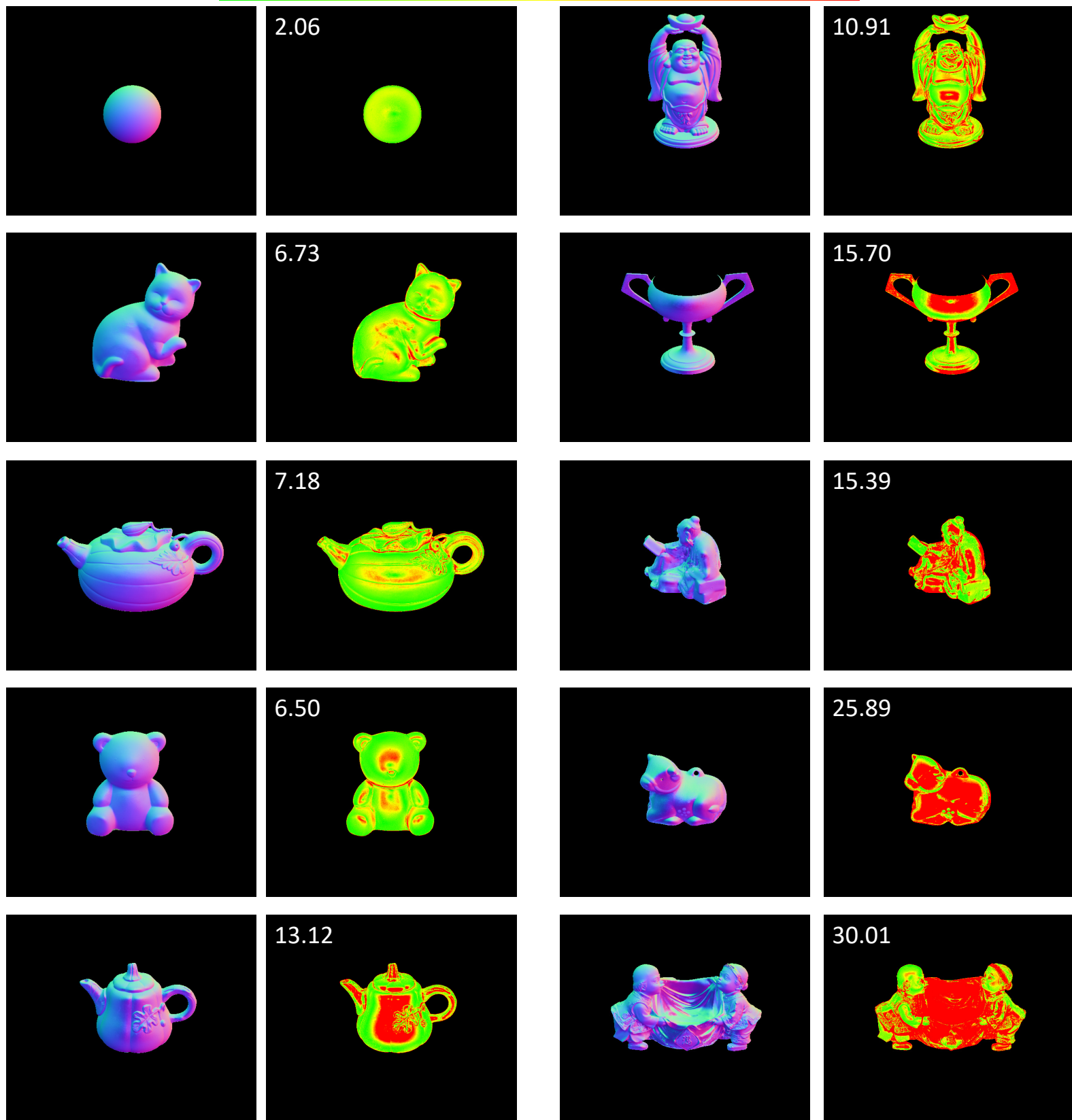
# Part II Footnote 13: Results for all objects and methods in Figure 2

L. Wu, A. Ganesh, B. Shi, Y. Matsushita, Y. Wang, and Y. Ma. Robust photometric stereo via low-rank matrix completion and recovery. In Proc. ACCV, 2010

## WG10

0

20



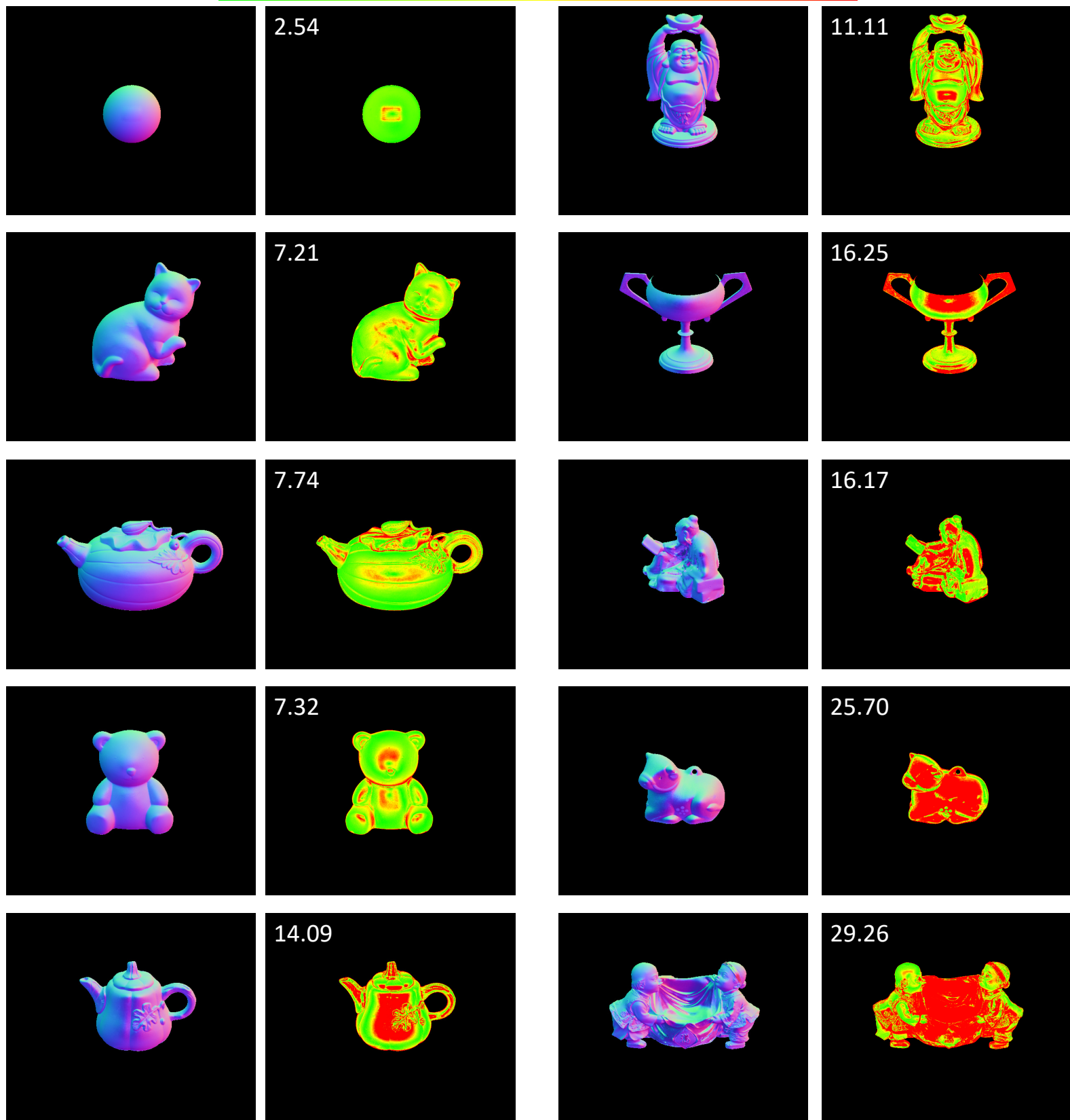
# Part II Footnote 13: Results for all objects and methods in Figure 2

S. Ikehata, D. Wipf, Y. Matsushita, and K. Aizawa. Robust photometric stereo using sparse regression. In Proc. CVPR, 2012

## IW12

0

20



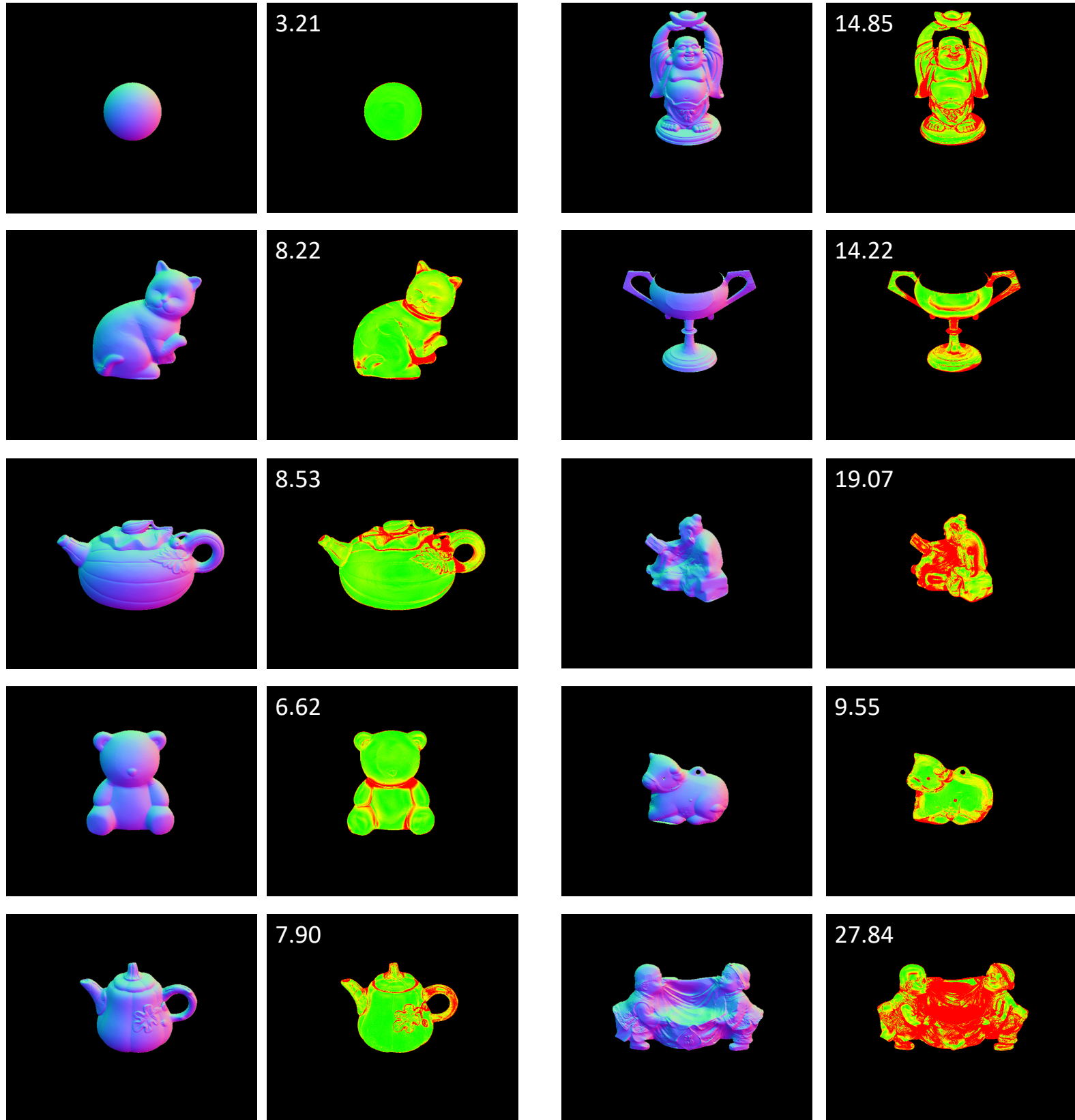
# Part II Footnote 13: Results for all objects and methods in Figure 2

D. B. Goldman, B. Curless, A. Hertzmann, and S. M. Seitz. Shape and spatially-varying BRDFs from photometric stereo. IEEE TPAMI 32(6):1060–1071, 2010

## GC10

0

20



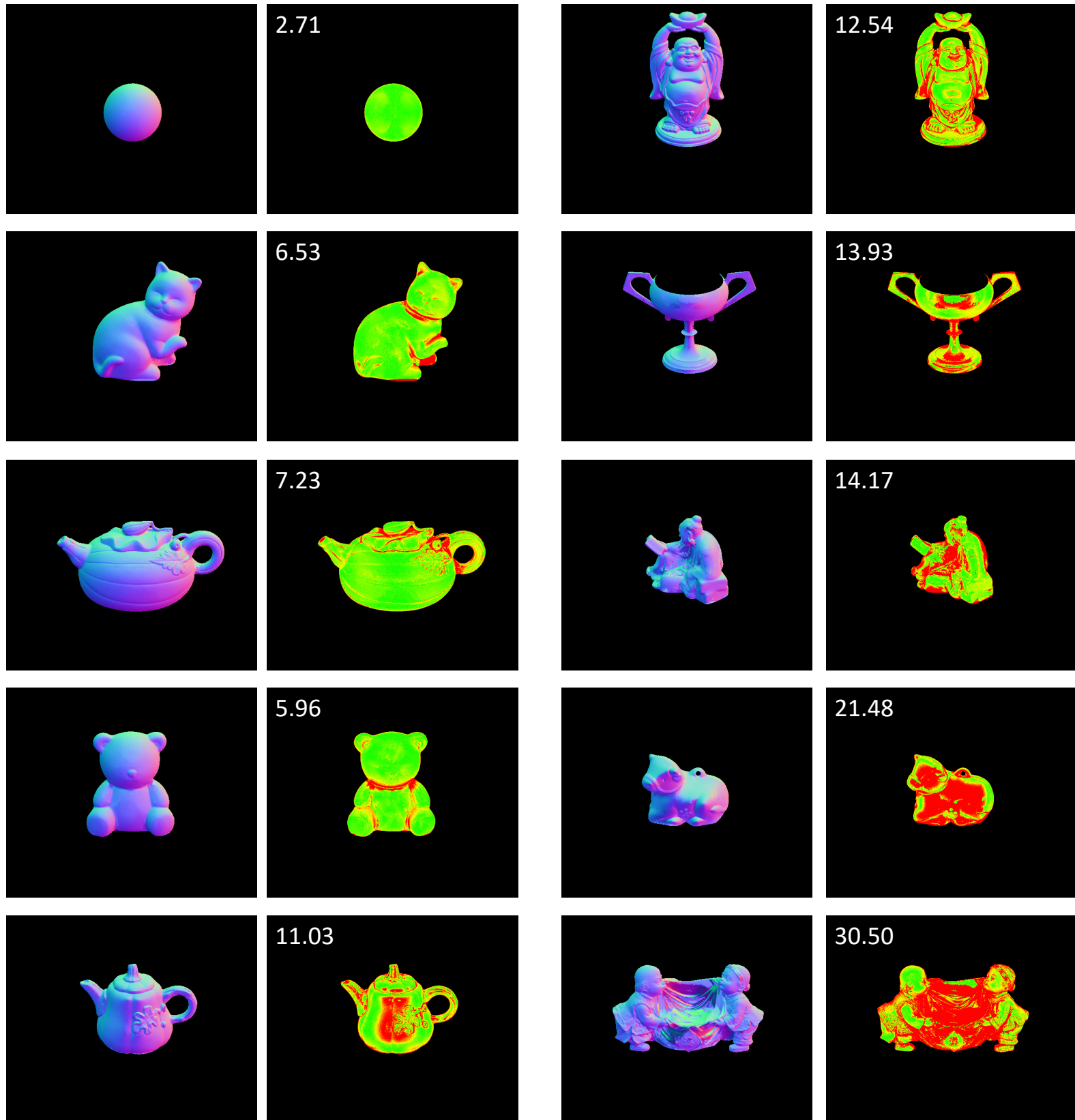
# Part II Footnote 13: Results for all objects and methods in Figure 2

N. G. Alldrin, T. Zickler, and D. J. Kriegman. Photometric stereo with non-parametric and spatially-varying reflectance. In Proc. CVPR, 2008

## AZ08

0

20



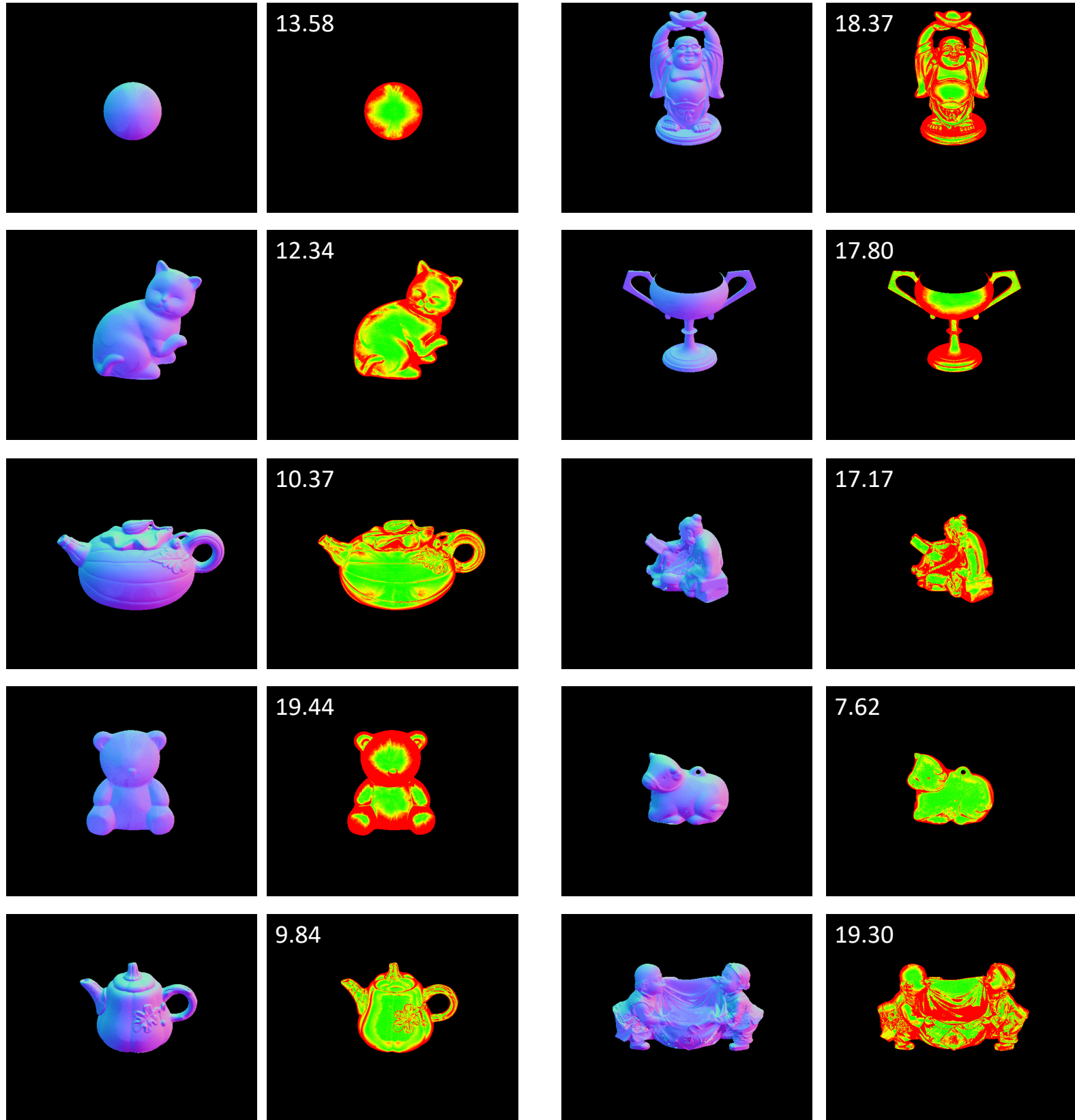
# Part II Footnote 13: Results for all objects and methods in Figure 2

B. Shi, P. Tan, Y. Matsushita, and K. Ikeuchi. Elevation angle from reflectance monotonicity: Photometric stereo for general isotropic reflectances. In Proc. ECCV, 2012

## ST12

0

20



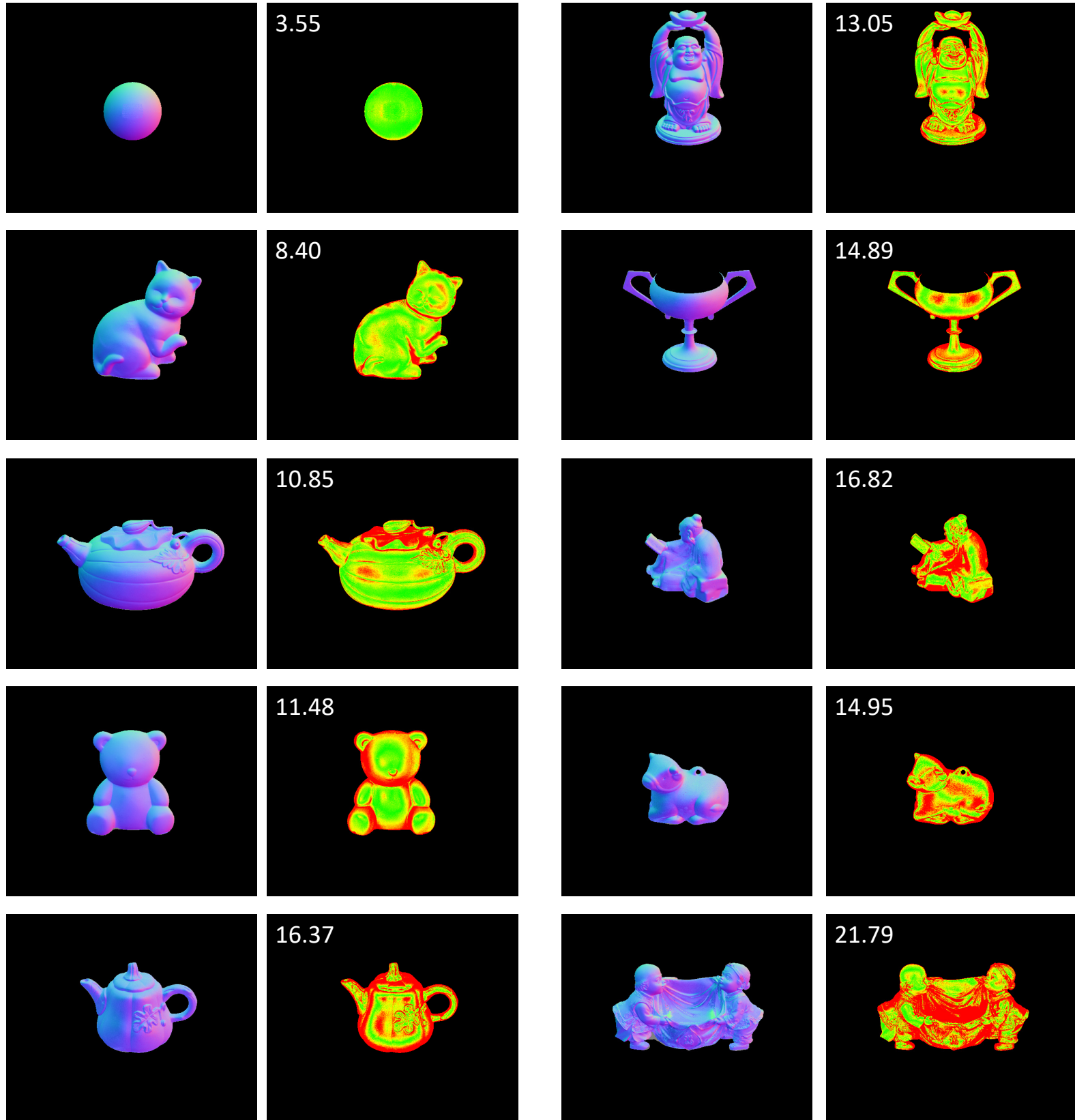
# Part II Footnote 13: Results for all objects and methods in Figure 2

T. Higo, Y. Matsushita, and K. Ikeuchi. Consensus photometric stereo. In Proc. CVPR, 2010

## HM10

0

20



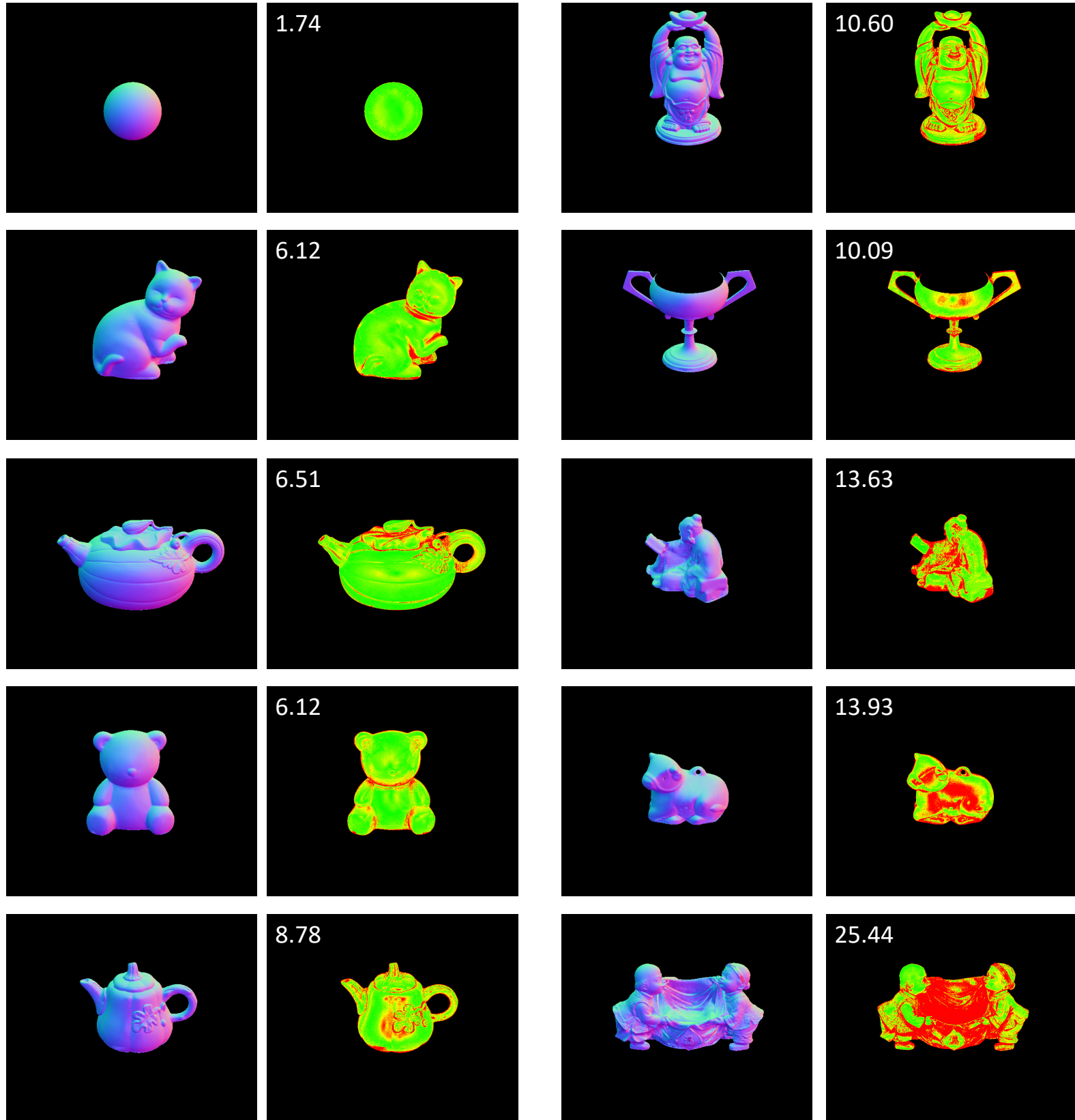
# Part II Footnote 13: Results for all objects and methods in Figure 2

B. Shi, P. Tan, Y. Matsushita, and K. Ikeuchi. Bipolynomial modeling of low-frequency reflectances. IEEE TPAMI 36(6):1078–1091, 2014

## ST14

0

20



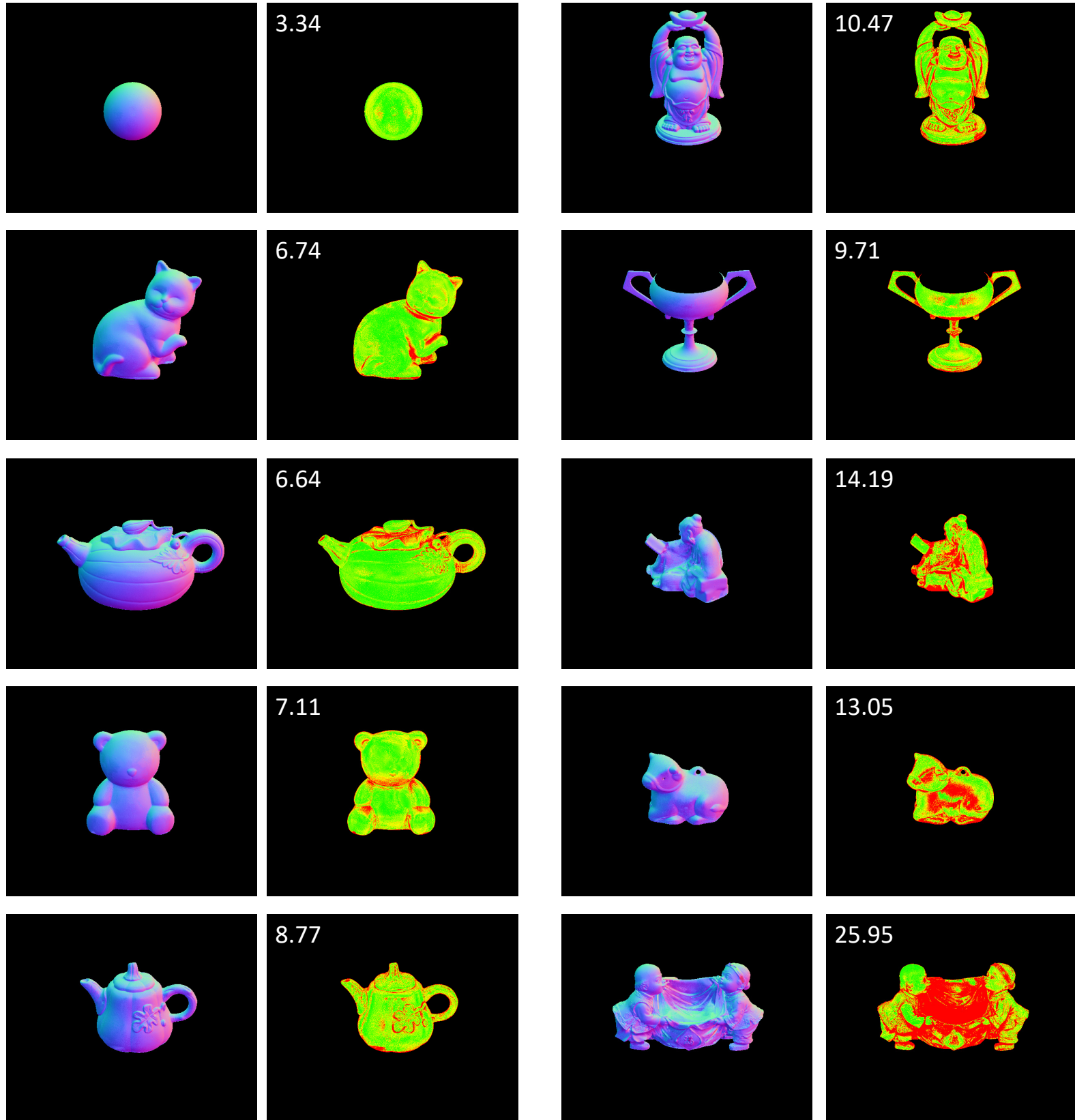
# Part II Footnote 13: Results for all objects and methods in Figure 2

S. Ikehata and K. Aizawa. Photometric stereo using constrained bivariate regression for general isotropic surfaces. In Proc. CVPR, 2014

## IA14

0

20



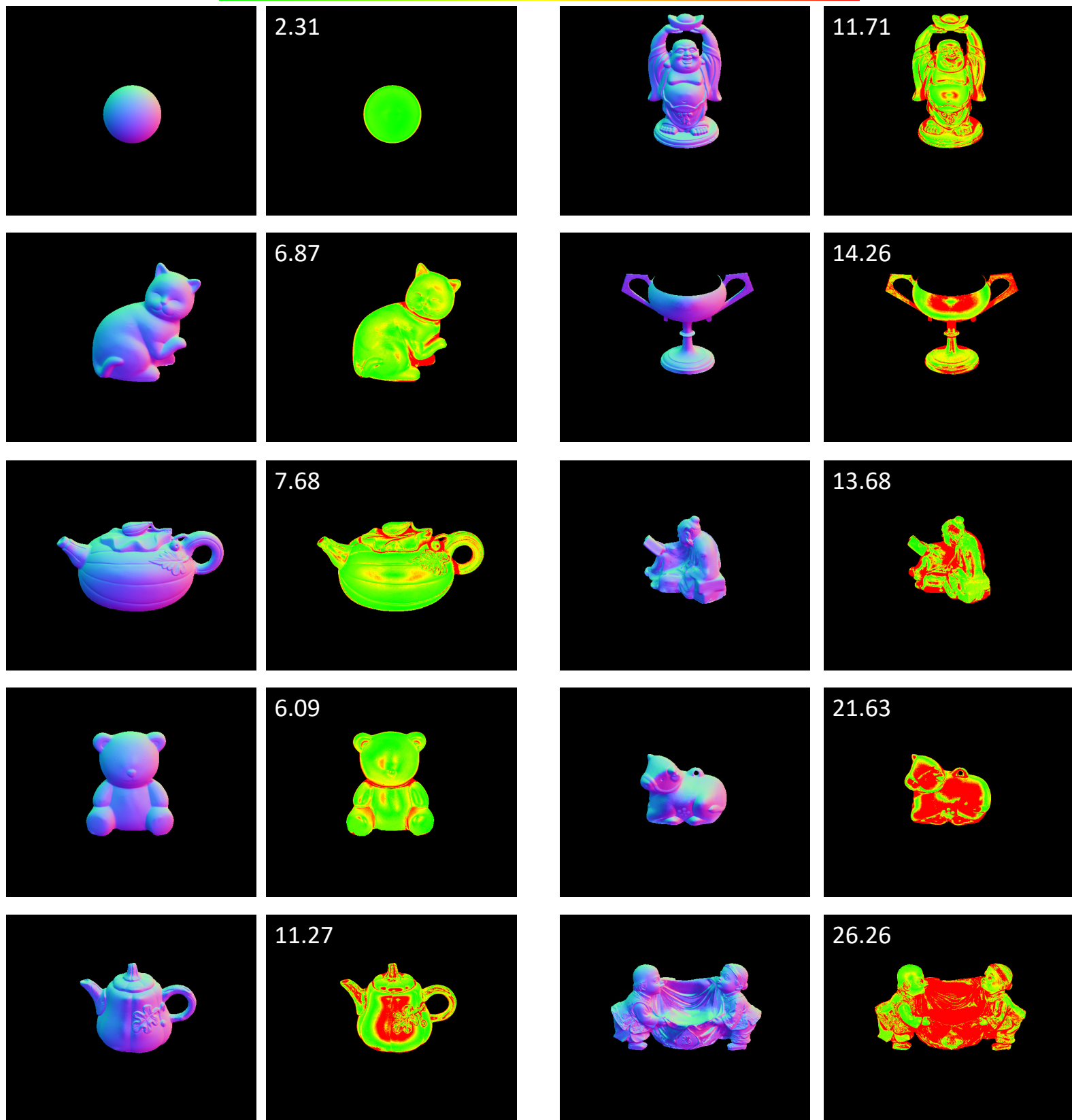
# Part II Footnote 13: Results for all objects and methods in Figure 2

Position threshold with the setting below

(20%, 80%)

0

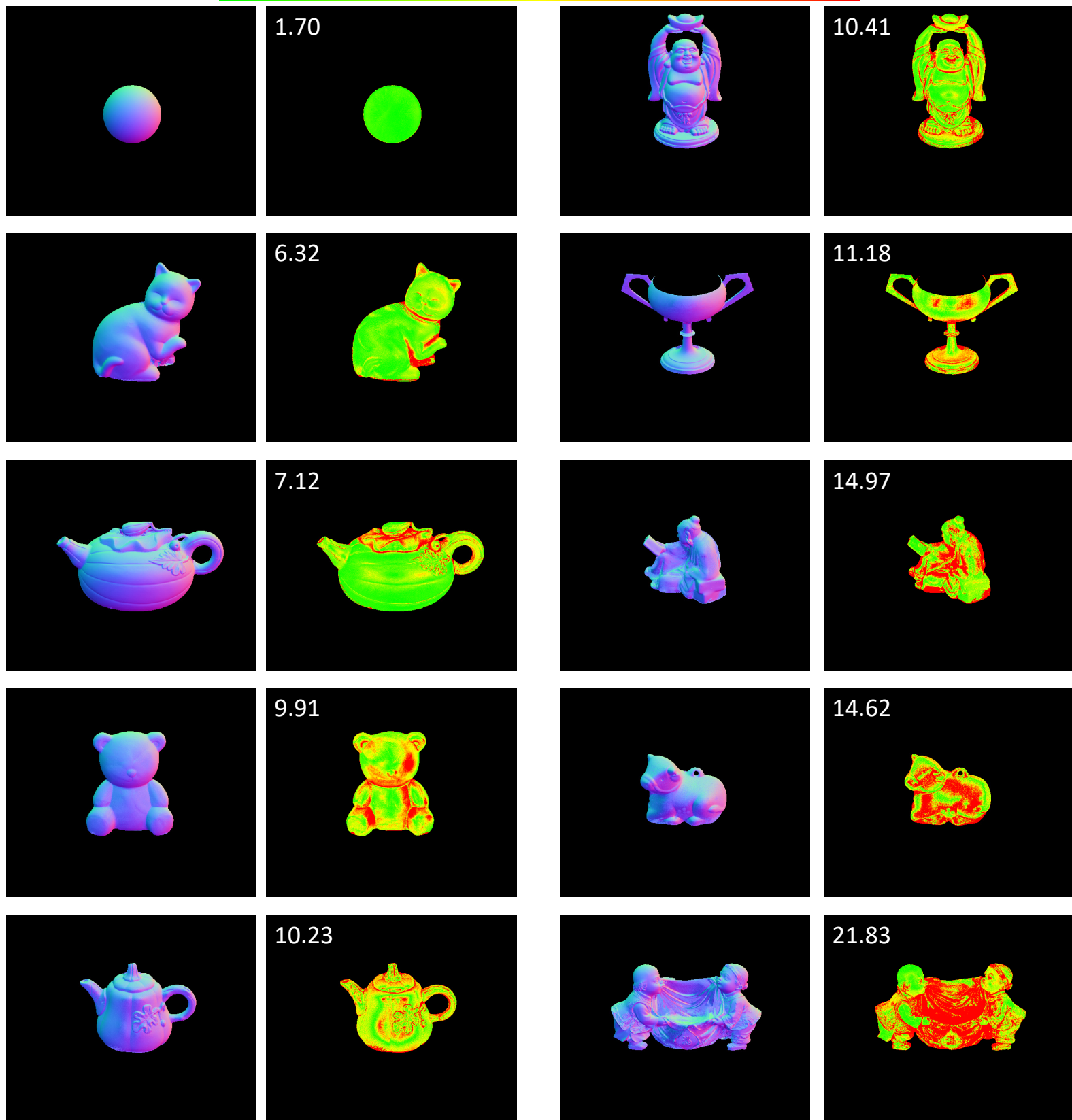
20



# Part II Footnote 13: Results for all objects and methods in Figure 2

Position threshold with the setting below

(40%, 60%)



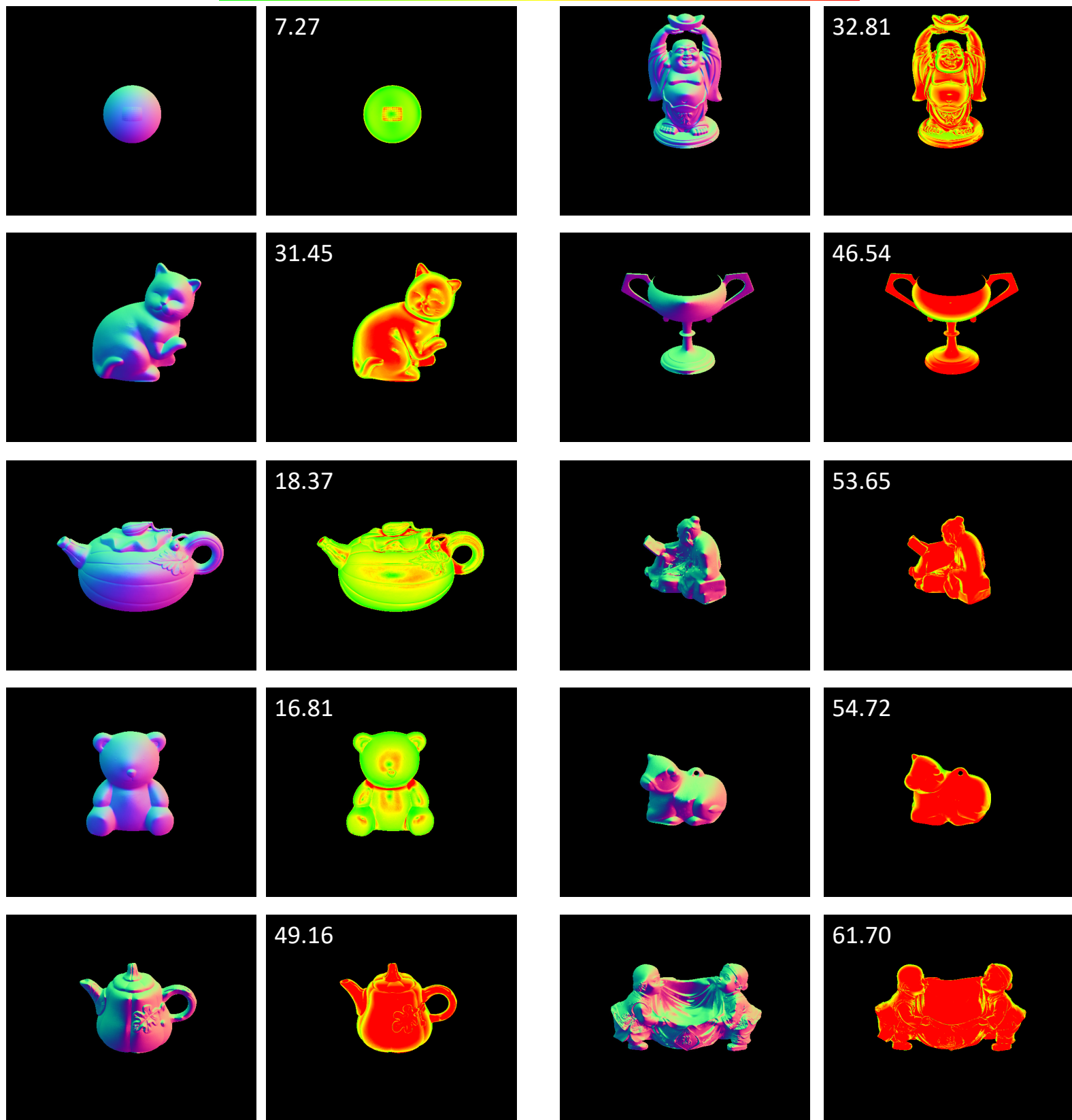
# Part II Footnote 13: Results for all objects and methods in Figure 2

N. G. Aldrin, S. P. Mallick, and D. J. Kriegman. Resolving the generalized bas-relief ambiguity by entropy minimization. In Proc. CVPR, 2007

## AM07

0

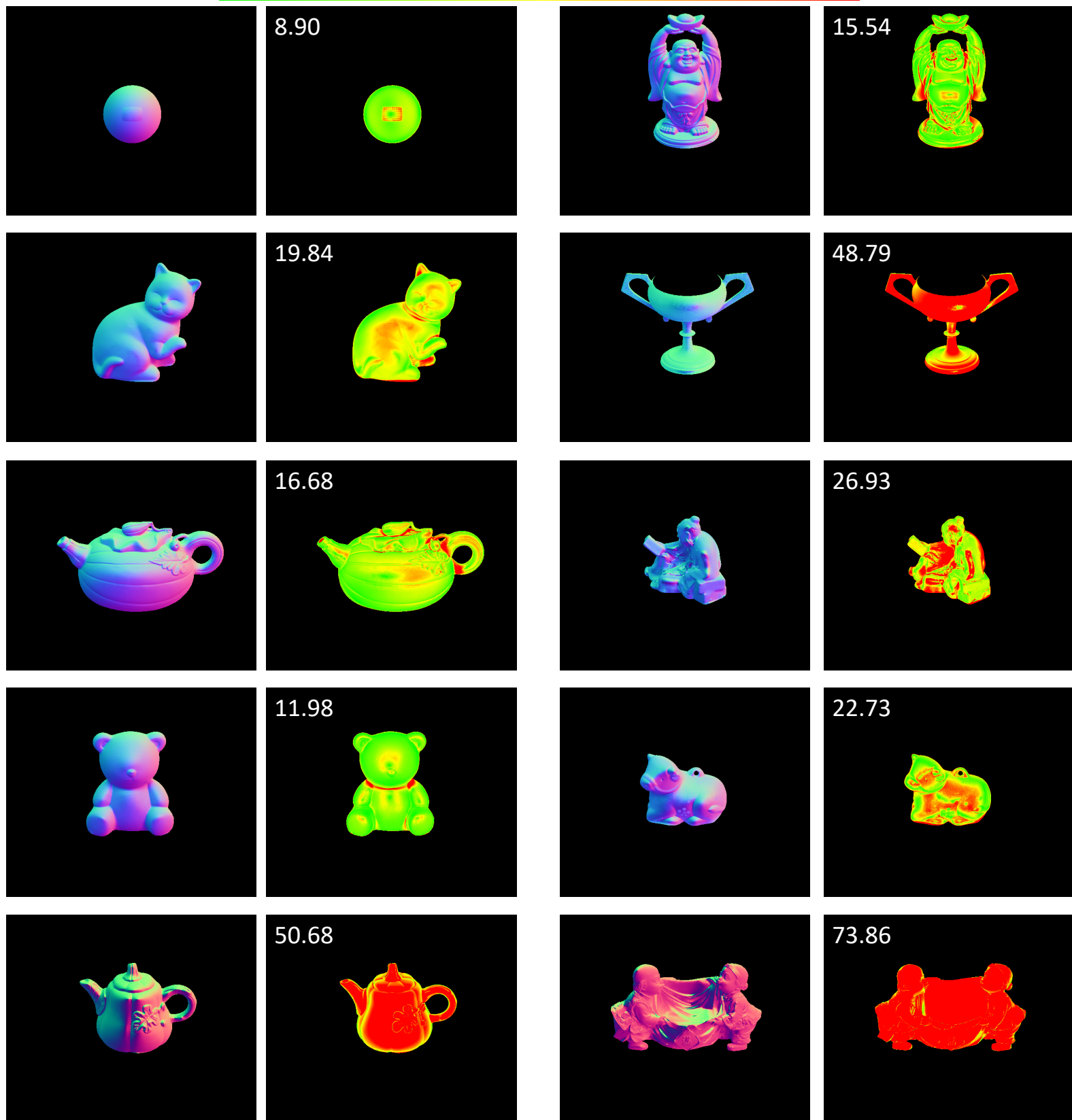
20



# Part II Footnote 13: Results for all objects and methods in Figure 2

B. Shi, Y. Matsushita, Y. Wei, C. Xu, and P. Tan. Self-calibrating photometric stereo.

## SM10



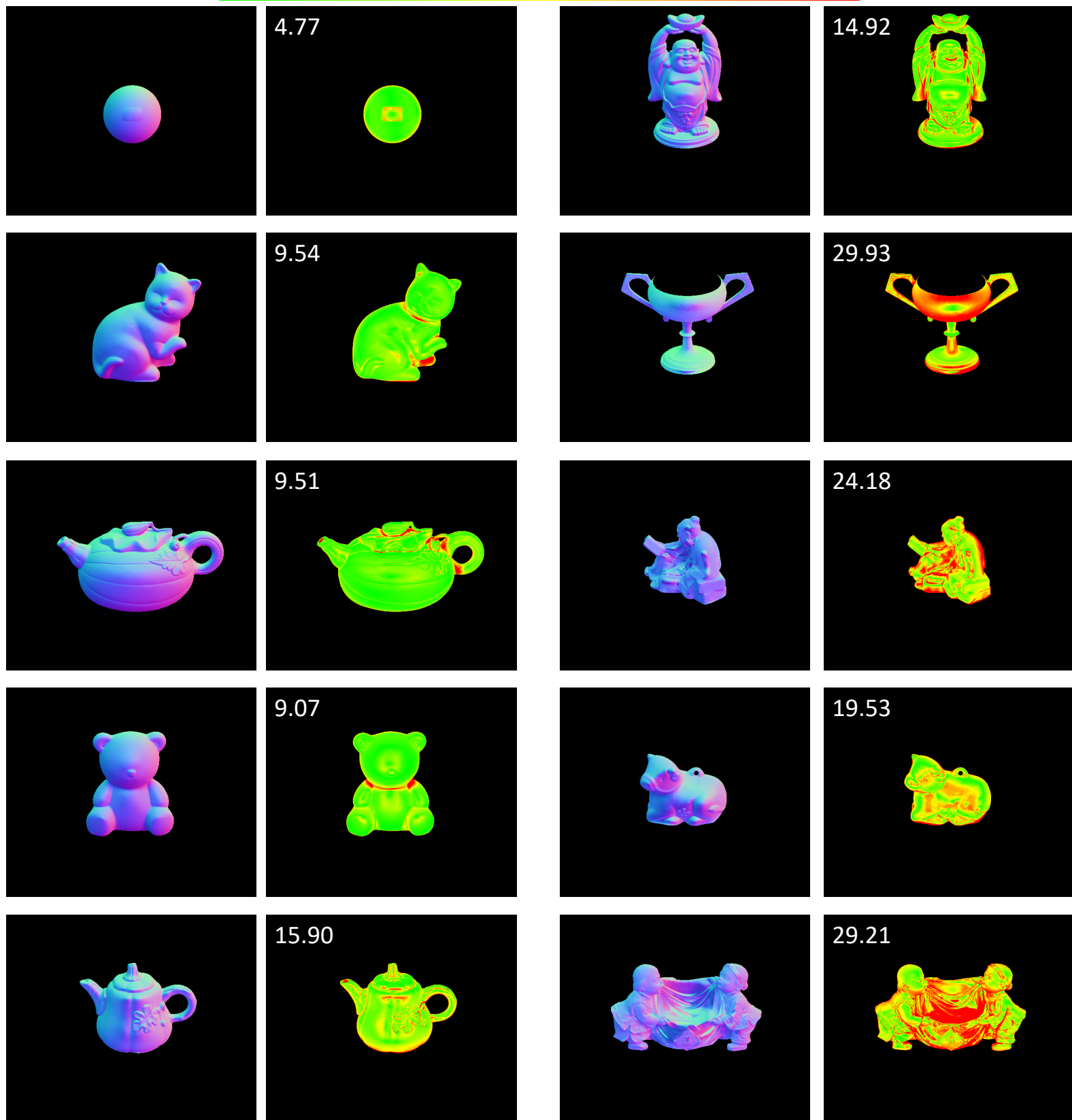
# Part II Footnote 13: Results for all objects and methods in Figure 2

T. Papadhimetri and P. Favaro. A closed-form, consistent and robust solution to uncalibrated photometric stereo via local diffuse reflectance maxima. IJCV 107(2):139–154, 2014

## PF14

0

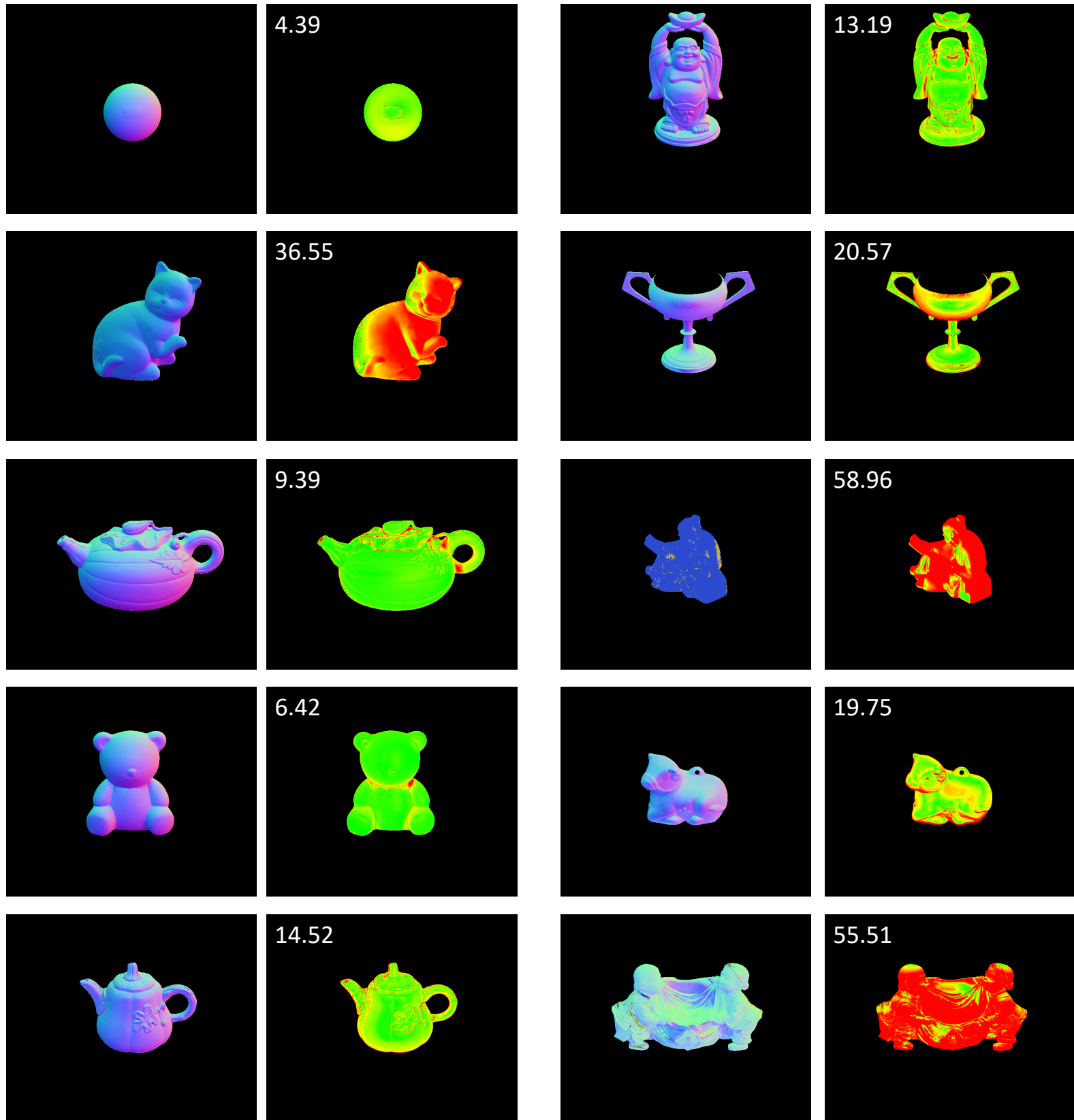
20



# Part II Footnote 13: Results for all objects and methods in Figure 2

Z. Wu and P. Tan. Calibrating photometric stereo by holistic reflectance symmetry analysis. In Proc. CVPR, 2013

## WT13



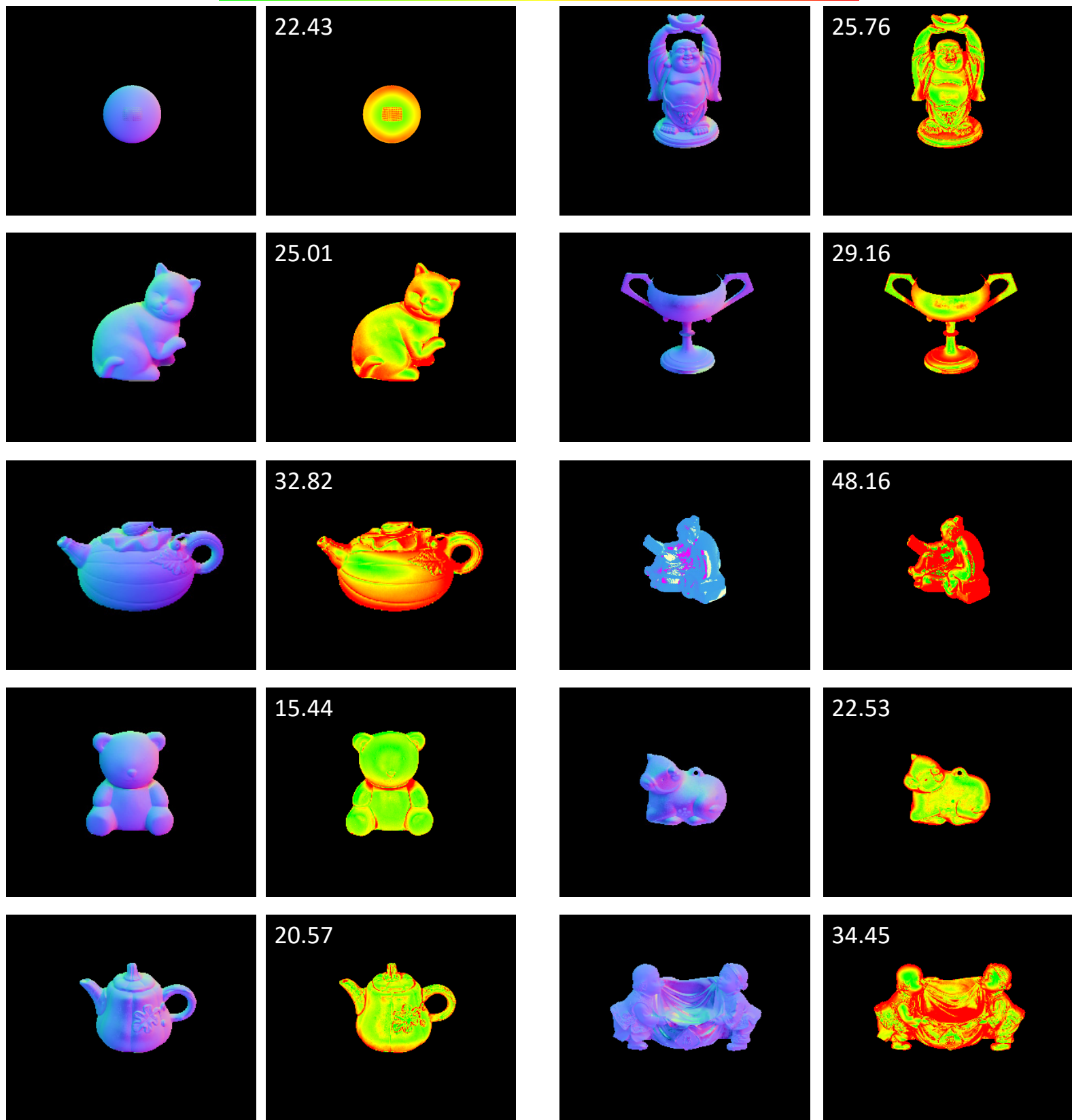
# Part II Footnote 13: Results for all objects and methods in Figure 2

F. Lu, Y. Matsushita, I. Sato, T. Okabe, and Y. Sato. Uncalibrated photometric stereo for unknown isotropic reflectances. In Proc. CVPR, 2013

## LM13

0

20



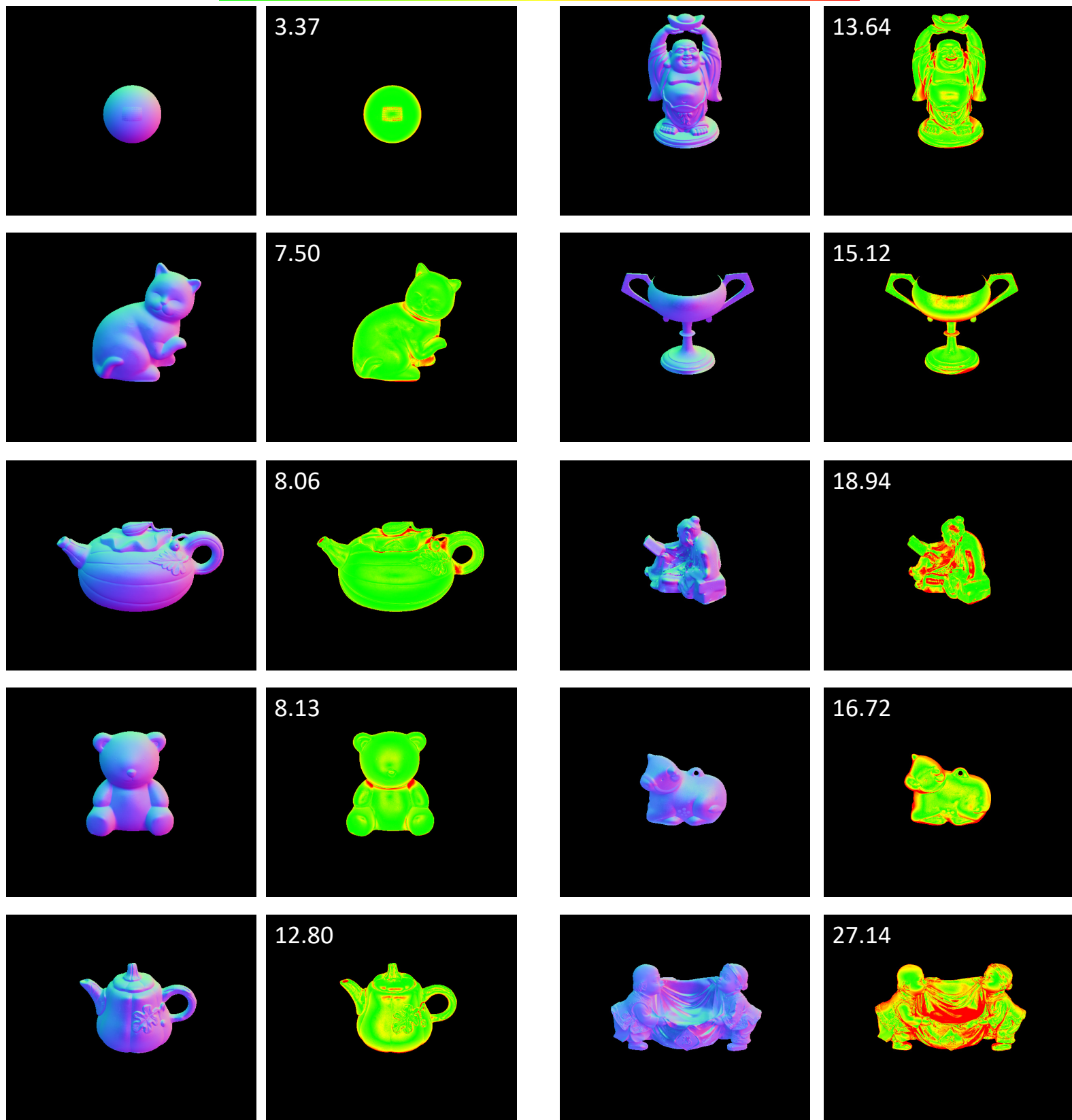
# Part II Footnote 13: Results for all objects and methods in Figure 2

Resolving the linear ambiguity matrix  $A$  with the 'ground truth'

## Opt. A

0

20



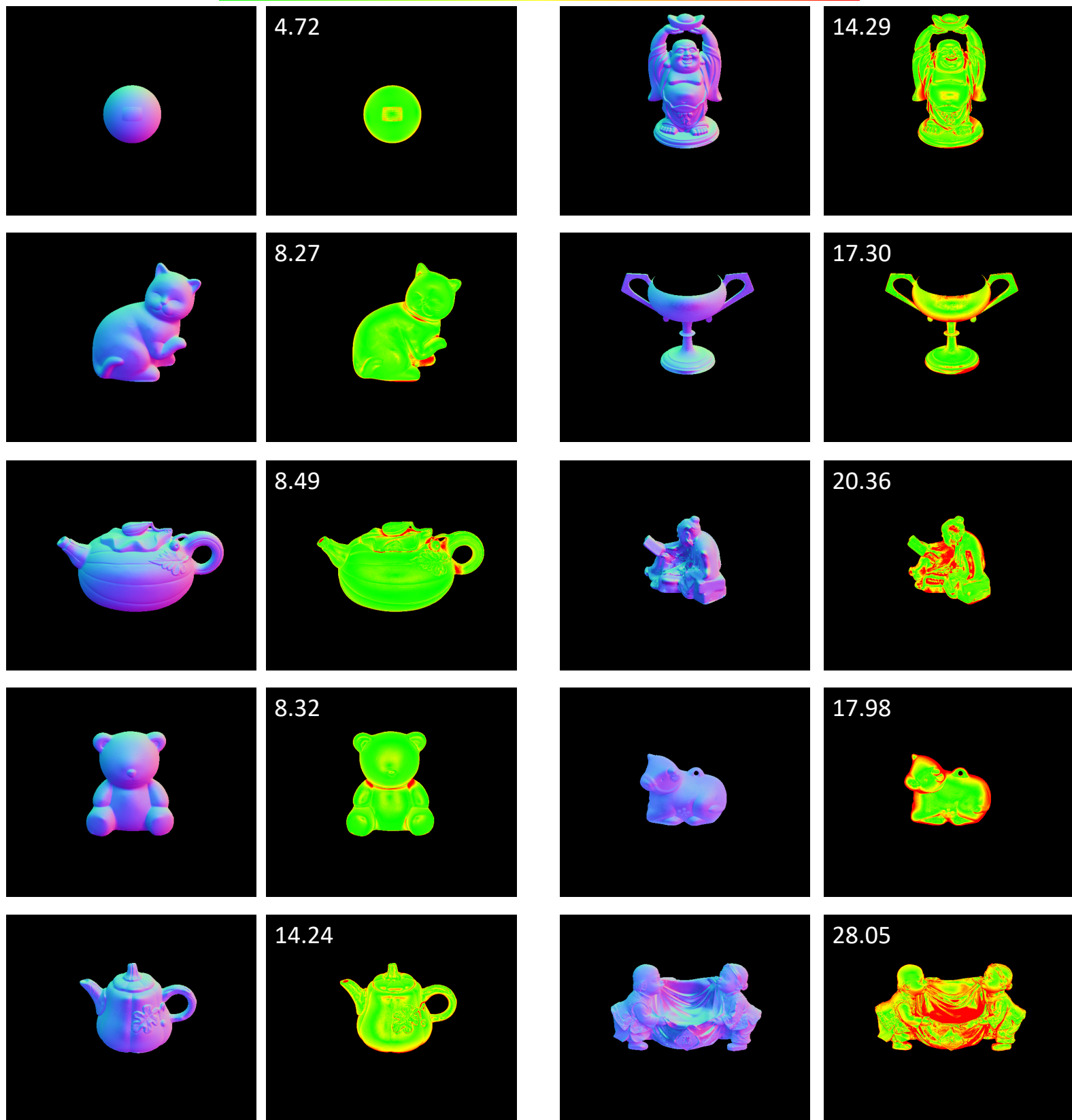
# Part II Footnote 13: Results for all objects and methods in Figure 2

Resolving the GBR ambiguity matrix  $G$  with the 'ground truth'

## Opt. G

0

20



**Part III** Footnote 16: Complete version of Figure 4 for all objects

Error inducing rate



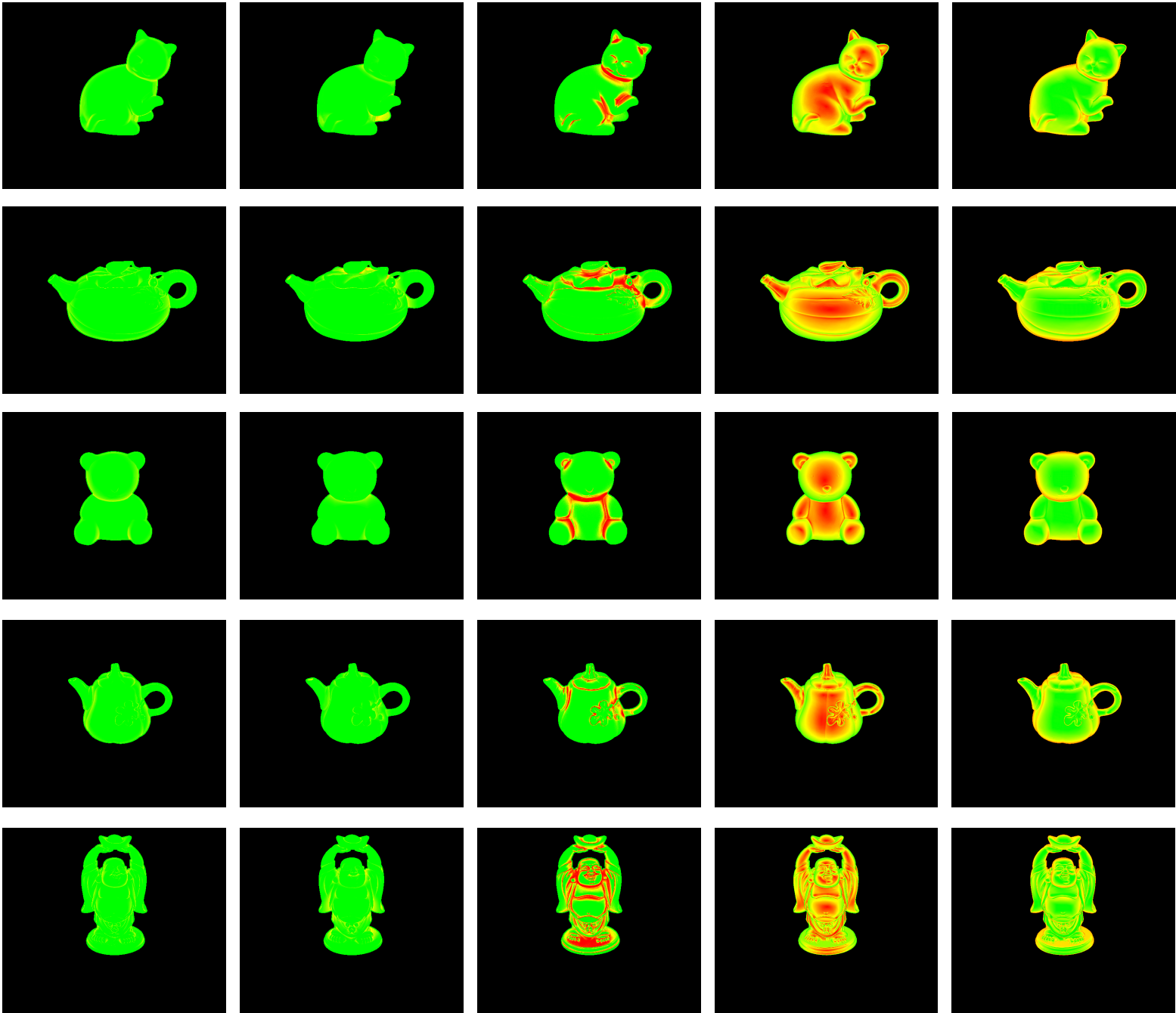
Attached shadow

Cast shadow

Interreflection

Elevation angle

Minimum half angle



**Part III** Footnote 16: Complete version of Figure 4 for all objects

Error inducing rate



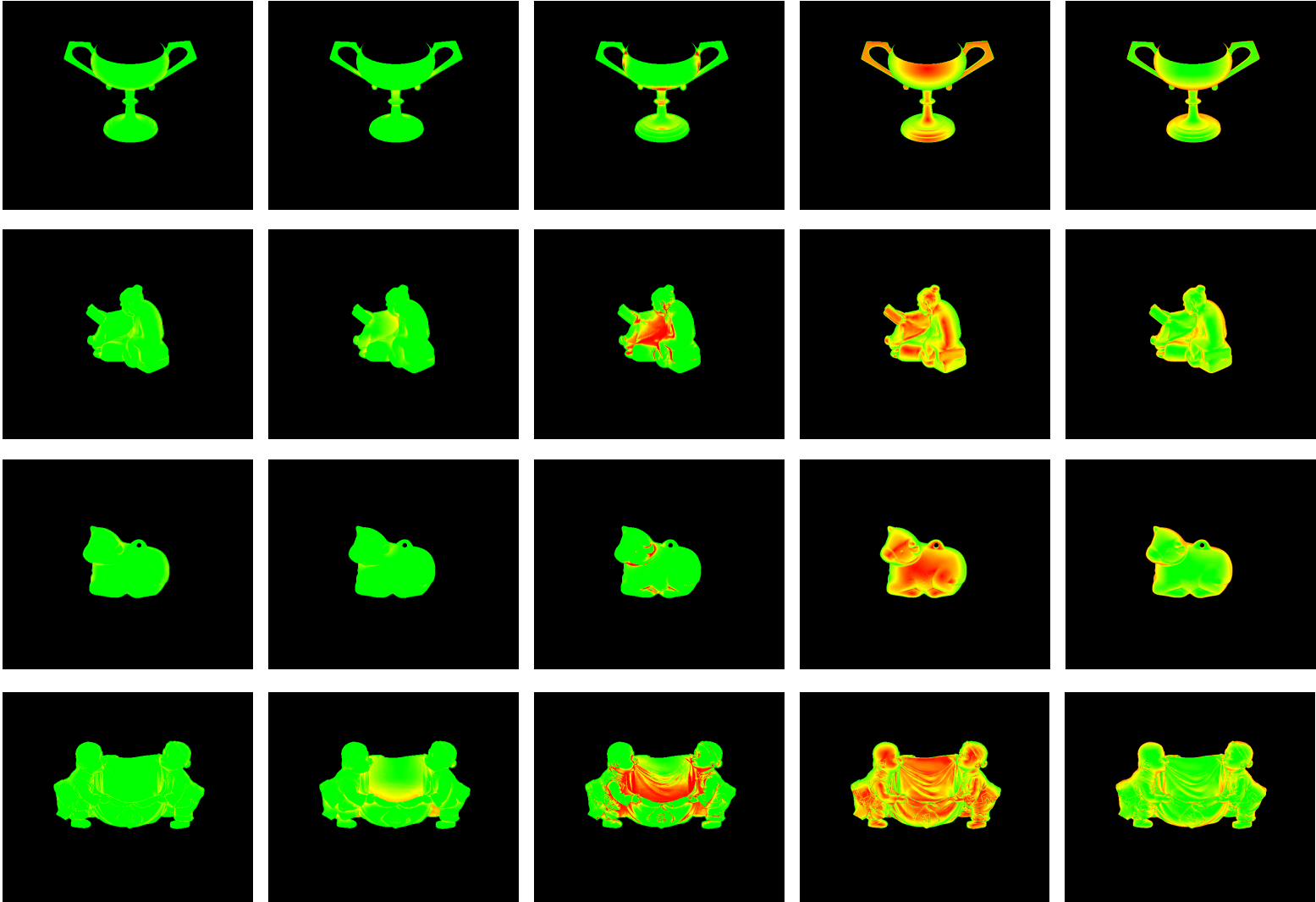
Attached shadow

Cast shadow

Interreflection

Elevation angle

Minimum half angle

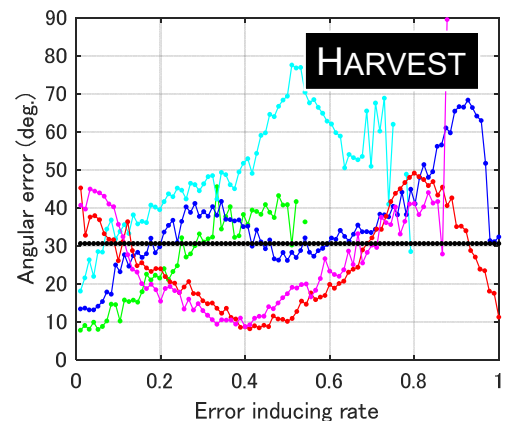
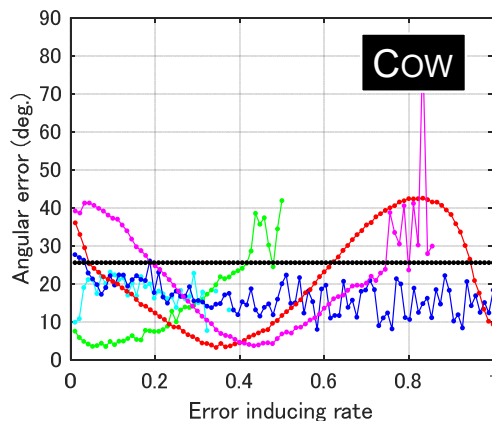
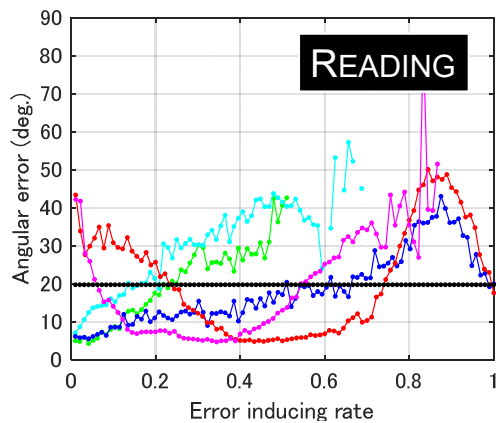
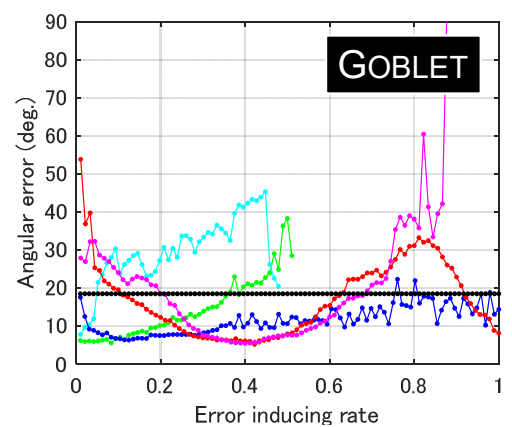
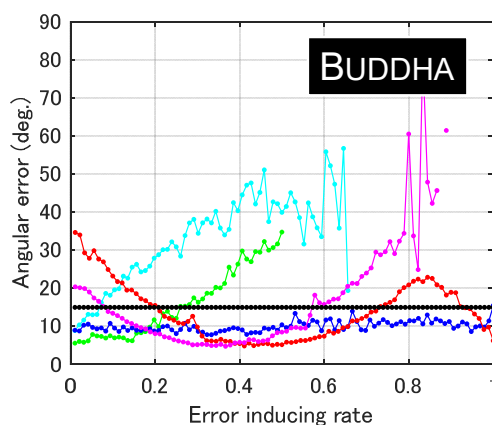
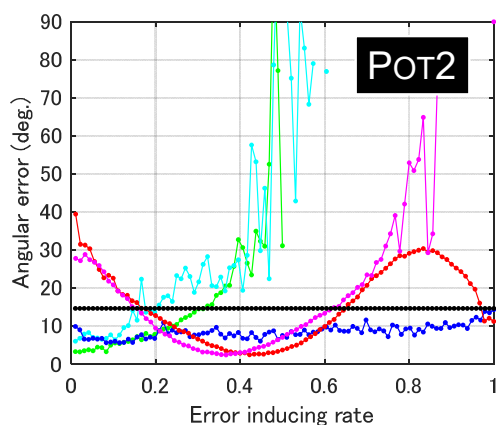
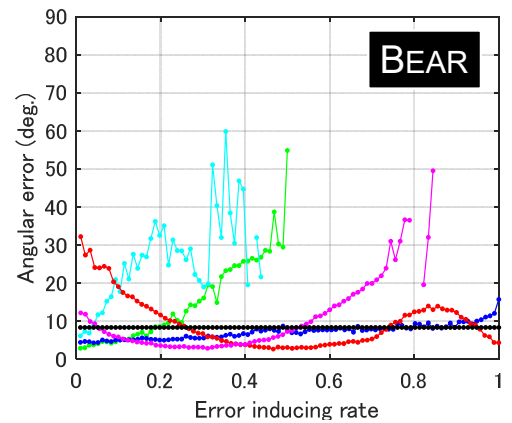
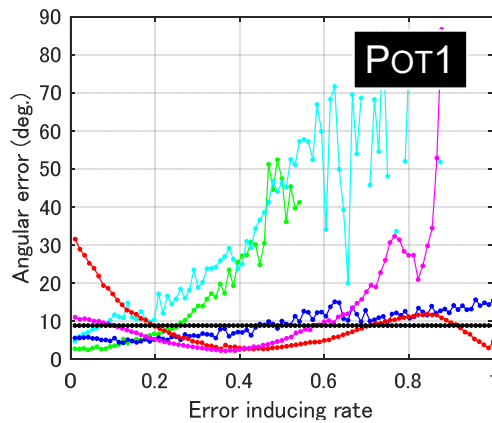
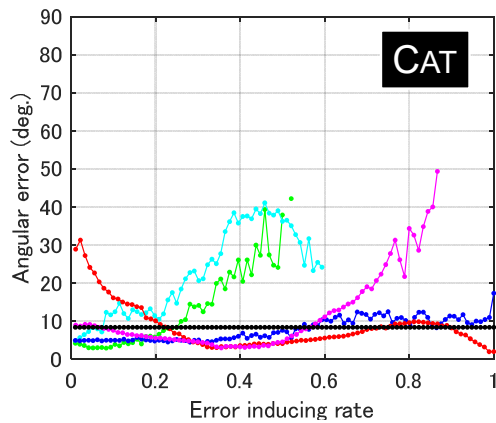
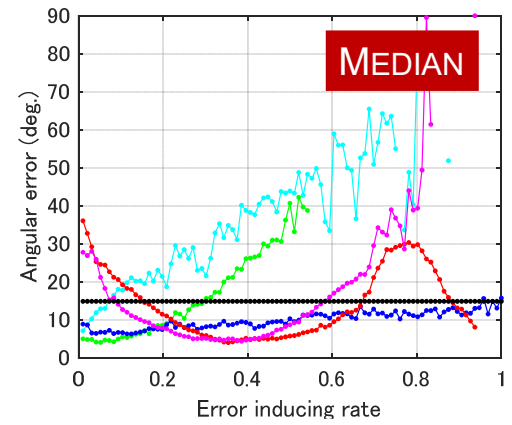


# Part III Footnote 17: Complete Figure 5

## Non-Lambertian methods

### BASELINE

R. J. Woodham. Photometric method for determining surface orientation from multiple images. *Optical Engineering* 19(1):139–144, 1980

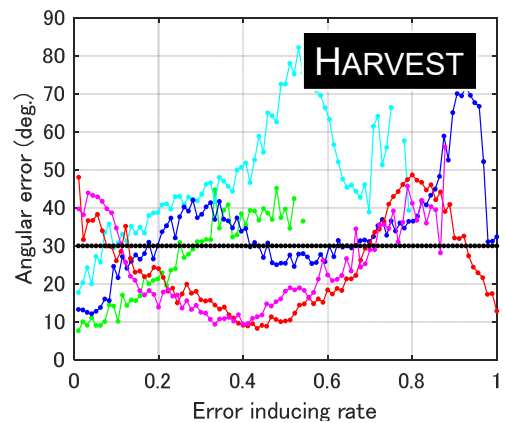
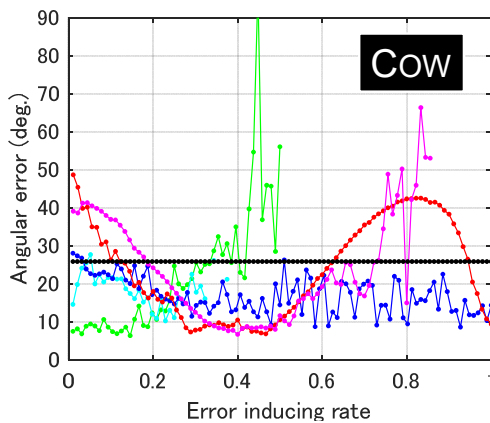
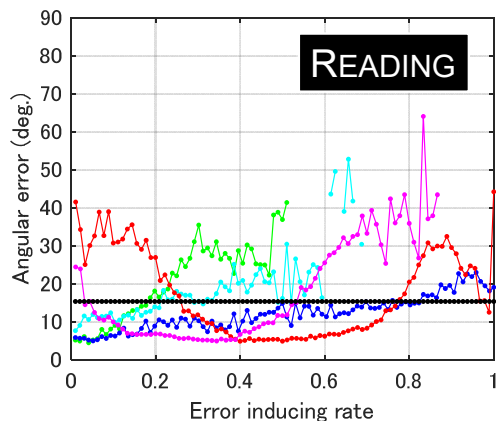
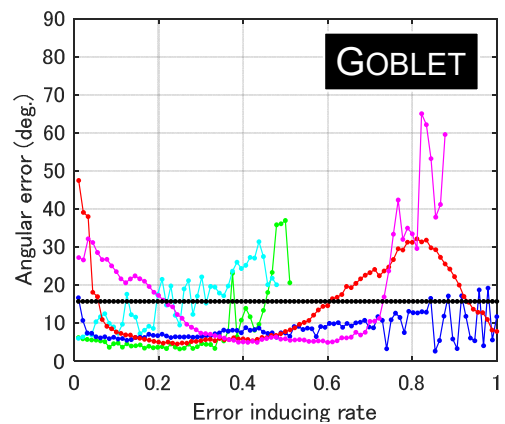
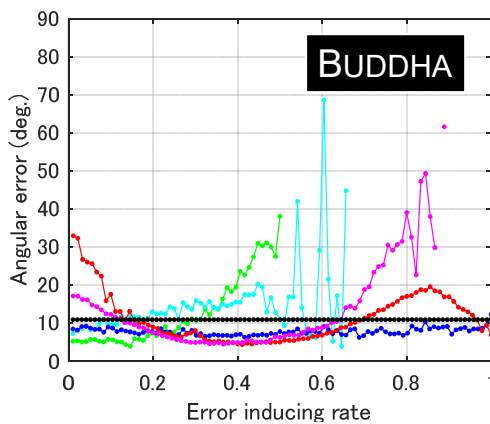
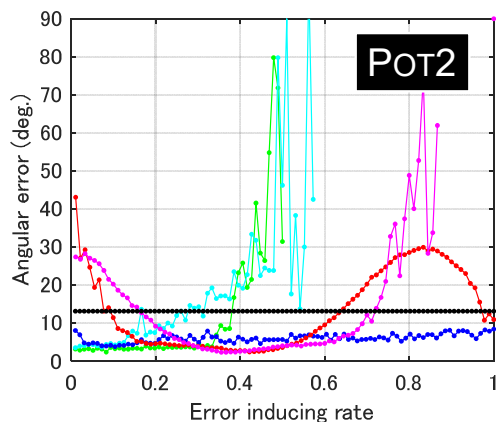
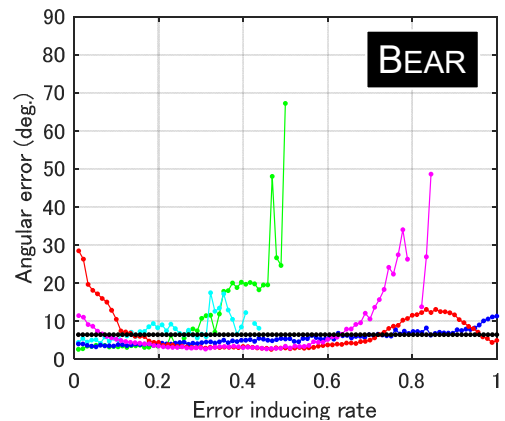
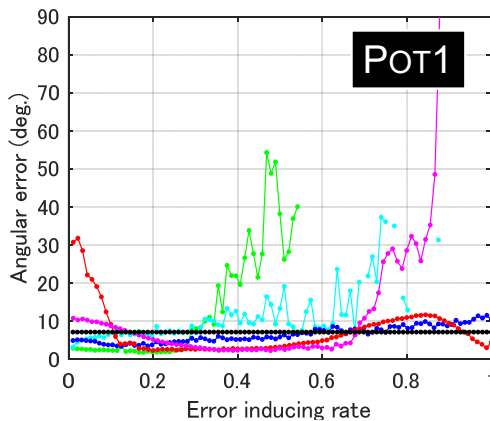
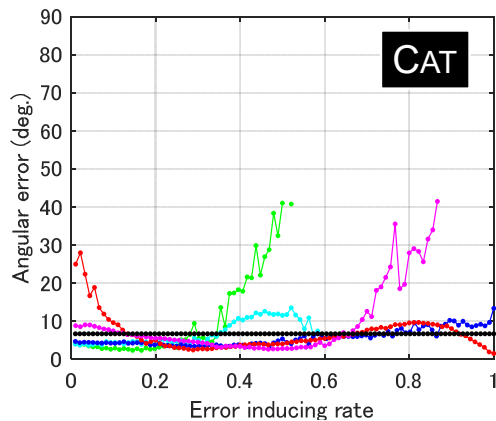
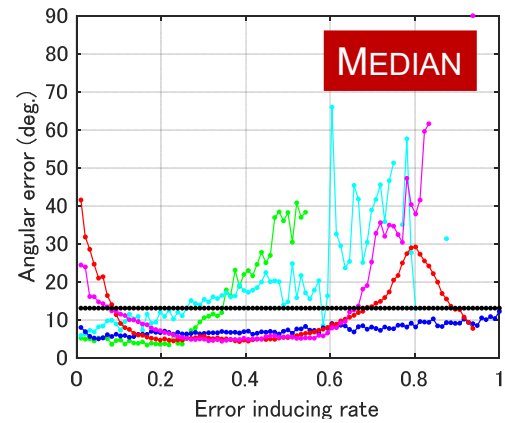


# Part III Footnote 17: Complete Figure 5

## Non-Lambertian methods

### WG10

L. Wu, A. Ganesh, B. Shi, Y. Matsushita, Y. Wang, and Y. Ma.  
Robust photometric stereo via low-rank matrix completion and recovery. In Proc. ACCV, 2010



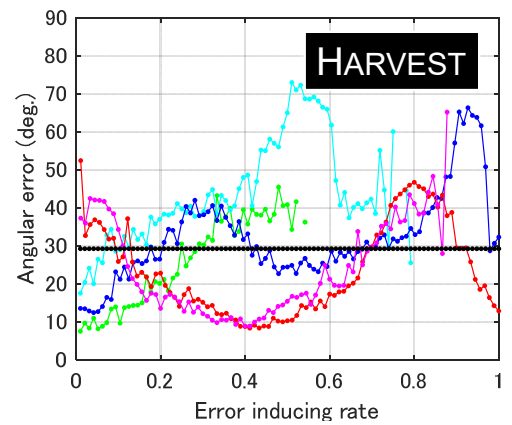
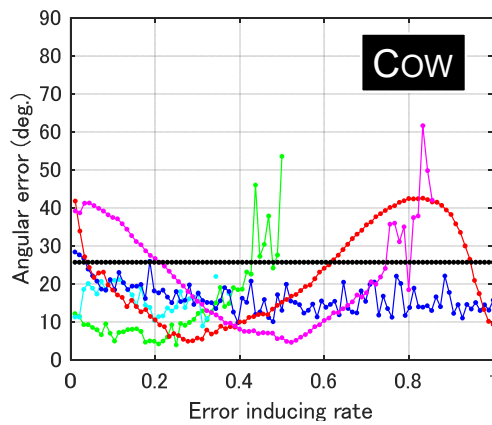
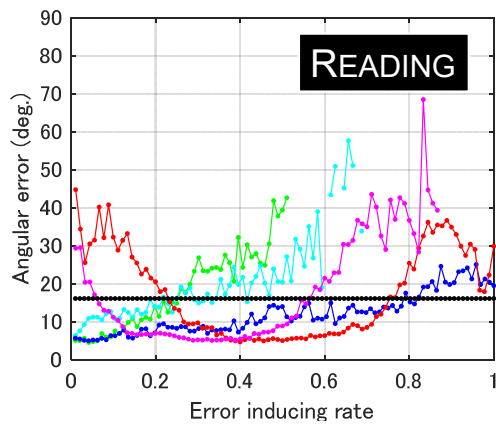
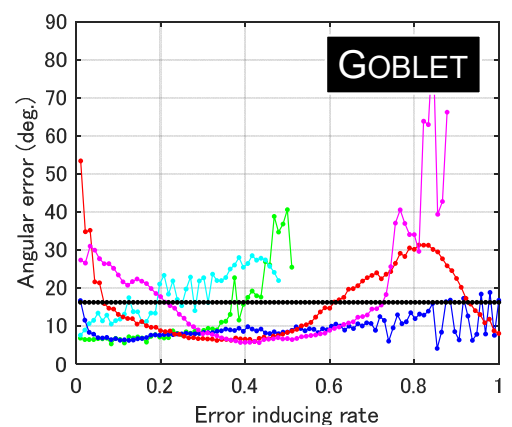
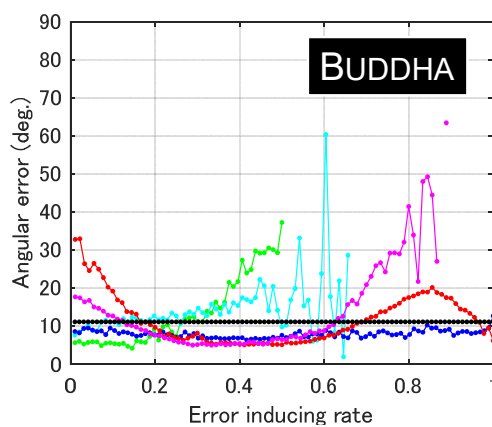
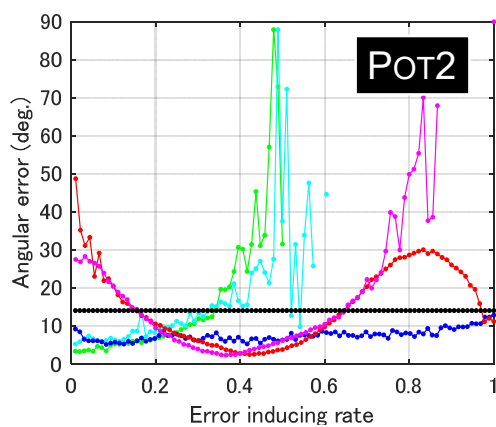
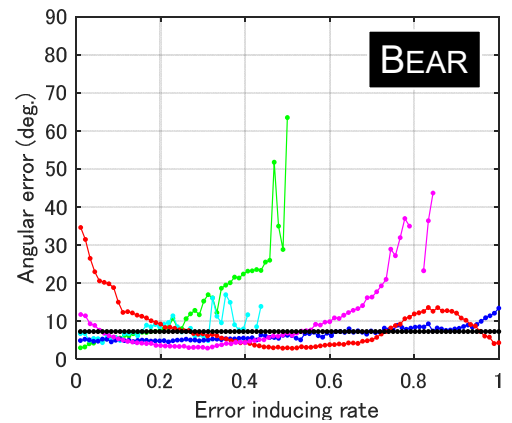
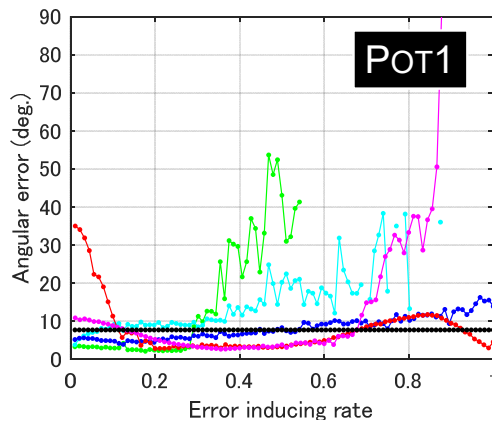
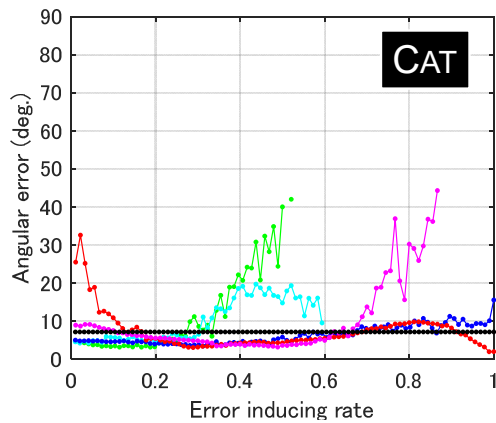
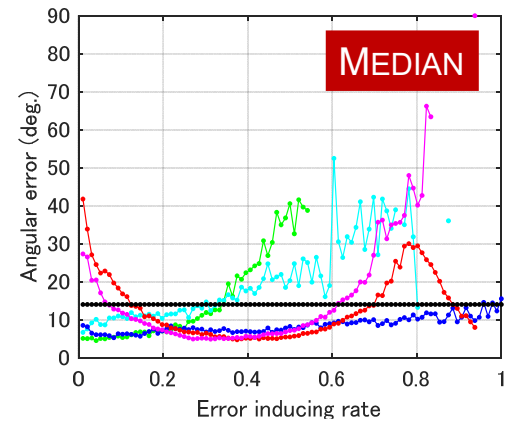
Attached shadow    Cast shadow    Interreflection    Elevation angle    Minimum half angle    Average

# Part III Footnote 17: Complete Figure 5

## Non-Lambertian methods

### IW12

S. Ikehata, D. Wipf, Y. Matsushita, and K. Aizawa. Robust photometric stereo using sparse regression. In Proc. CVPR, 2012

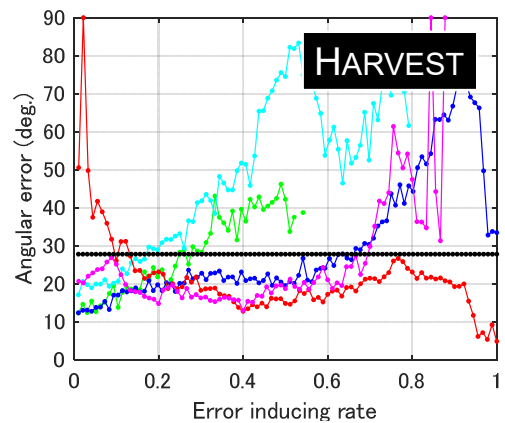
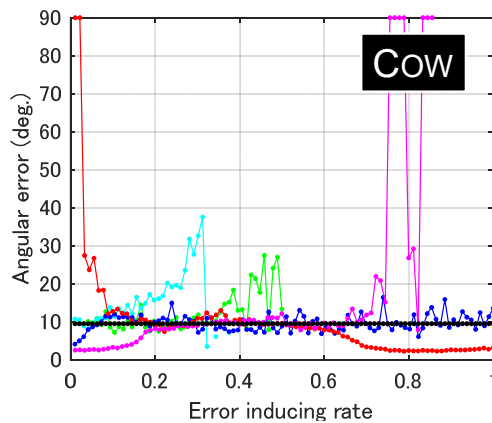
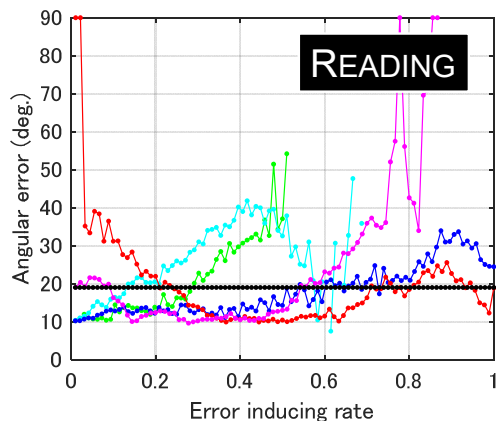
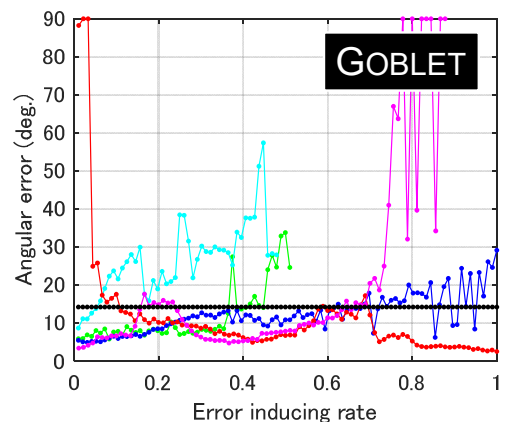
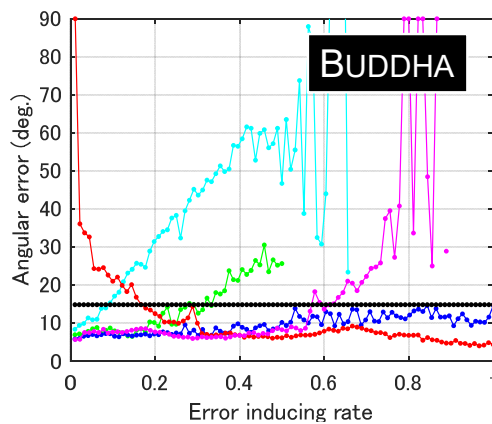
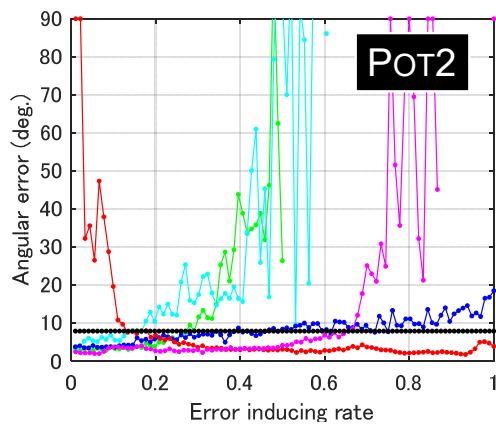
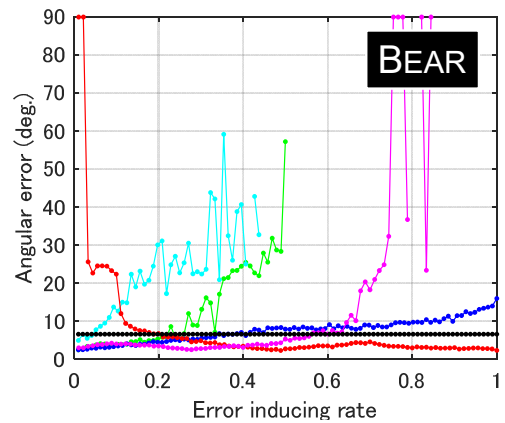
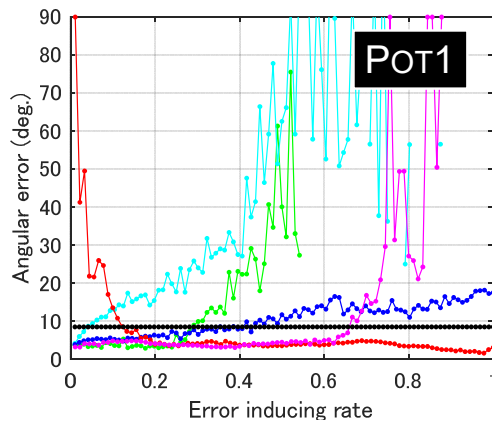
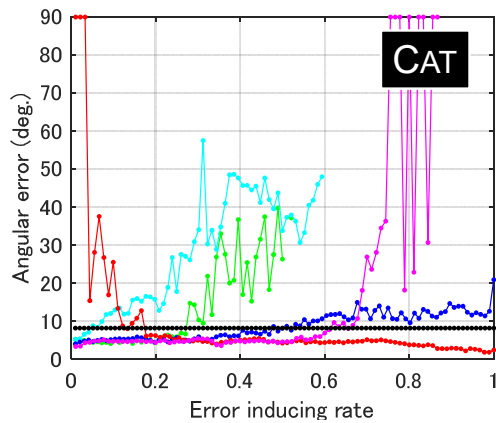
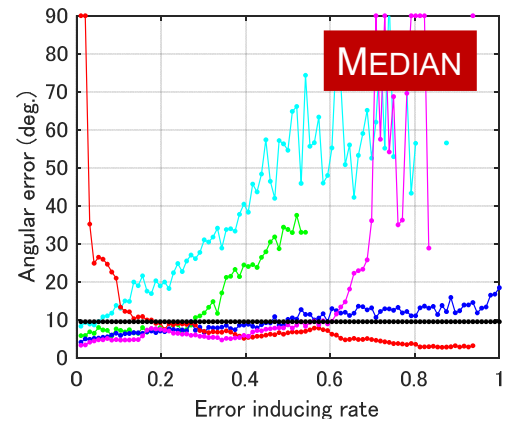


# Part III Footnote 17: Complete Figure 5

## Non-Lambertian methods

### GC10

D. B. Goldman, B. Curless, A. Hertzmann, and S. M. Seitz. Shape and spatially-varying BRDFs from photometric stereo. IEEE TPAMI 32(6):1060–1071, 2010



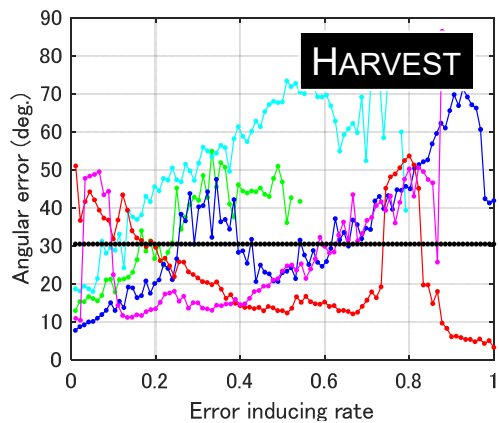
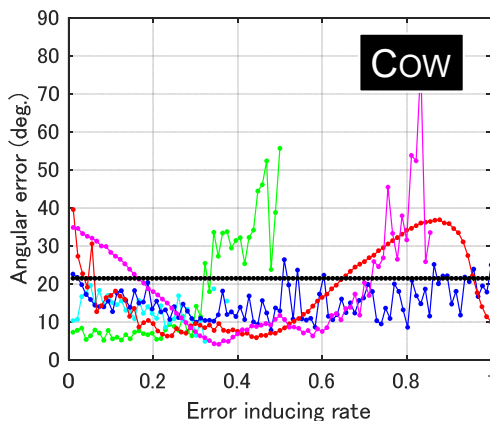
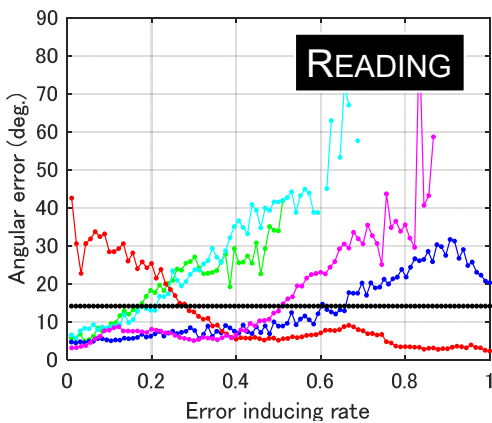
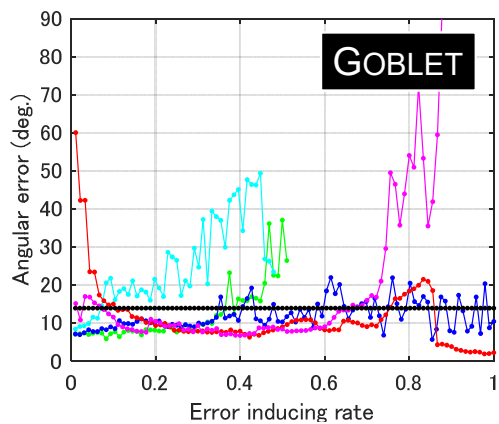
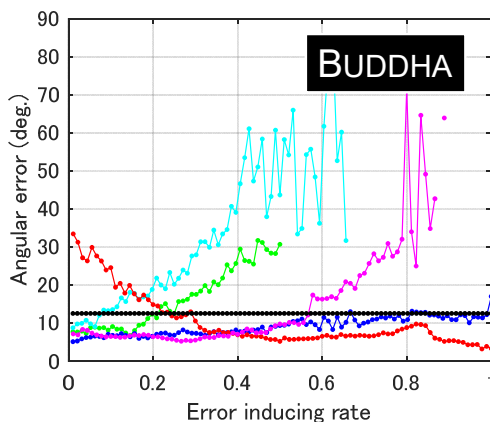
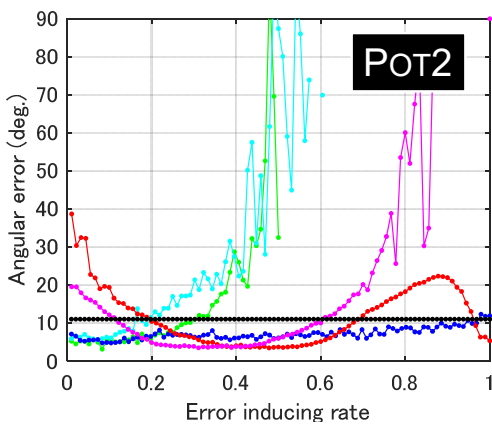
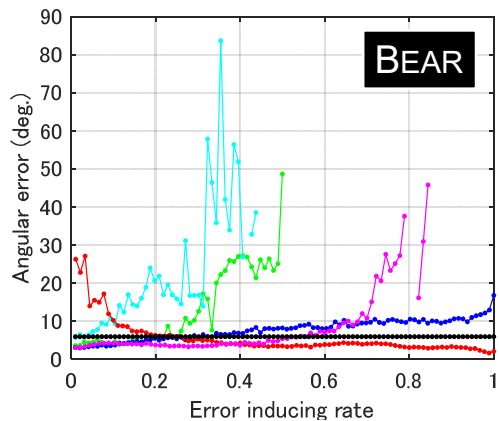
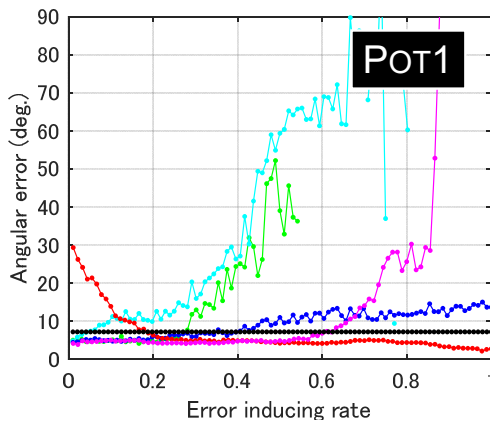
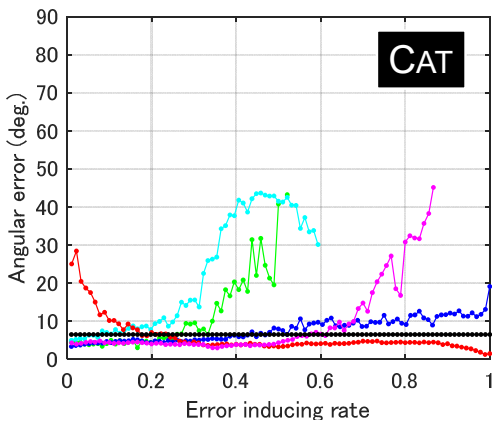
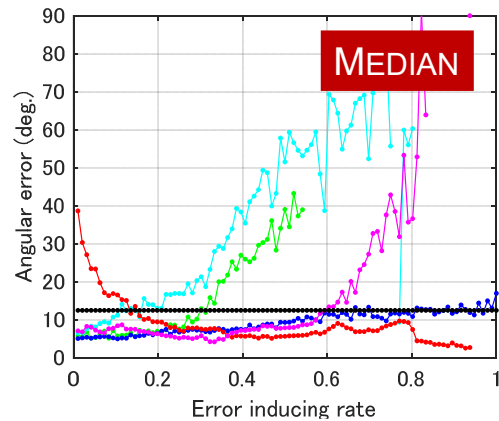
Attached shadow Cast shadow Interreflection Elevation angle Minimum half angle Average

# Part III Footnote 17: Complete Figure 5

## Non-Lambertian methods

### AZ08

N. G. Aldrin, T. Zickler, and D. J. Kriegman. Photometric stereo with non-parametric and spatially-varying reflectance. In Proc. CVPR, 2008



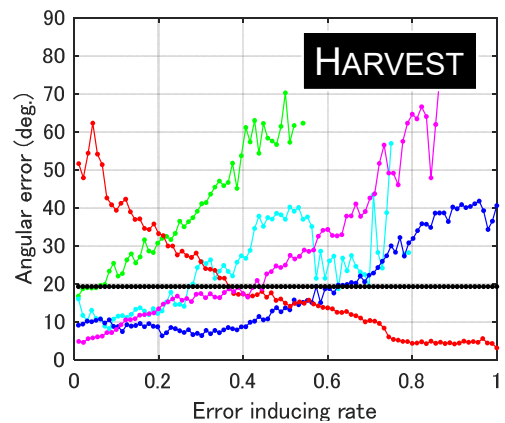
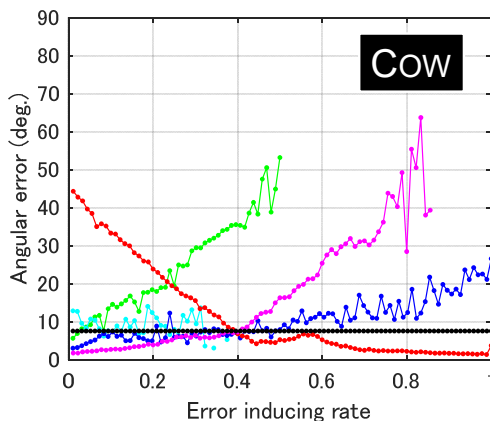
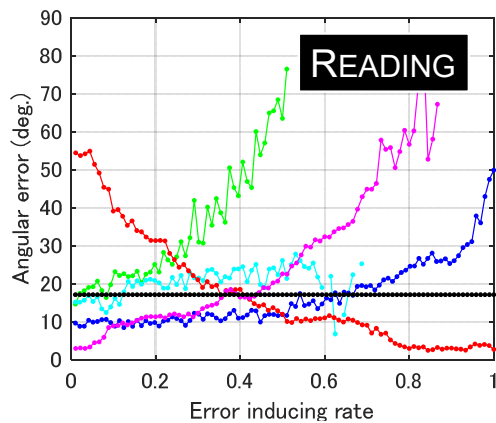
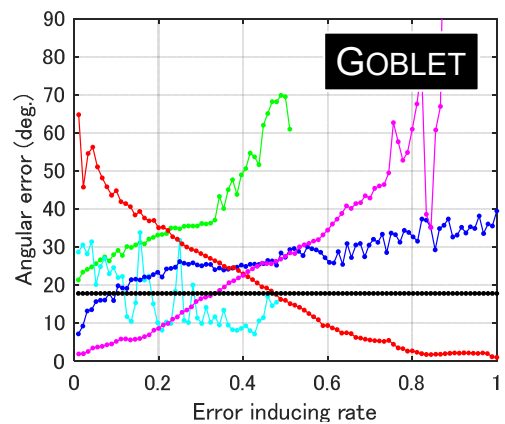
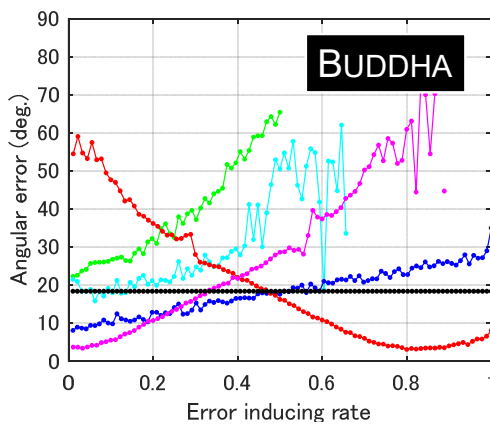
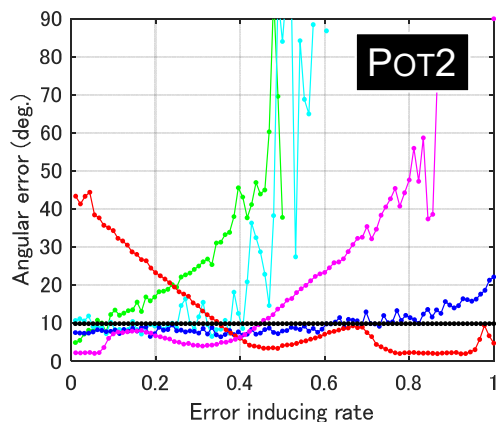
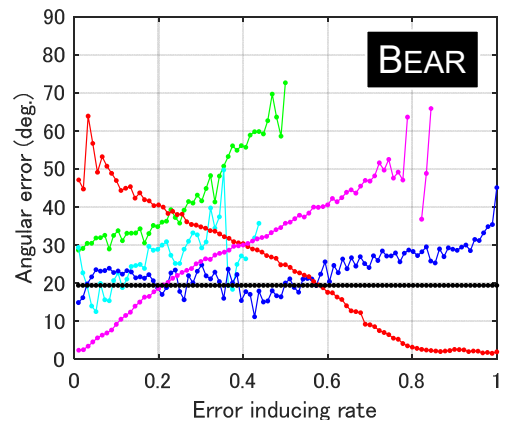
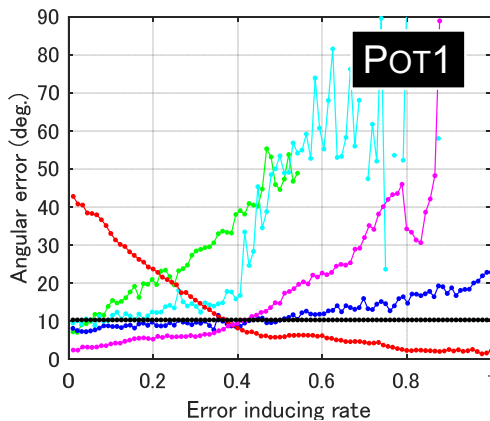
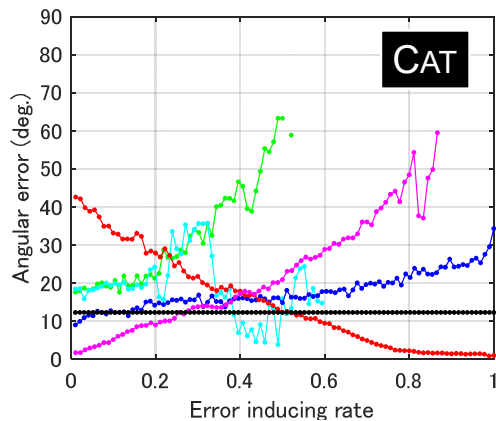
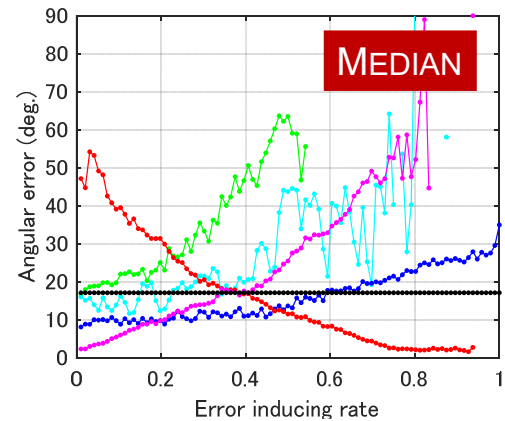
Attached shadow Cast shadow Interreflection Elevation angle Minimum half angle Average

# Part III Footnote 17: Complete Figure 5

## Non-Lambertian methods

### ST12

B. Shi, P. Tan, Y. Matsushita, and K. Ikeuchi. Elevation angle from reflectance monotonicity: Photometric stereo for general isotropic reflectances. In Proc. ECCV, 2012



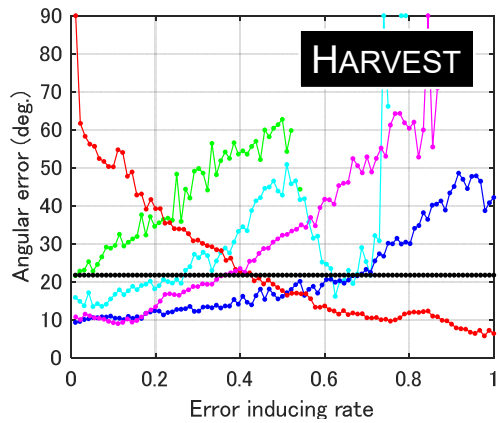
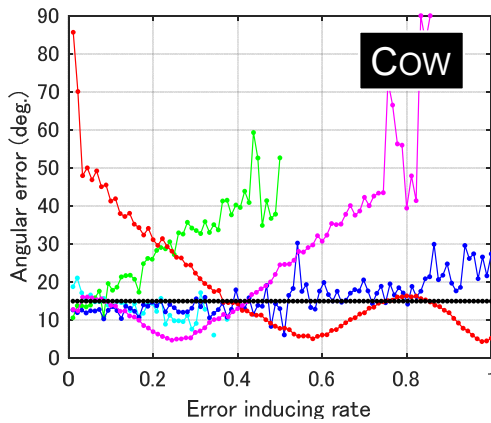
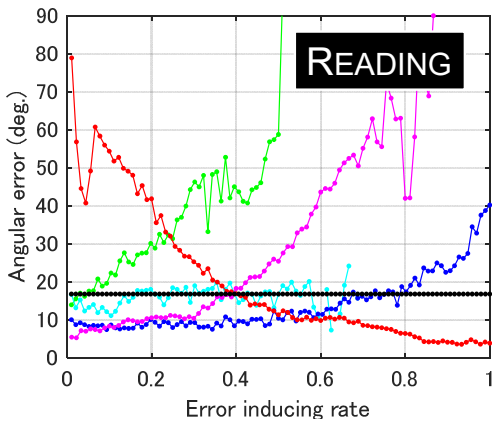
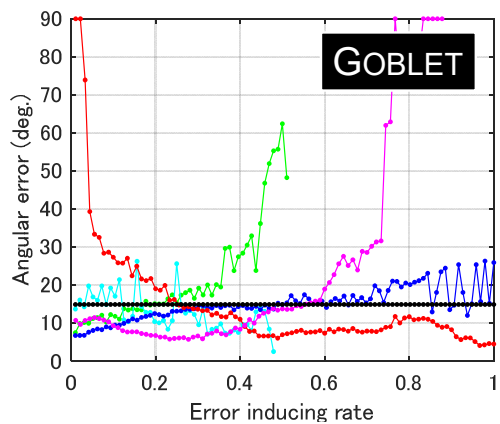
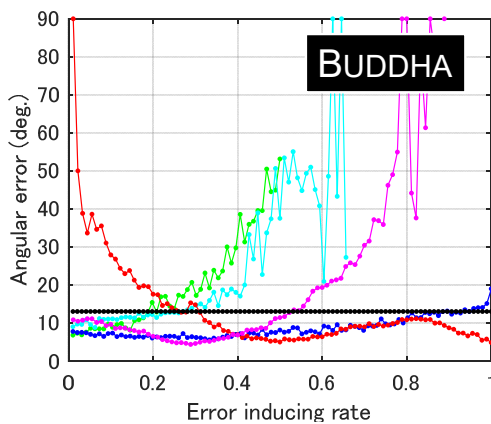
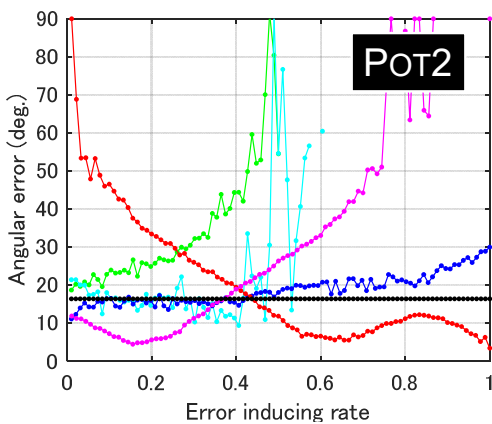
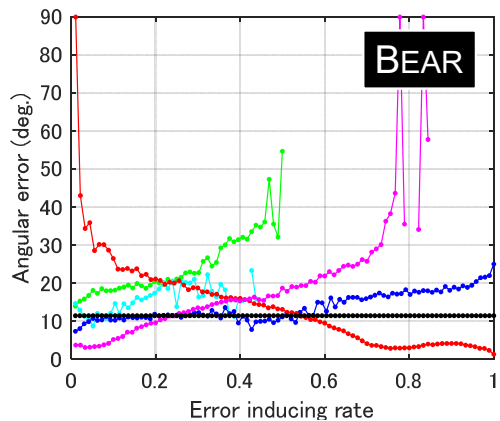
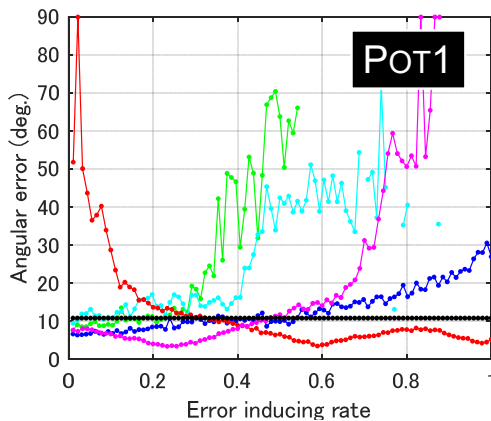
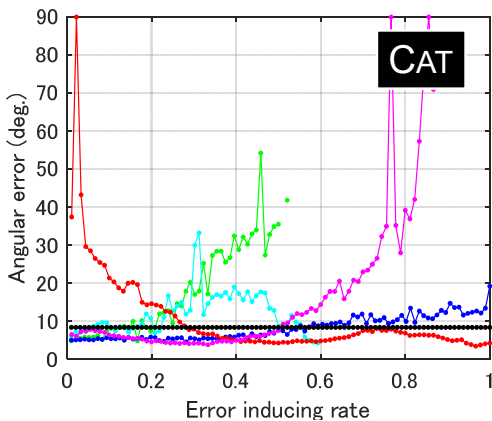
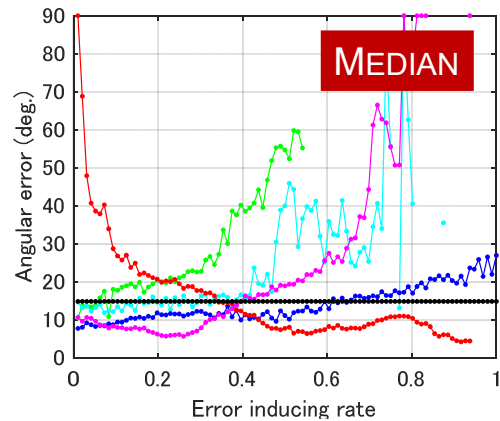
— Attached shadow — Cast shadow — Interreflection — Elevation angle — Minimum half angle — Average

# Part III Footnote 17: Complete Figure 5

## Non-Lambertian methods

### HM10

T. Higo, Y. Matsushita, and K. Ikeuchi. Consensus photometric stereo. In Proc. CVPR, 2010

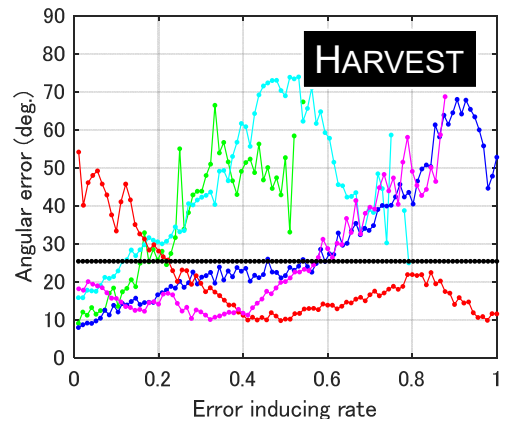
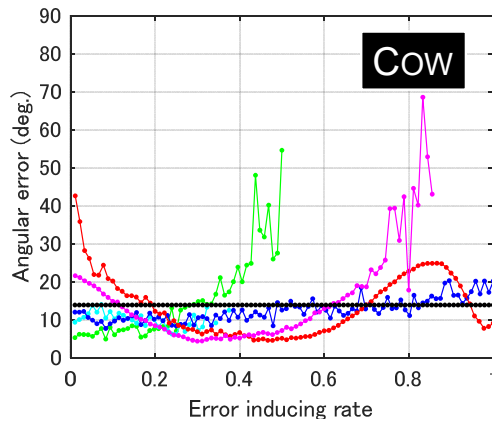
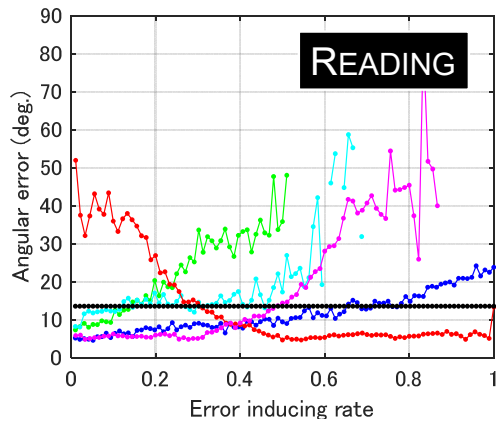
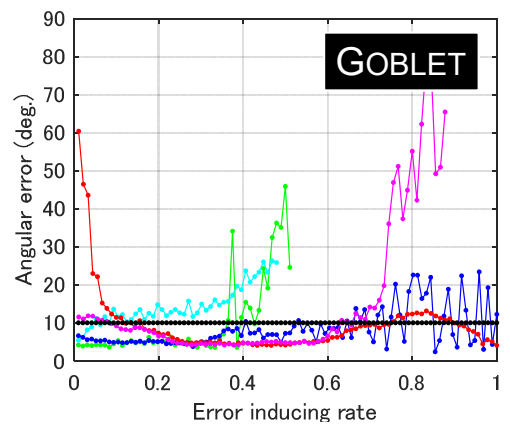
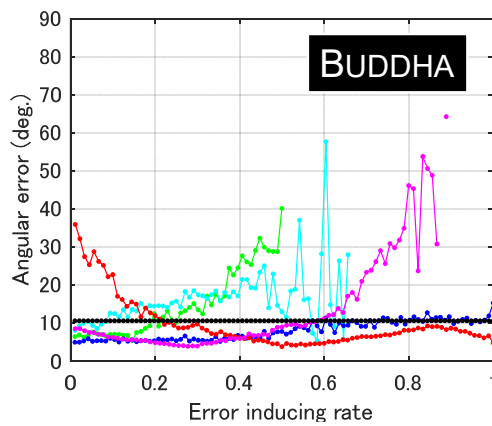
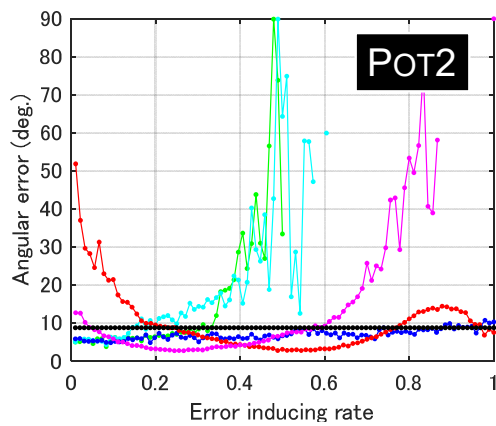
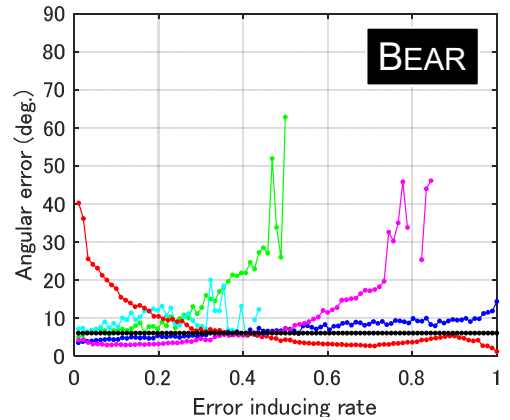
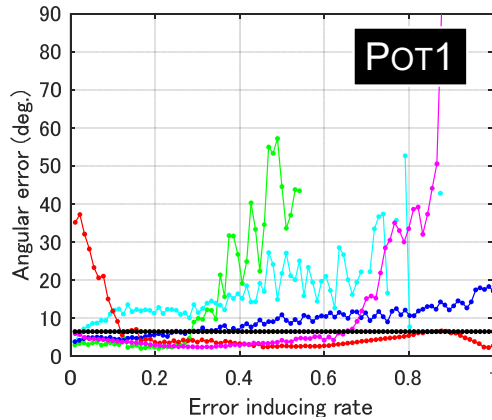
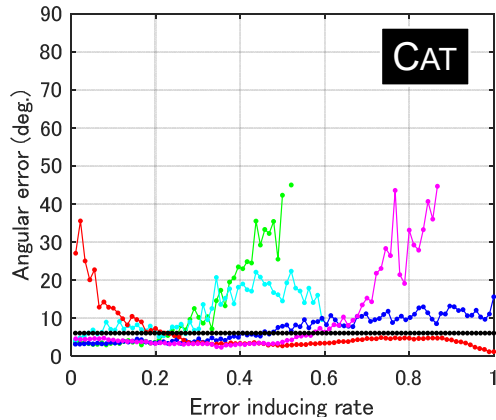
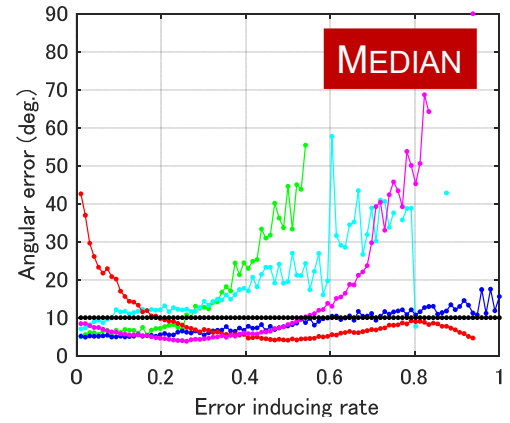


# Part III Footnote 17: Complete Figure 5

## Non-Lambertian methods

### ST14

B. Shi, P. Tan, Y. Matsushita, and K. Ikeuchi. Bipolynomial modeling of low-frequency reflectances. IEEE TPAMI 36(6):1078–1091, 2014



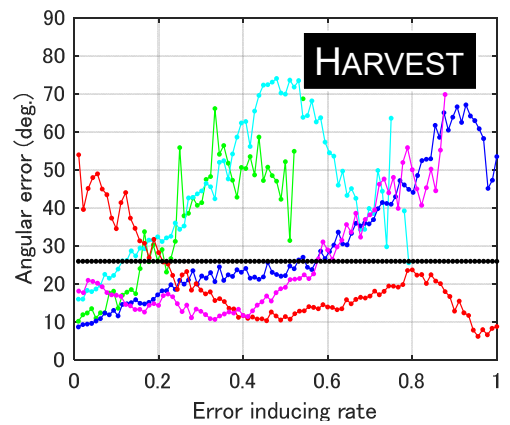
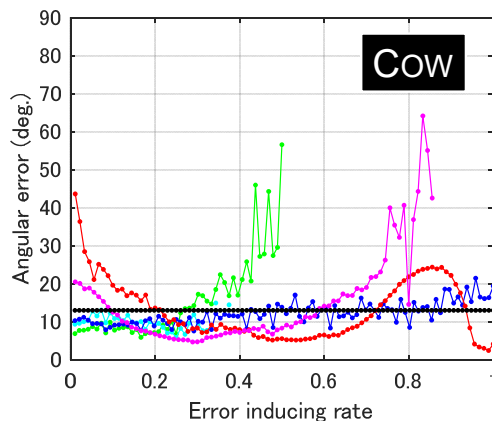
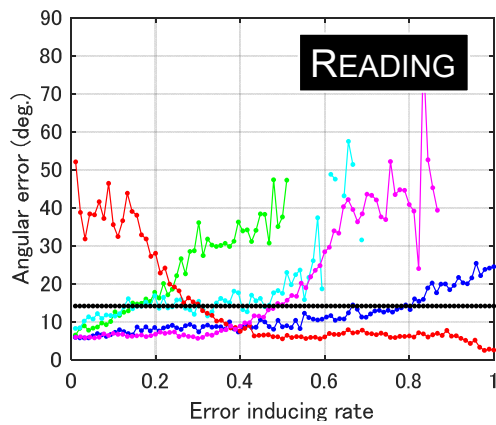
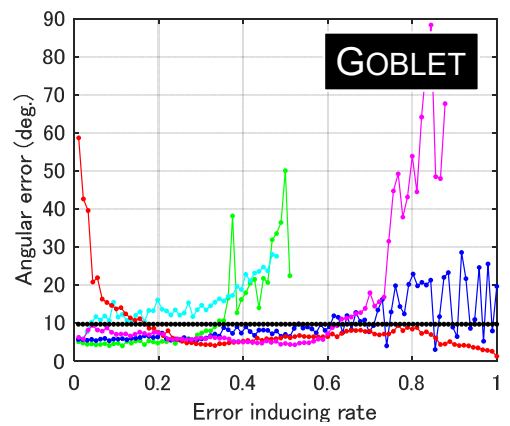
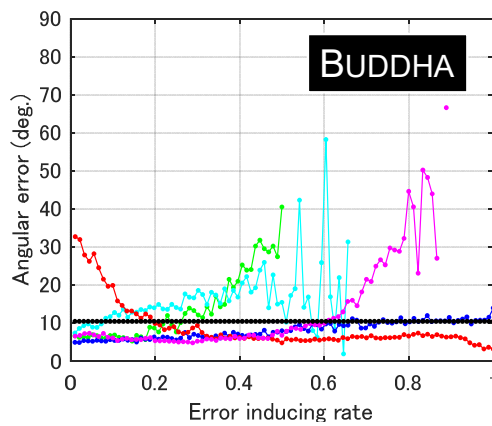
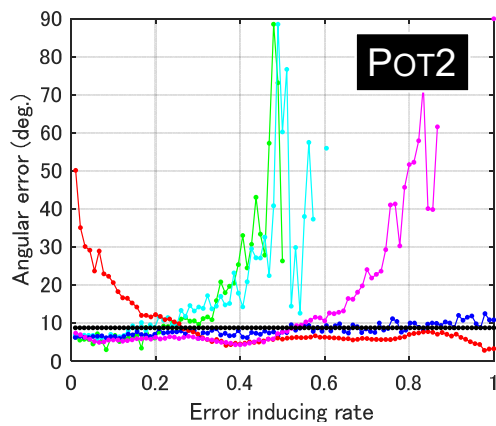
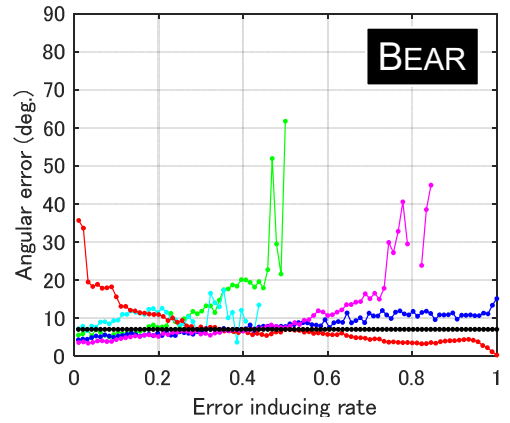
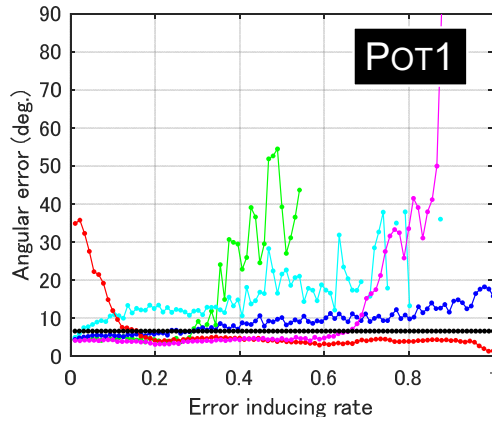
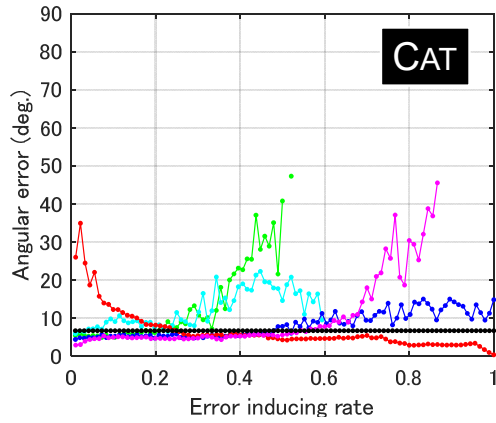
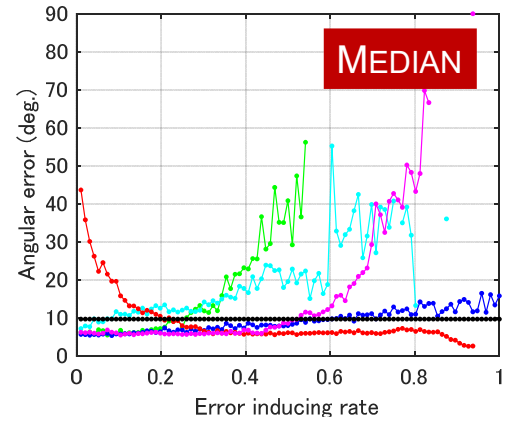
Attached shadow Cast shadow Interreflection Elevation angle Minimum half angle Average

# Part III Footnote 17: Complete Figure 5

## Non-Lambertian methods

### IA14

S. Ikehata and K. Aizawa, Photometric stereo using constrained bivariate regression for general isotropic surfaces. In Proc. CVPR, 2014

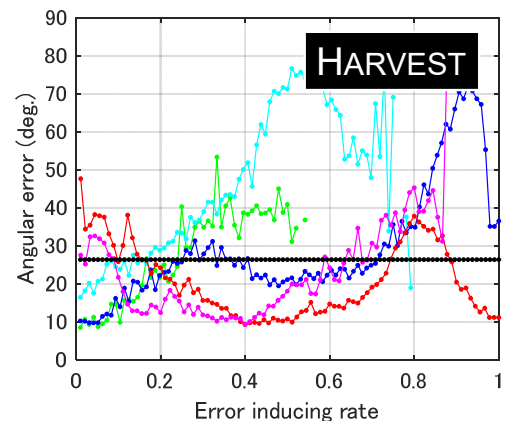
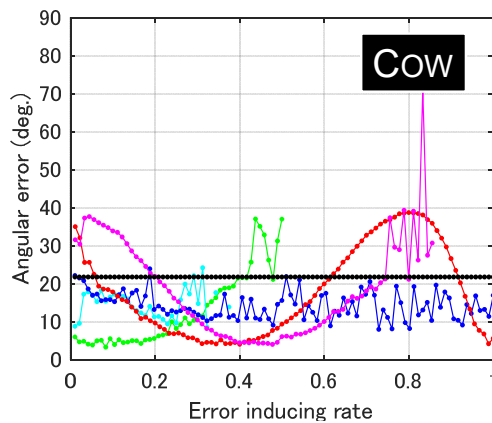
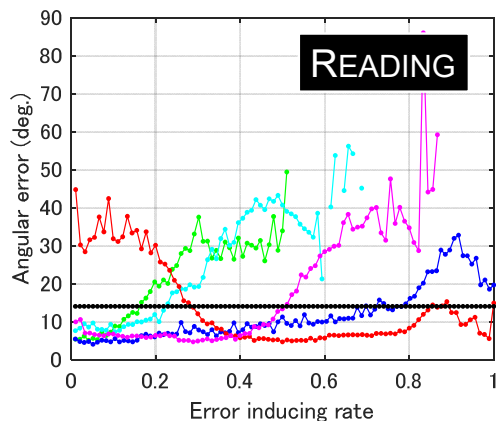
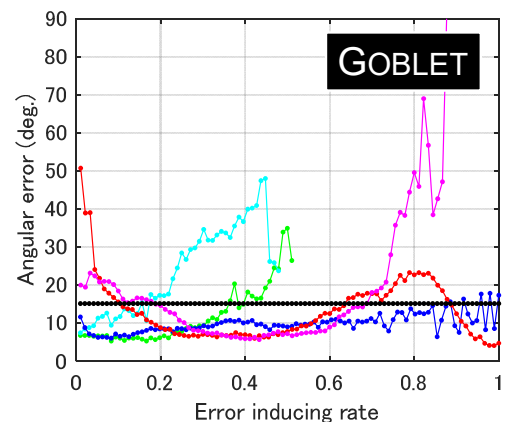
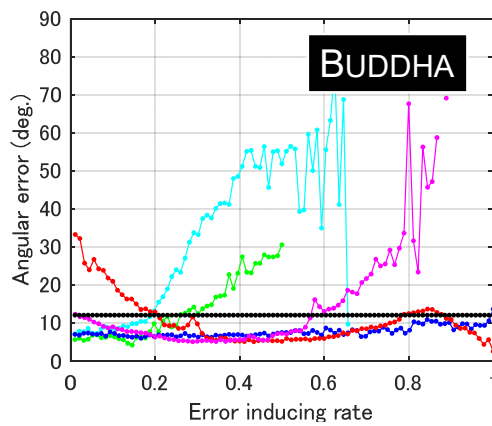
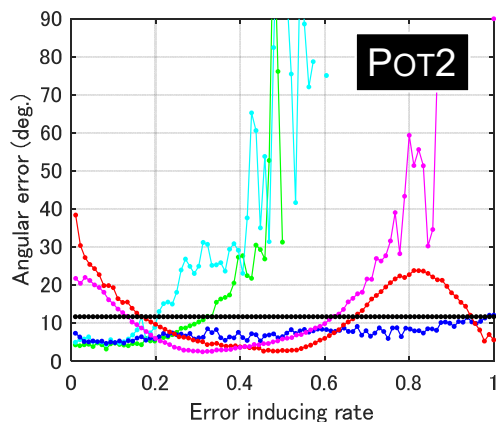
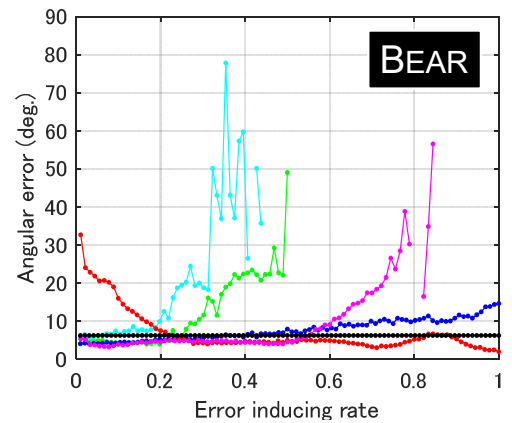
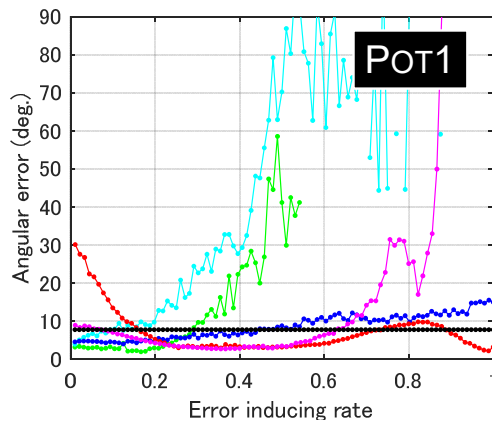
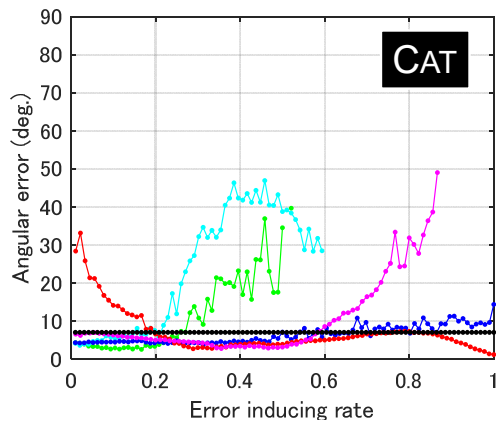
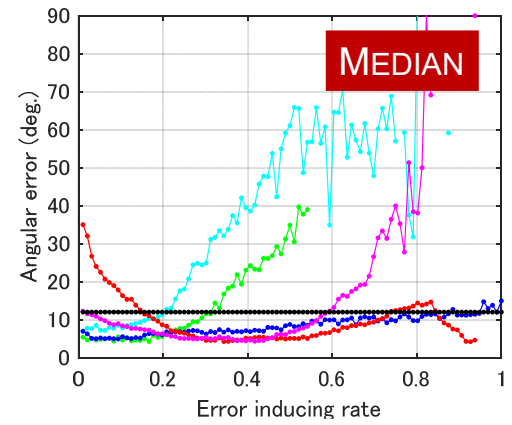


# Part III Footnote 17: Complete Figure 5

## Non-Lambertian methods

(20%, 80%)

Position threshold with the above setting

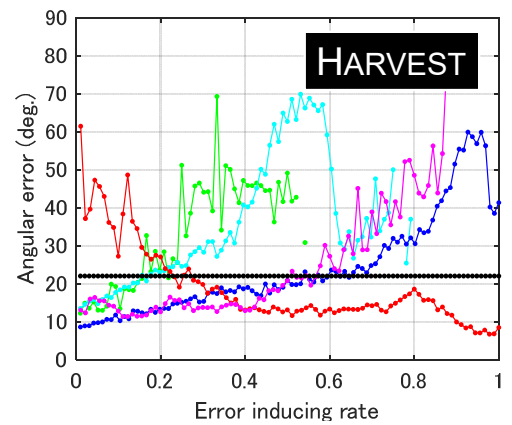
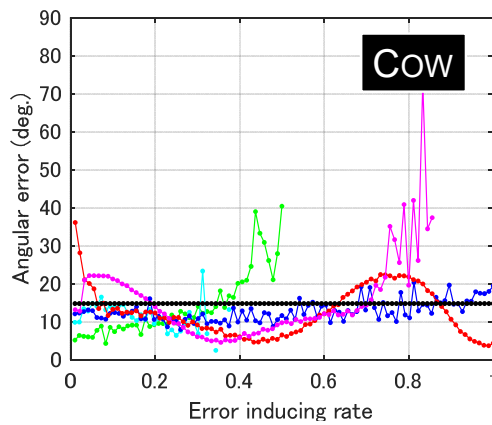
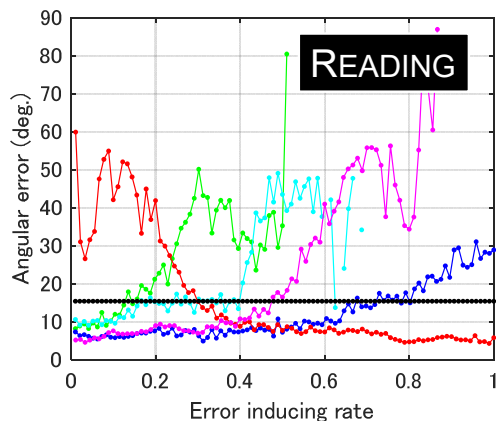
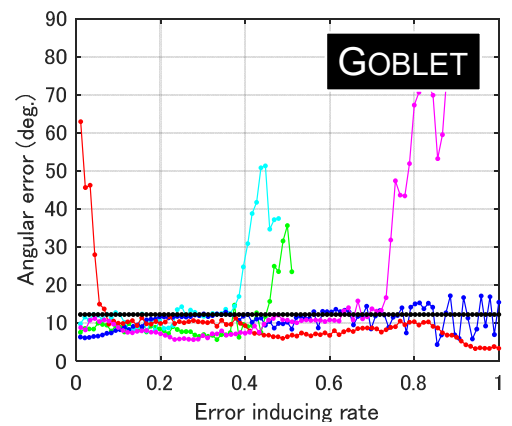
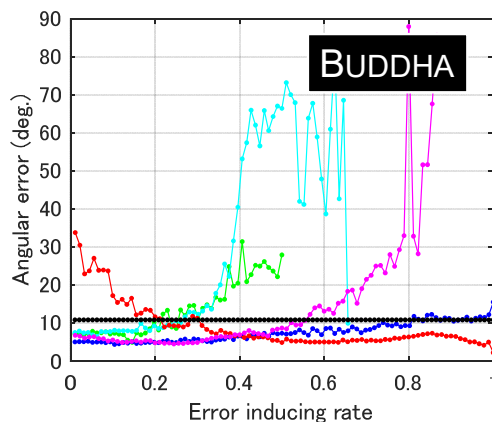
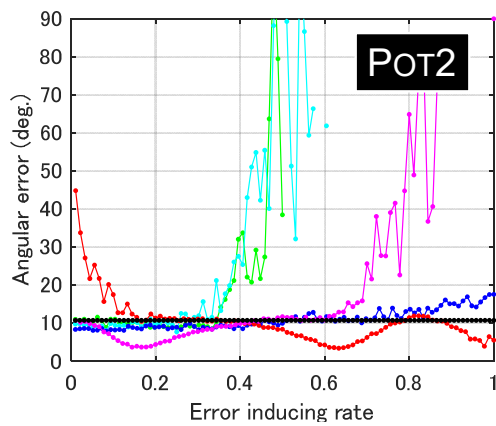
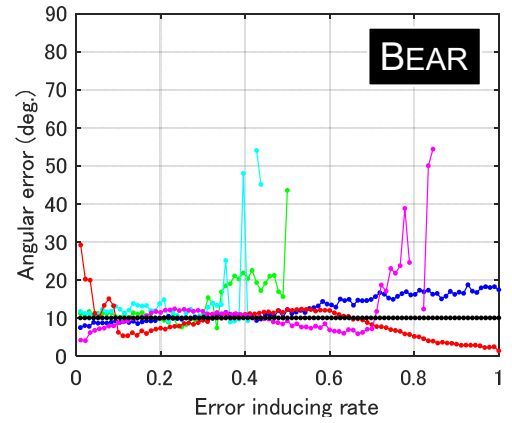
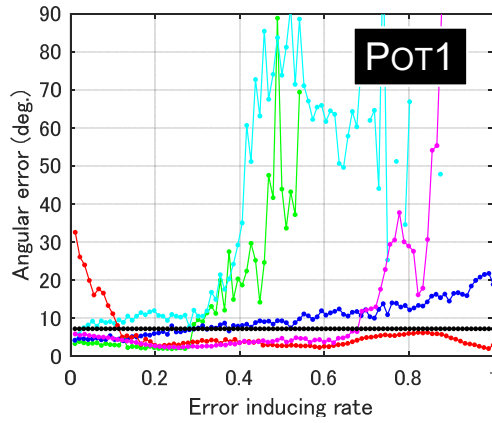
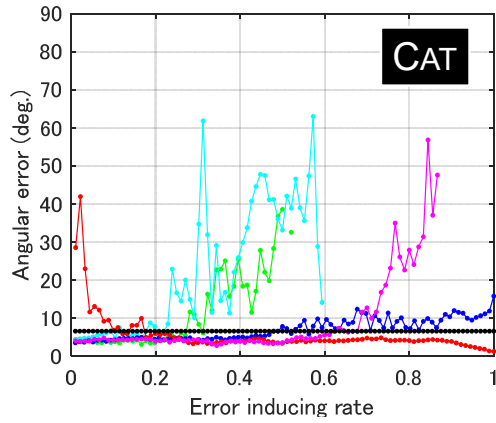
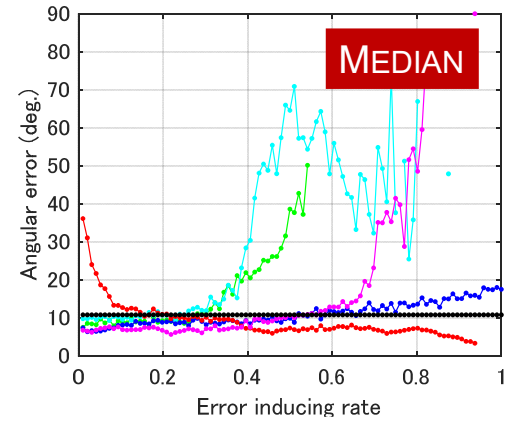


# Part III Footnote 17: Complete Figure 5

## Non-Lambertian methods

(40%, 60%)

Position threshold with the above setting

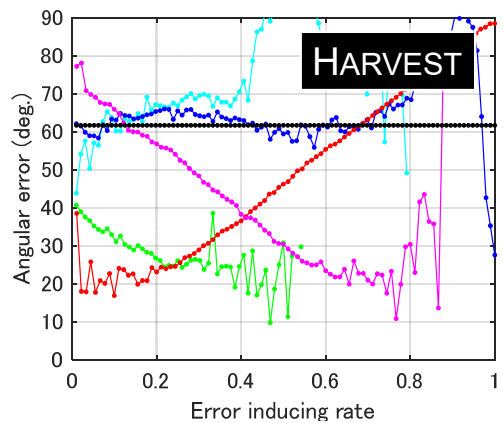
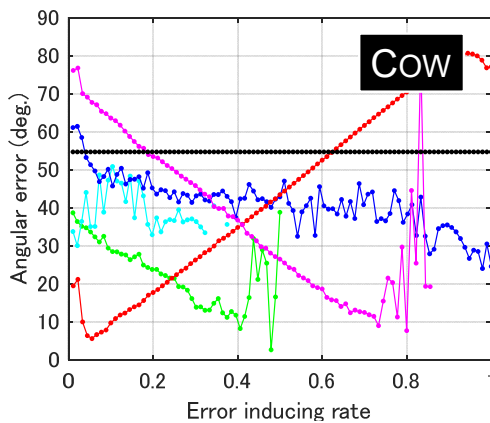
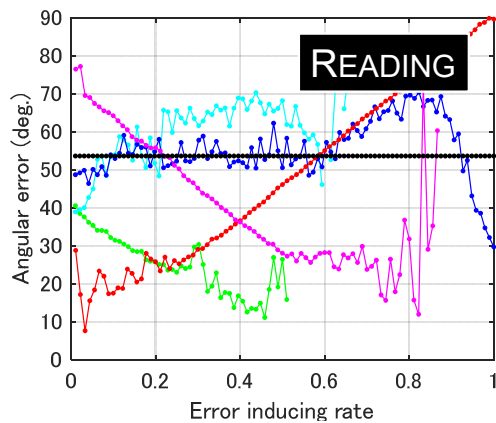
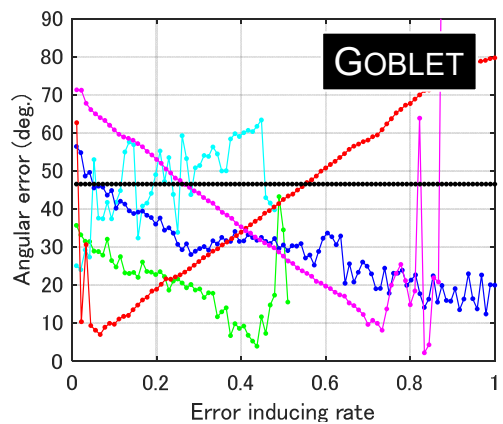
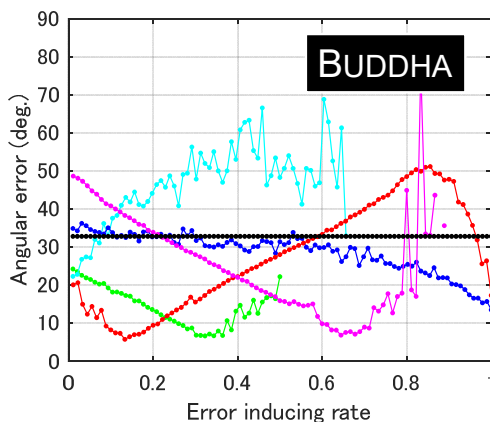
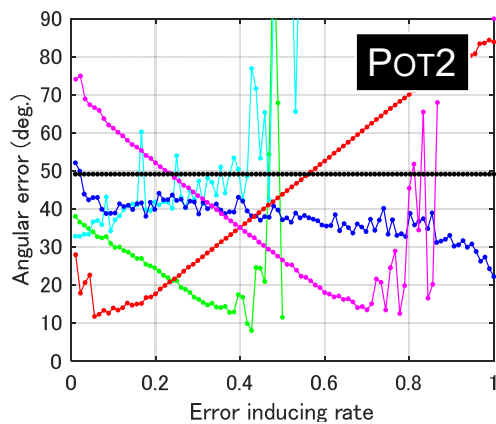
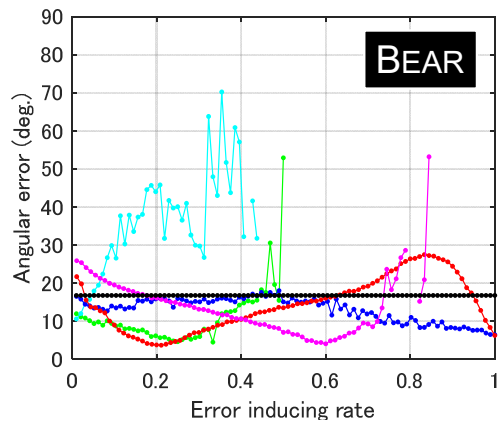
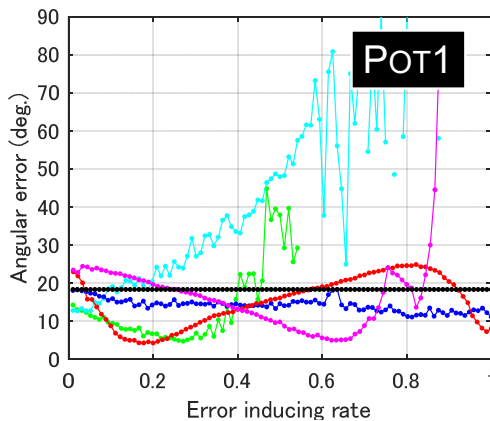
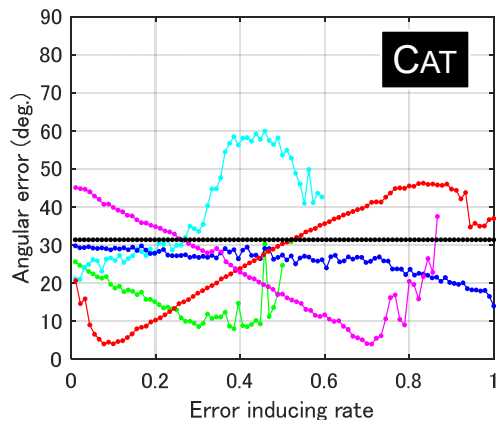
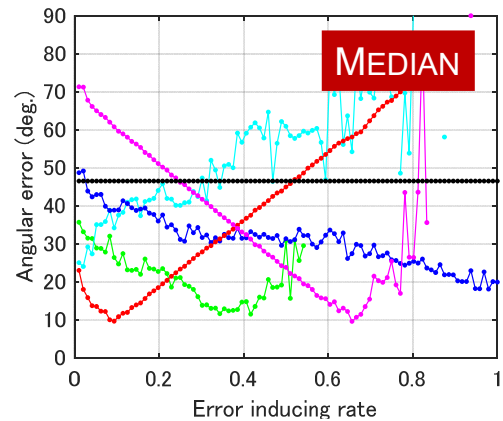


# Part III Footnote 17: Complete Figure 5

## Uncalibrated methods

### AM07

N. G. Aldrin, S. P. Mallick, and D. J. Kriegman. Resolving the generalized bas-relief ambiguity by entropy minimization. In Proc. CVPR, 2007



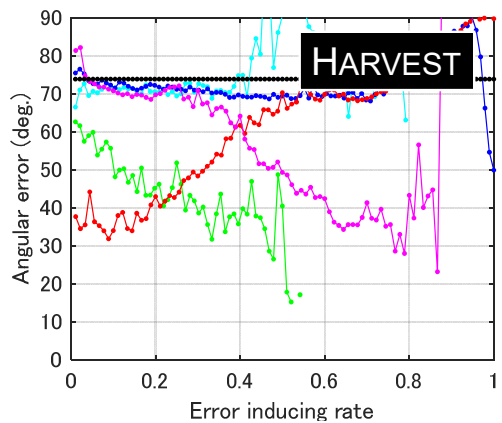
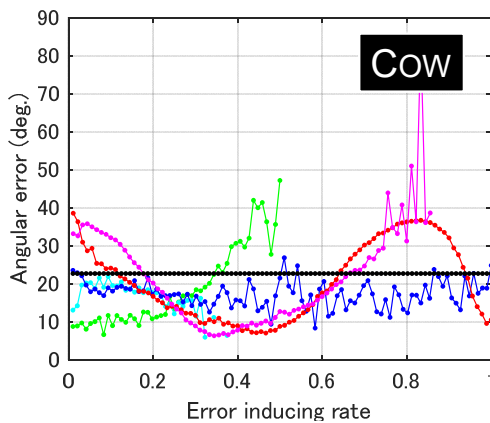
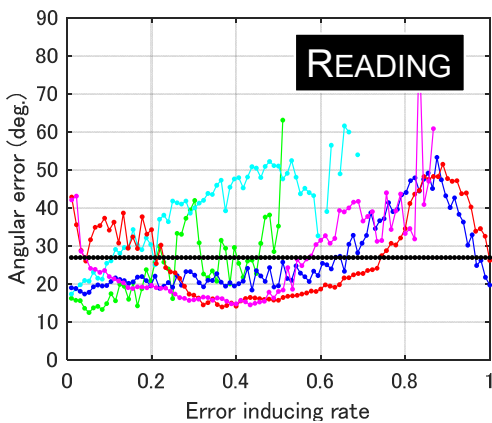
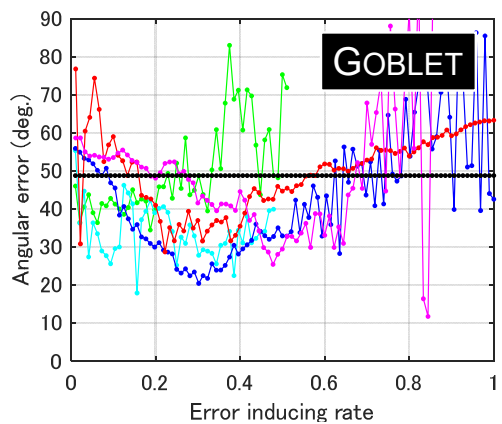
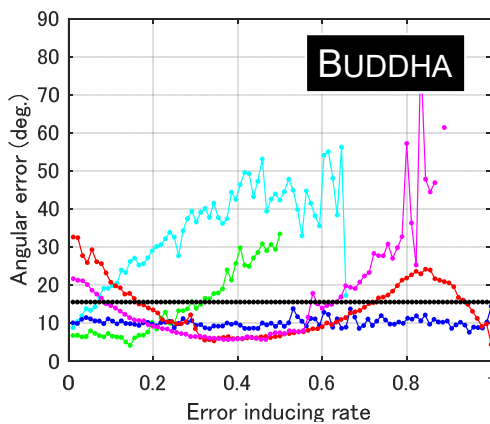
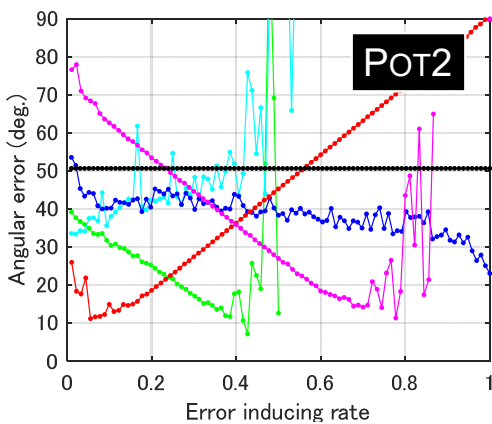
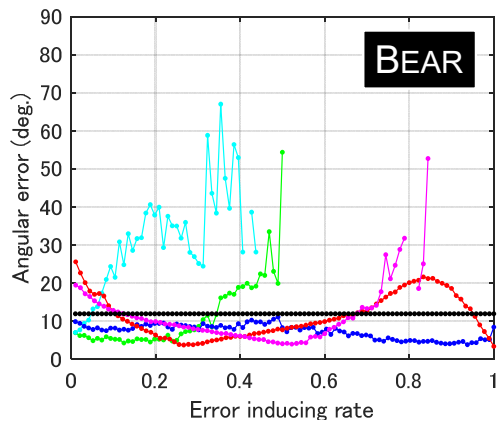
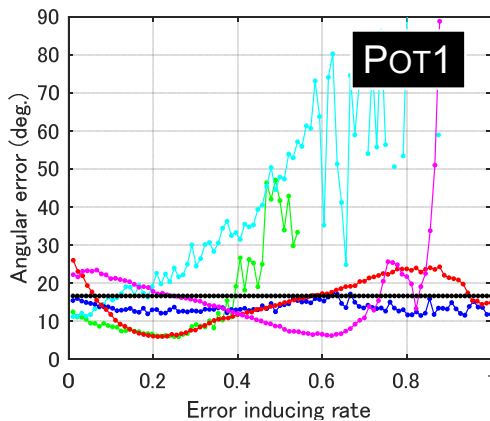
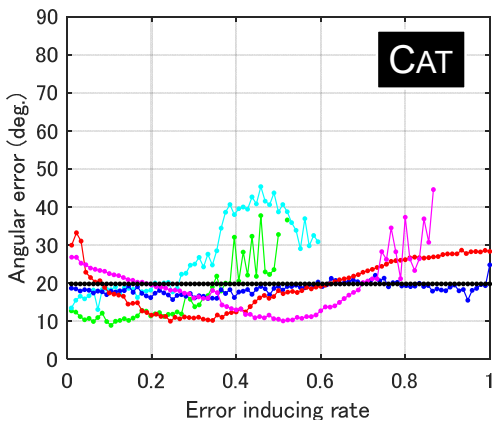
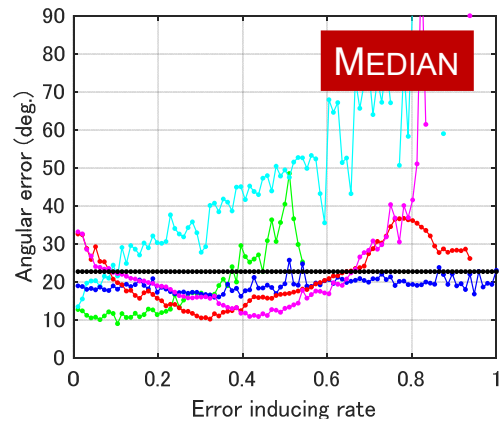
Attached shadow   Cast shadow   Interreflection   Elevation angle   Minimum half angle   Average

# Part III Footnote 17: Complete Figure 5

## Uncalibrated methods

### SM10

B. Shi, Y. Matsushita, Y. Wei, C. Xu, and P. Tan. Self-calibrating photometric stereo. In Proc. CVPR, 2010

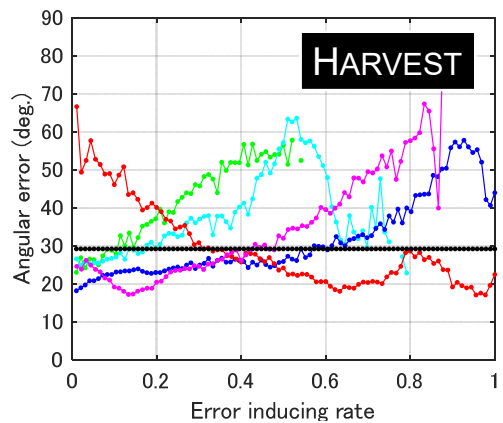
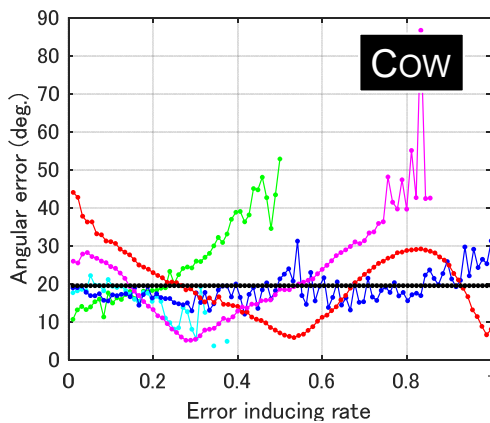
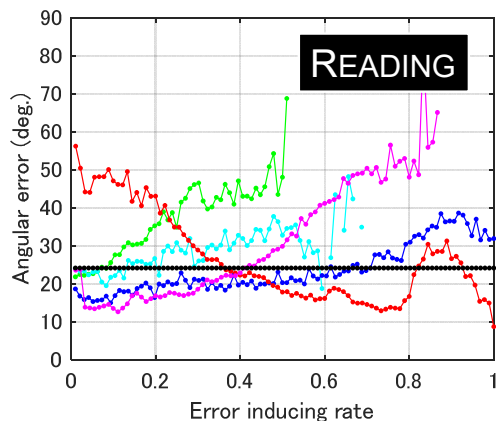
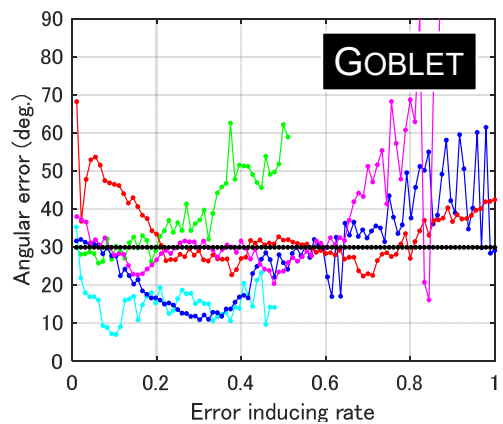
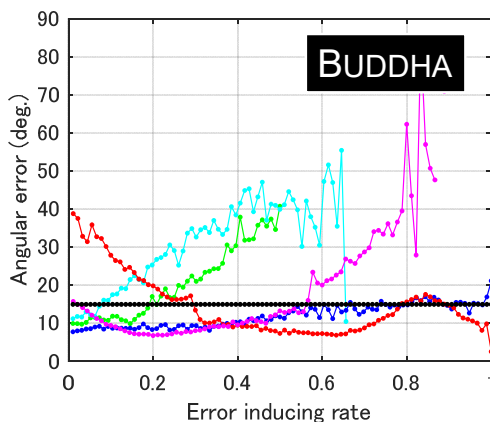
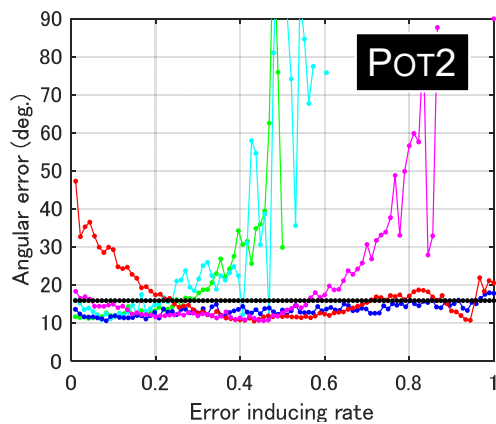
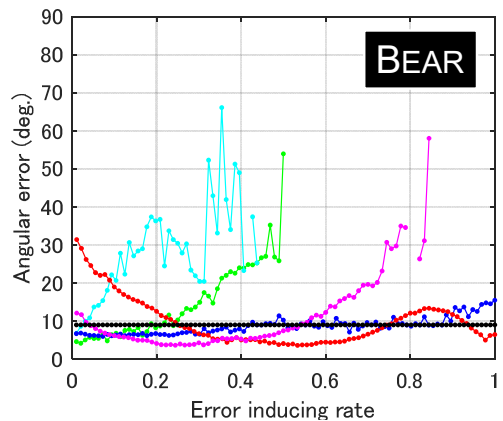
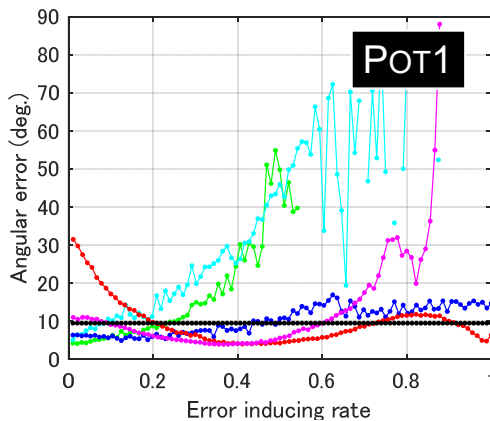
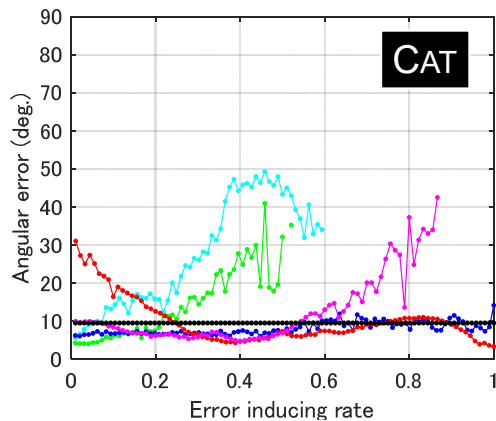
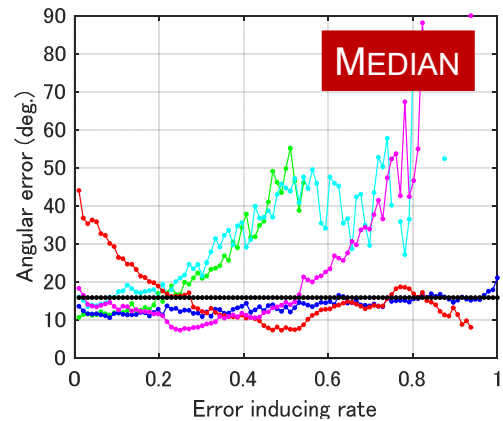


# Part III Footnote 17: Complete Figure 5

## Uncalibrated methods

### PF14

T. Papadhimetri and P. Favaro. A closed-form, consistent and robust solution to uncalibrated photometric stereo via local diffuse reflectance maxima. IJCV 107(2):139–154, 2014



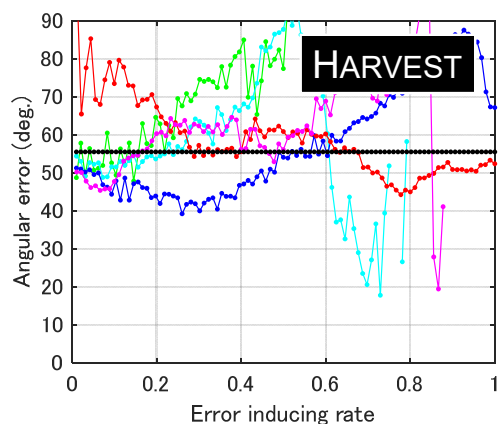
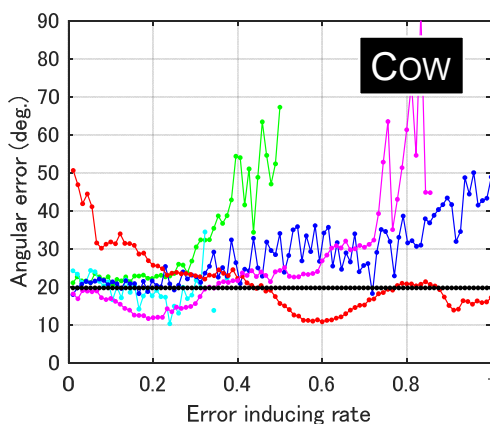
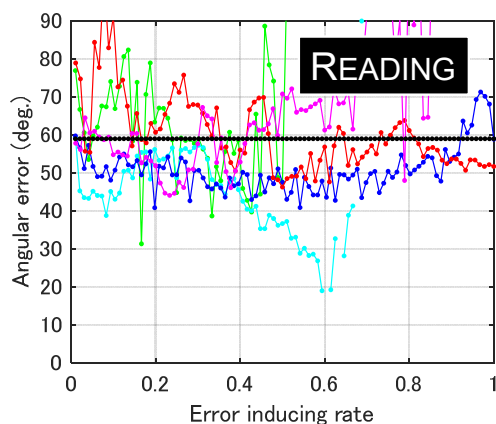
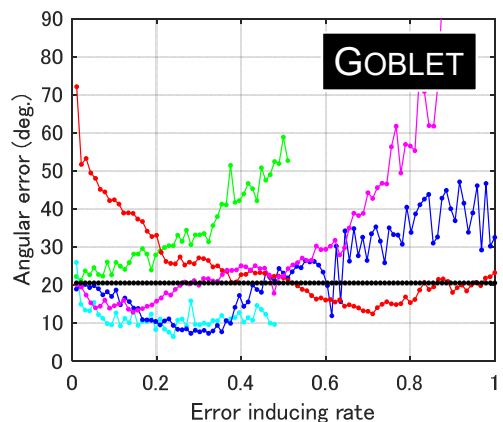
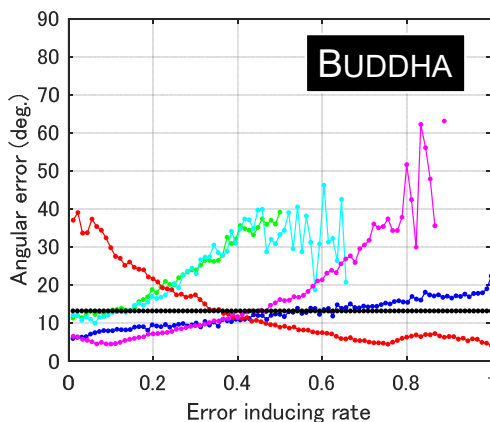
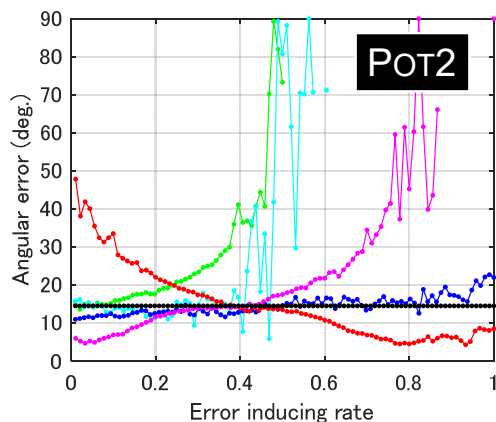
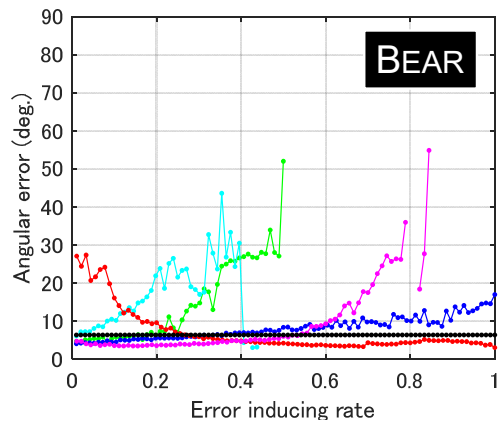
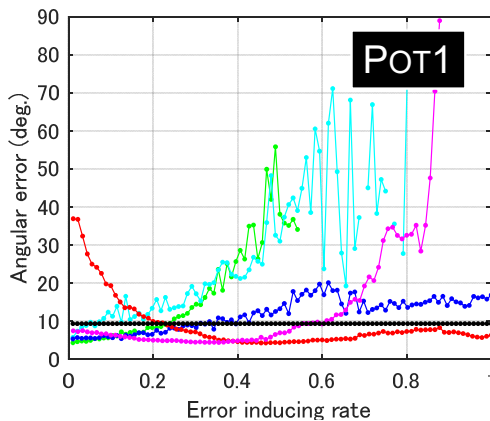
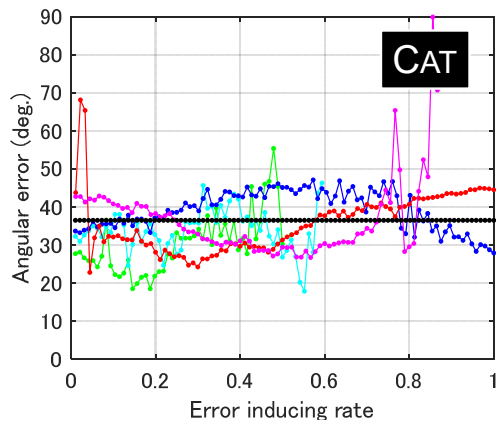
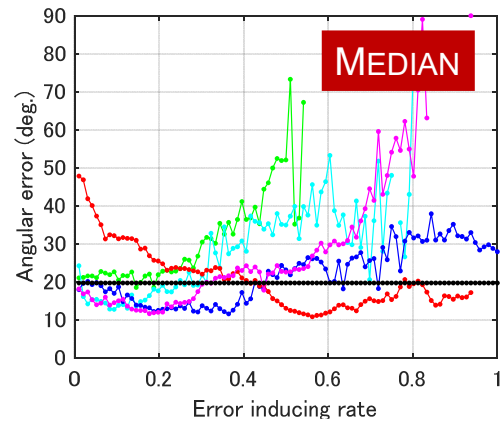
Attached shadow Cast shadow Interreflection Elevation angle Minimum half angle Average

# Part III Footnote 17: Complete Figure 5

## Uncalibrated methods

### WT13

Z. Wu and P. Tan. Calibrating photometric stereo by holistic reflectance symmetry analysis. In Proc. CVPR, 2013



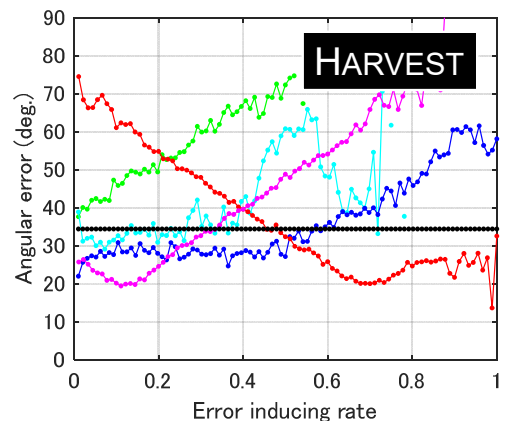
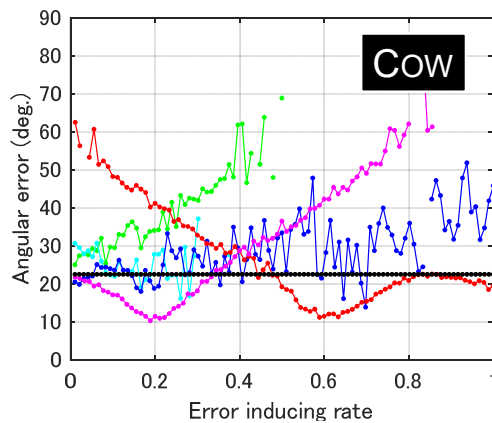
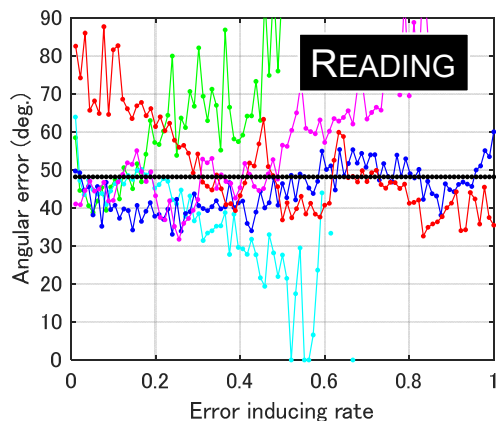
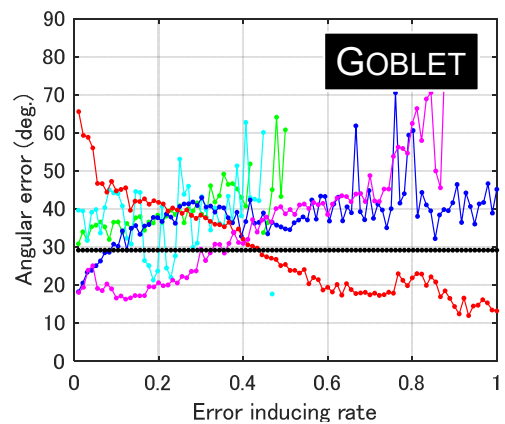
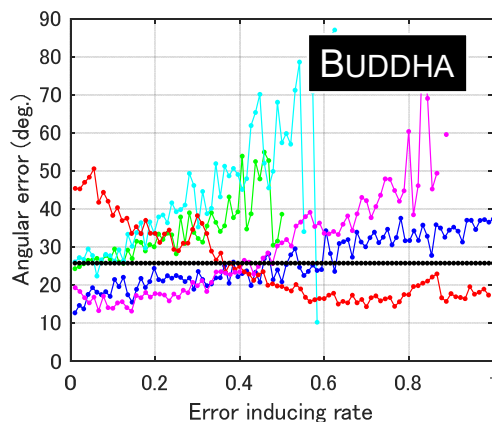
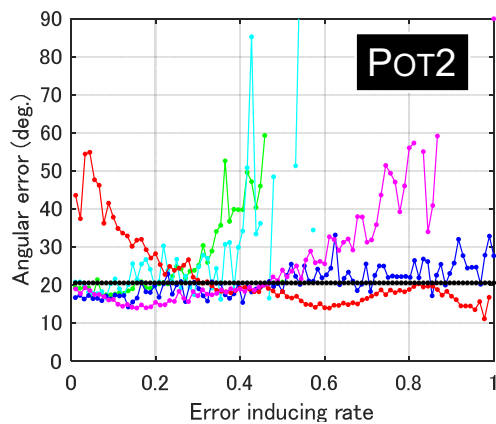
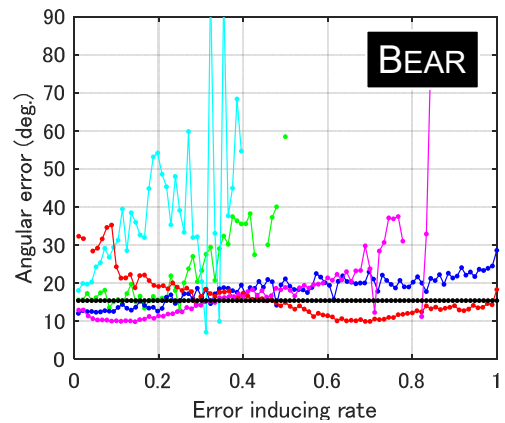
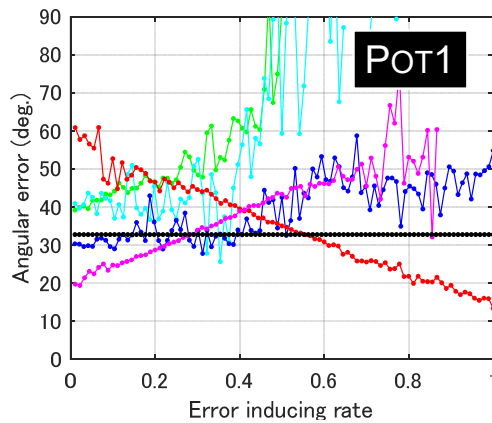
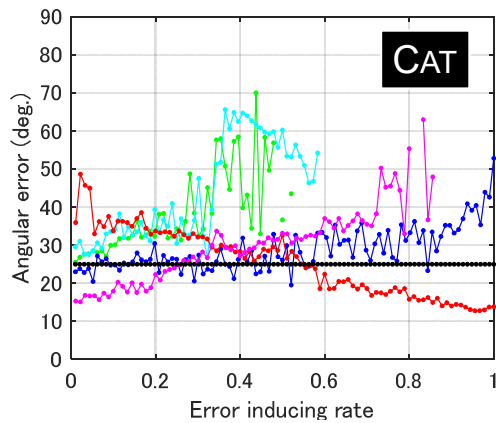
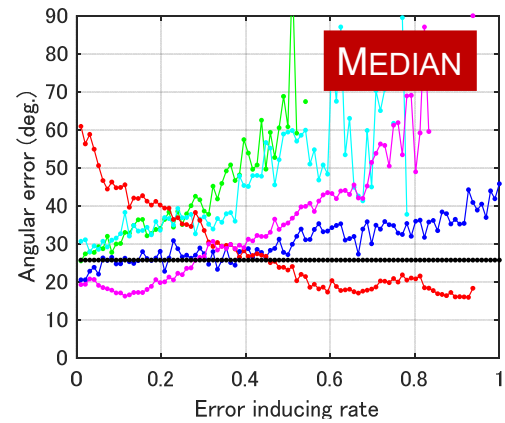
Attached shadow Cast shadow Interreflection Elevation angle Minimum half angle Average

# Part III Footnote 17: Complete Figure 5

## Uncalibrated methods

### LM13

F. Lu, Y. Matsushita, I. Sato, T. Okabe, and Y. Sato. Uncalibrated photometric stereo for unknown isotropic reflectances. In Proc. CVPR, 2013



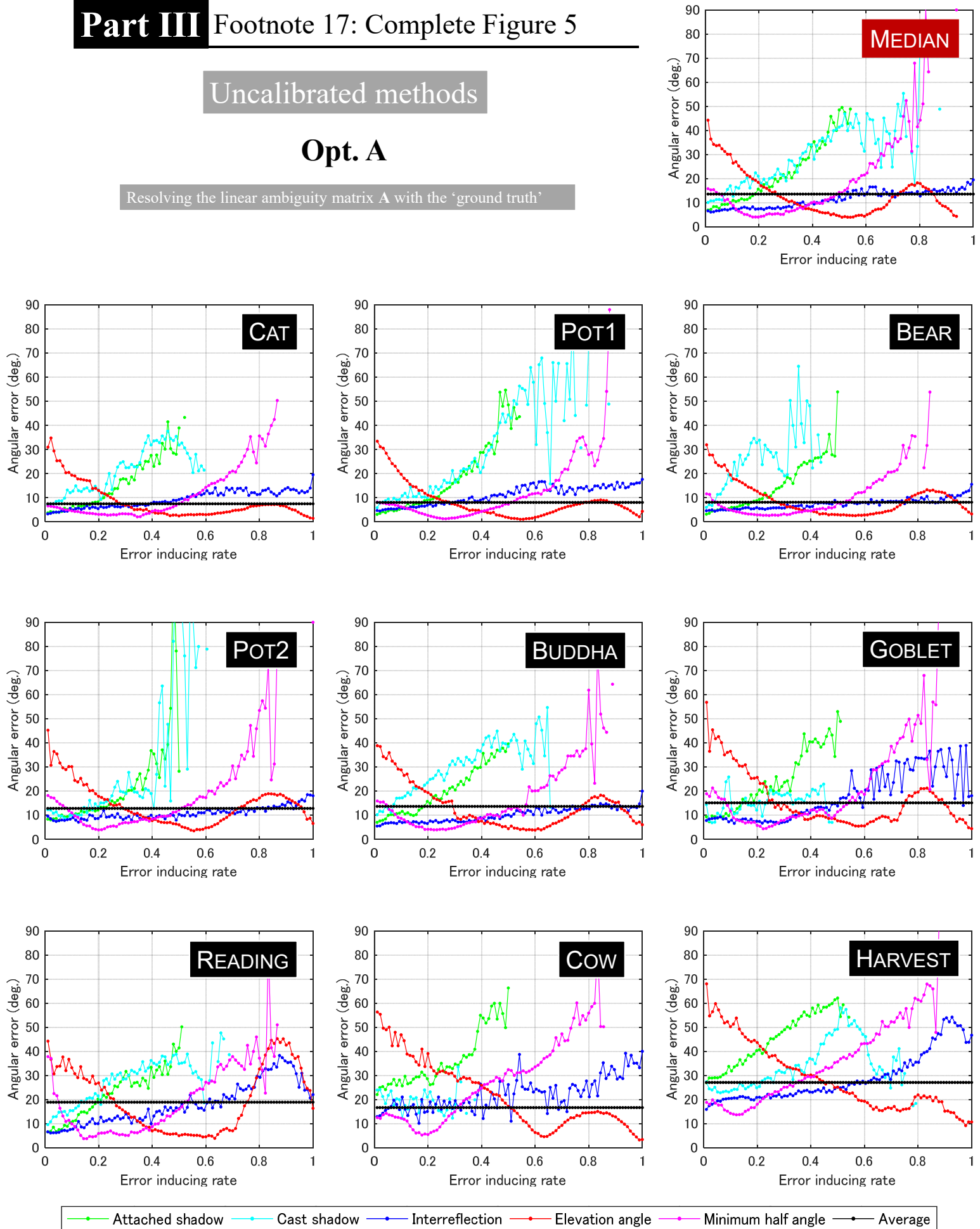
Attached shadow Cast shadow Interreflection Elevation angle Minimum half angle Average

# Part III Footnote 17: Complete Figure 5

## Uncalibrated methods

### Opt. A

Resolving the linear ambiguity matrix A with the 'ground truth'



# Part III Footnote 17: Complete Figure 5

## Uncalibrated methods

### Opt. G

Resolving the linear ambiguity matrix  $G$  with the 'ground truth'

